Supplementary Materials for

- **Constraints on the origin of the Martian dichotomy from the Southern Highlands marsquakes**

Weijia Sun, Hrvoje Tkalčić

*Corresponding author. Email: swj@mail.iggcas.ac.cn, hrvoje.tkalcic@anu.edu.au

This PDF file includes:

Supplementary Text
Figs. S1 to S58
Tables S1 to S4

Supplementary Text

S1. Picking of P-wave and S-wave arrivals

Figures S1-S24 illustrate the picked P-wave and S-wave arrivals with a scalogram and four techniques to improve the clarity of the P- and S-wave onsets. The scalogram is calculated by the continuous wavelet transform (CWT) with the wavelet parameter of 10 to balance the time and frequency resolution. The minimum and maximum frequencies are 0.1 and 1 Hz. The sampling rate of the time series is 20 Hz. In contrast to the conventional spectrogram as a function of time and frequency, the scalogram is a function of time, frequency, and scale, which exhibits better time and frequency localization or resolution. This makes the scalogram more suitable for analyzing marsquake signals containing many abrupt transients, such as glitches and wind noise.

We further test the influences of noise on the time-picking schemes utilized in the paper. We add varied strength noise (0%-200% amplitude stronger than the maximum amplitude of S arrival) on the raw 02.BHV component for the event S0173a in Fig. S25. As the noise becomes more substantial, the onsets of the bandpass-filtered S arrival become ambiguous, but the DAPF and CCH-filtered waveforms show distinct S arrival onsets. The CCF-filtered results do not provide clear onsets since the CCF approach employs the Fourier transform, which accounts for both amplitudes and phases.

S2. Optimal frequency band for back azimuth selection

The hodogram or particle motion of the P-wave is ideally rectilinear or elliptic (18). However, the hodogram analysis is sensitive to the time window and frequency band choice for the low signal-to-noise ratio marsquakes (18). With the aid of multiple time-picking techniques we utilize, the accuracy of phase picking is significantly improved. The negative influence of the time window can thus be neglected. The time window for the hodogram analysis is 0-10 s relative to the picked P arrival.

Filter banks are helpful tools for selecting the optimal frequency band, leading to well-polarized P-wave arrivals. We design a set of filter banks with frequencies ranging between 0.1 Hz and 1 Hz with various bandwidths of 0.3 Hz, 0.4 Hz, 0.5 Hz, 0.6 Hz, 0.7 Hz, 0.8 Hz, and 0.9 Hz. For example, the frequency bands are 0.1-0.6 Hz, 0.2-0.7 Hz, 0.3-0.8 Hz, 0.4-0.9 Hz, and 0.5-1 Hz for the bandwidth of 0.5 Hz. All combinations result in 28 frequency bands in total.

The 3-D principal component analysis is performed on all bandpass-filtered marsquakes. The signal-to-noise ratio (SNR) is calculated from the eigenvalues of 3-component seismograms (19). We describe in the Methods how we select the optimal back-azimuth using both SNR and the polarization shape. The hodogram maps in the 28 frequency band for each marsquake are displayed in Figs S26-S53.

We also compare the back-azimuth and SNR determined by the 2-D and 3-D principal component analysis in Fig. S54. As can be seen, the back azimuths measured by the 2-D and 3-D methods are similar, but the 3-D back azimuth provides smaller uncertainties (Fig. S54A). In Fig. S54B, the SNR of the 2-D analysis is generally higher than the 3-D one. This is because the 2-D analysis uses the two horizontal components, and the 3-D analysis uses the three-component components to measure back-azimuth.

Here, we discuss several marsquakes, featured in Fig. 2. The S0173a marsquake, the most prominent of all recorded marsquakes, presents a rectilinear particle motion, giving a back azimuth of $88.8 \pm 2.8°$ in 0.2-0.5 Hz, which agrees well with the values of $91^{+11°}_{-12°}$ in MQS (42)and $88^{+15°}_{-10°}$ (18).

Another prominent marsquake, S0235b, demonstrates the elliptic shape of P-wave particle motions, giving a back azimuth of $67.6 \pm 8.8°$ in the frequency band 0.4-0.8 Hz. This is consistent with the ones of $74^{+14°}_{-8°}$ in MQS (42) and $77^{+23°}_{-13°}$ (18).

The marsquake S1048d is seriously contaminated by low-frequency (<0.2 Hz) noise overlapping with the frequency band of glitches. To include the strong P-wave energy in the frequency band of 0.3–0.5 Hz, we select a broader band of 0.3–1 Hz as the optimal band, which leads to a back azimuth of $191.7 \pm 28.2°$ (Fig. 2L).

S3. Seismic attenuation from spectral ratio approach

We employ the spectral ratio method (Equations 6 and 7) to estimate the quality factor Q_S from S arrivals in Terra Cimmeria, Southern Highland, where a group of marsquakes is located. These marsquakes in Cimmeria have similar epicentral distances ($\sim 30°$) with the two marsquakes S0173a and S0235b in Cerberus Fossae. The Q_S value calculated from the spectral ratio between the Cimmeria marsquakes and the two Cerberus Fossae marsquakes can therefore be regarded as the quality factor beneath the Cimmeria region. The S arrival waveform is taken in the time window of 0-20 s relative to the picked S phase. The Q_S from S arrivals is estimated to be 483.7.

The Q_S estimation from S arrival may be affected by the focal mechanism. To reduce these uncertainties, we further measure the quality factor from the coda wave of three selected marsquakes, i.e., S0173a, S0864a, and S1039b, since coda waves are thought to be generated by scattering of heterogeneities along the ray path. In addition, the three marsquakes have very similar epicentral distances of 1749.6 km, 1705.5 km, and 1741.2 km. The Q_c value from the coda wave is calculated on two horizontal components of 02.BHE and 02.BHN by the spectral ratio approach (Equations 8 and 9). The estimated Q_c for S0173a in Elysium Planitia is greater than 800 from measurements of coda waves.

The coda wave is taken from the time window of 100-200 s after the picked S phase. Their amplitude spectrums are illustrated in Fig. S57, which presents a similar feature with S arrival, i.e., the amplitude spectrum of S0173a in Elysium Planitia is stronger than S0864a and S1039b in Terra Cimmeria. The linear regressions are given in Fig. S58. We calculate the Q_c value in three different frequency bands: 0.1-0.5 Hz, 0.1-0.8 Hz, and 0.2-0.5 Hz, giving $Q_c = 512.9 \pm 66.3$, 481.0 ± 12.9 and 542.9 ± 87.6.

S4. Summaries of the newly located marsquakes

Table S1 summarizes the picked P and S arrivals and their uncertainties by the MQS and this study. The arrival time is defined in this study as the average time selected by multiple techniques. The arrival uncertainties are the standard deviation of the picked arrivals according to multiple techniques. Table S2 illustrates the back azimuth and their uncertainties by the MQS, previous studies, and this study. Tables S3-S4 provide verifications of our methods with ground-truth meteoroid impacts. The uncertainties of the estimated back-azimuths in this study are smaller than in previous studies, arguably due to the optimal selection of frequency band and more accurate phase-arrival time.

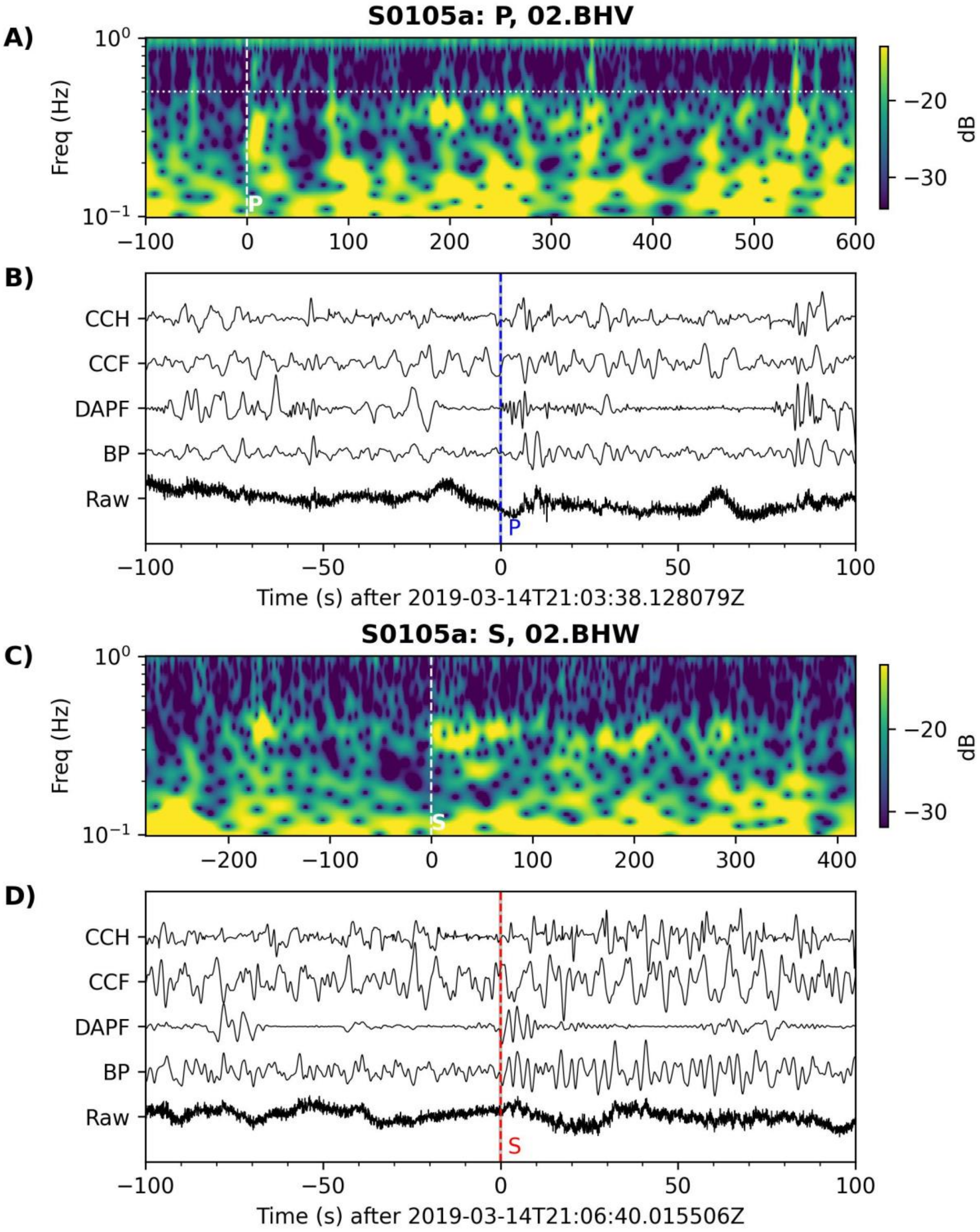

Fig. S1. P and S arrival picks for the event S0105a. The horizontal white dotted line is at 0.5 Hz. A) Scalogram of the component that the P arrival is picked on. B) Various filters applied on the P-wave waveforms relative to the picked P arrival. C) Scalogram of the component from which the S arrival is picked. D) Various filters applied on the S-wave waveforms relative to the picked S arrival. For the filter abbreviations, see the main text.

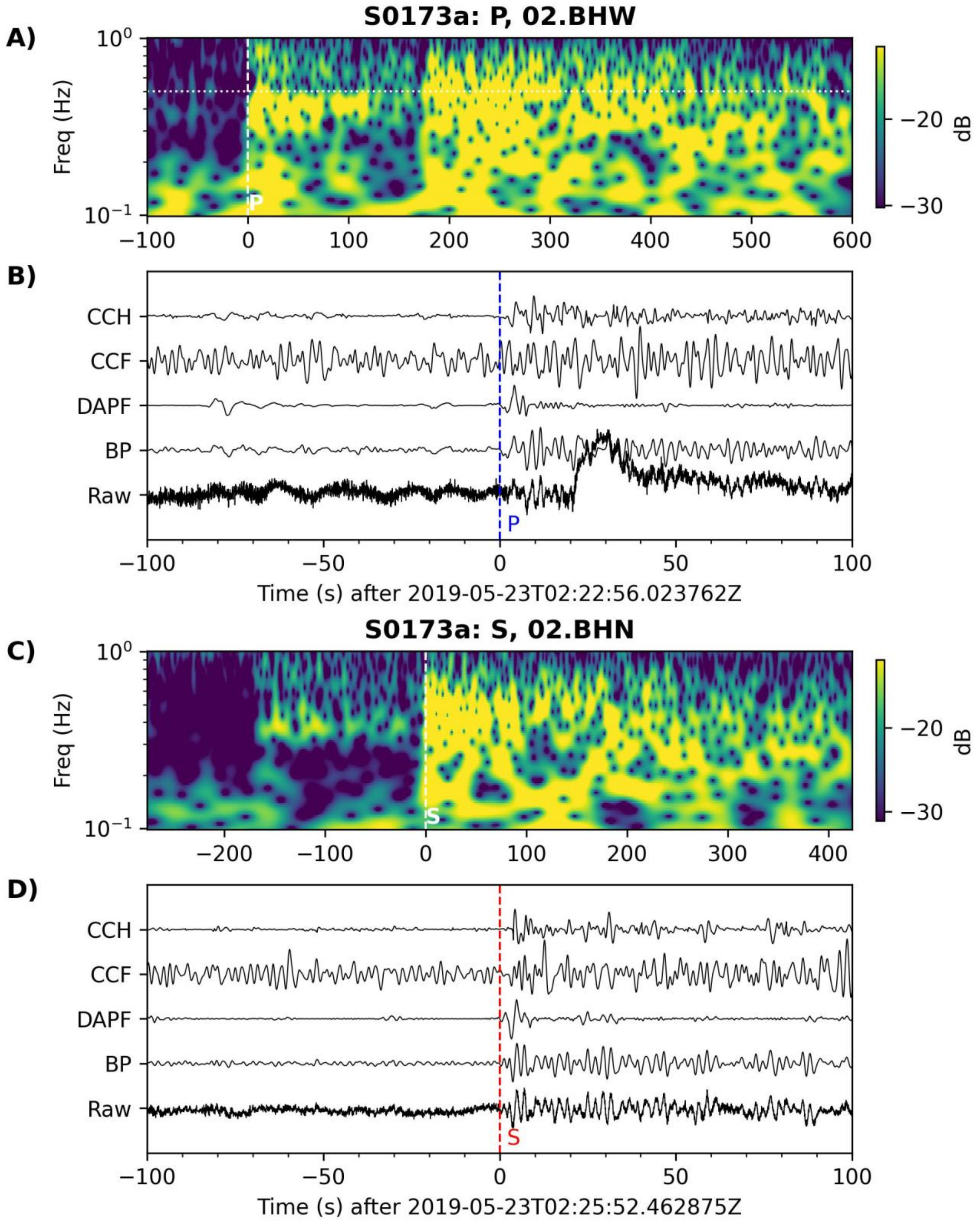

Fig. S2. Same as Fig. S1, but for S0173a.

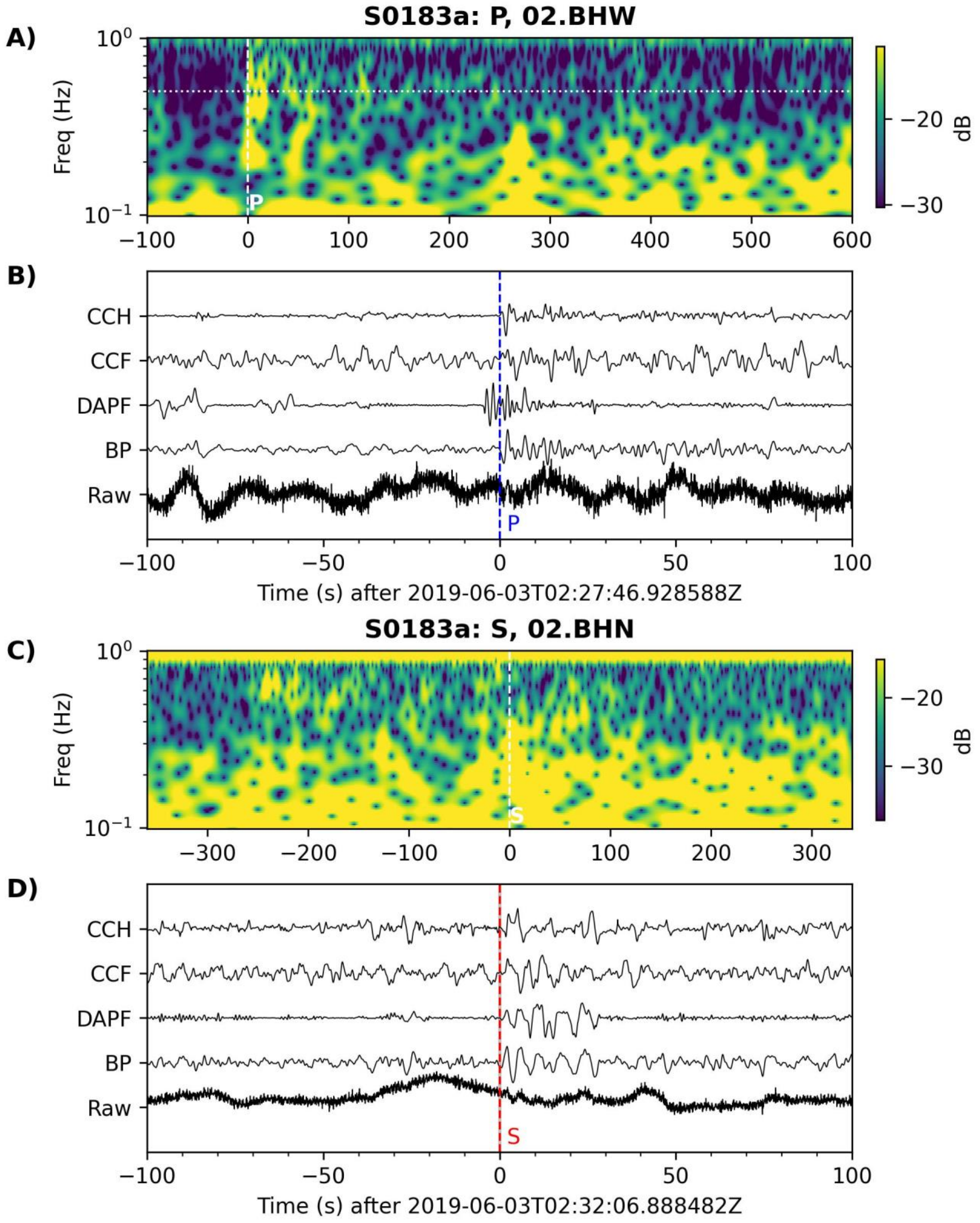

Fig. S3. Same as Fig. S1, but for S0183a.

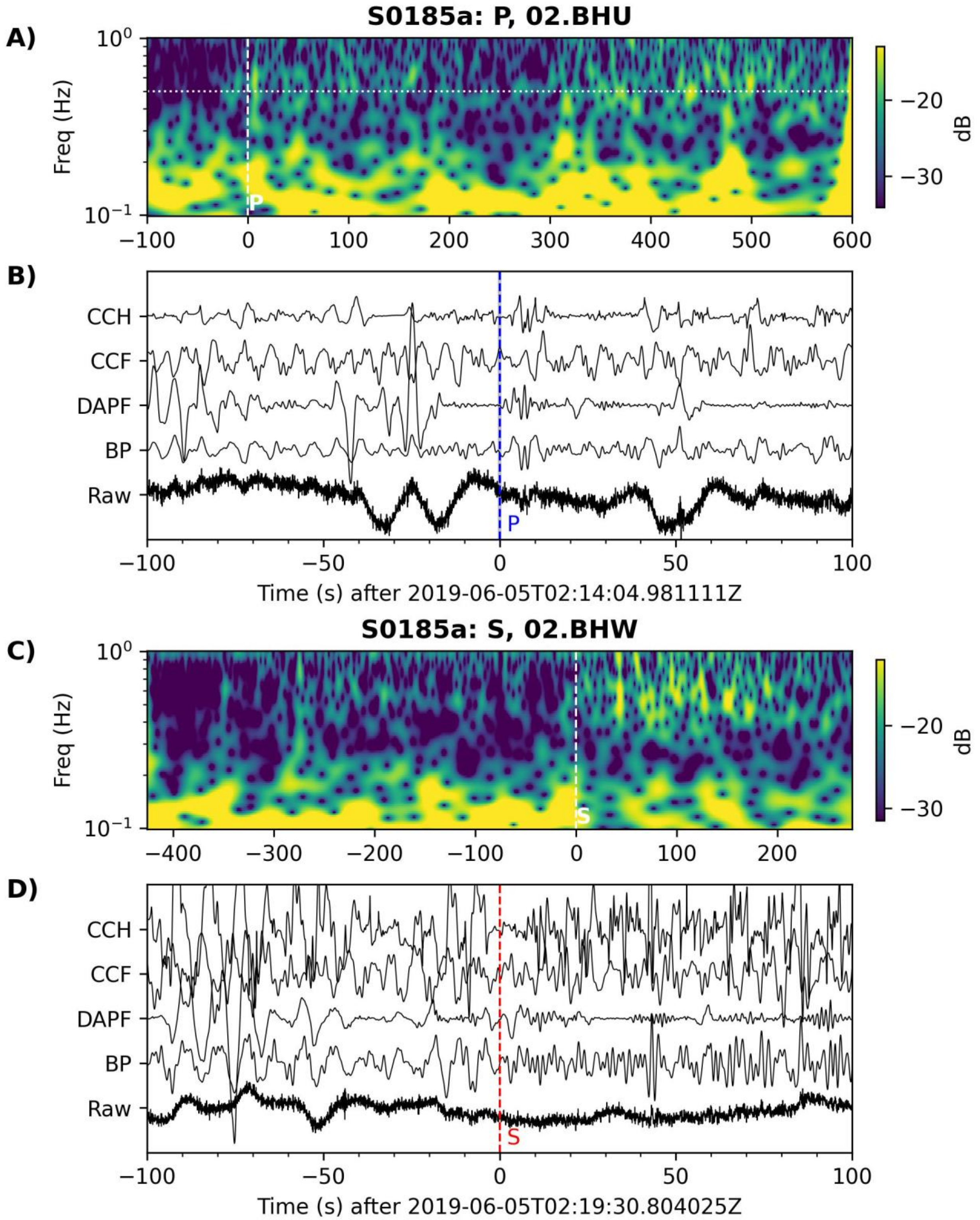

Fig. S4. Same as Fig. S1, but for S0185a.

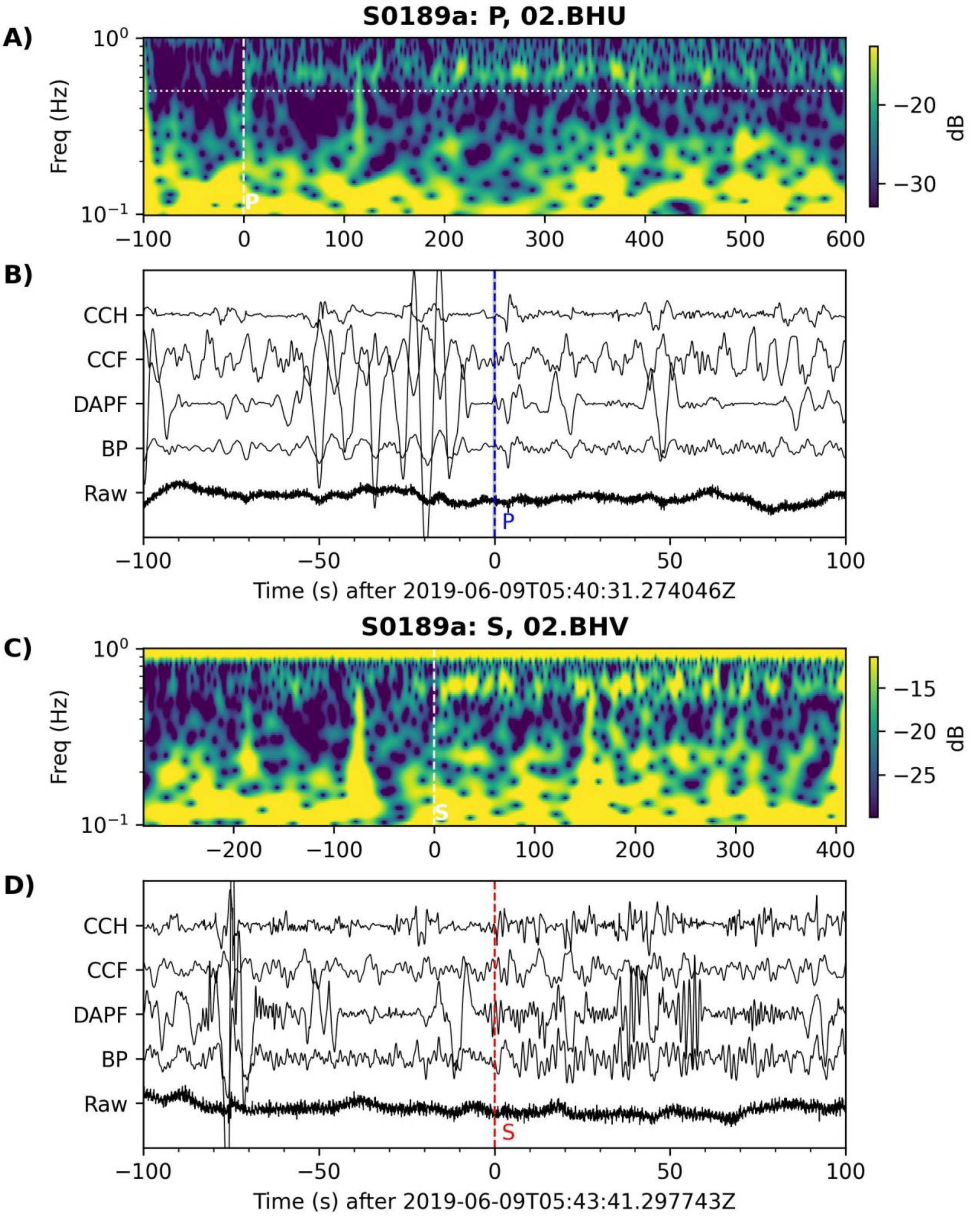

Fig. S5. Same as Fig. S1, but for S0189a.

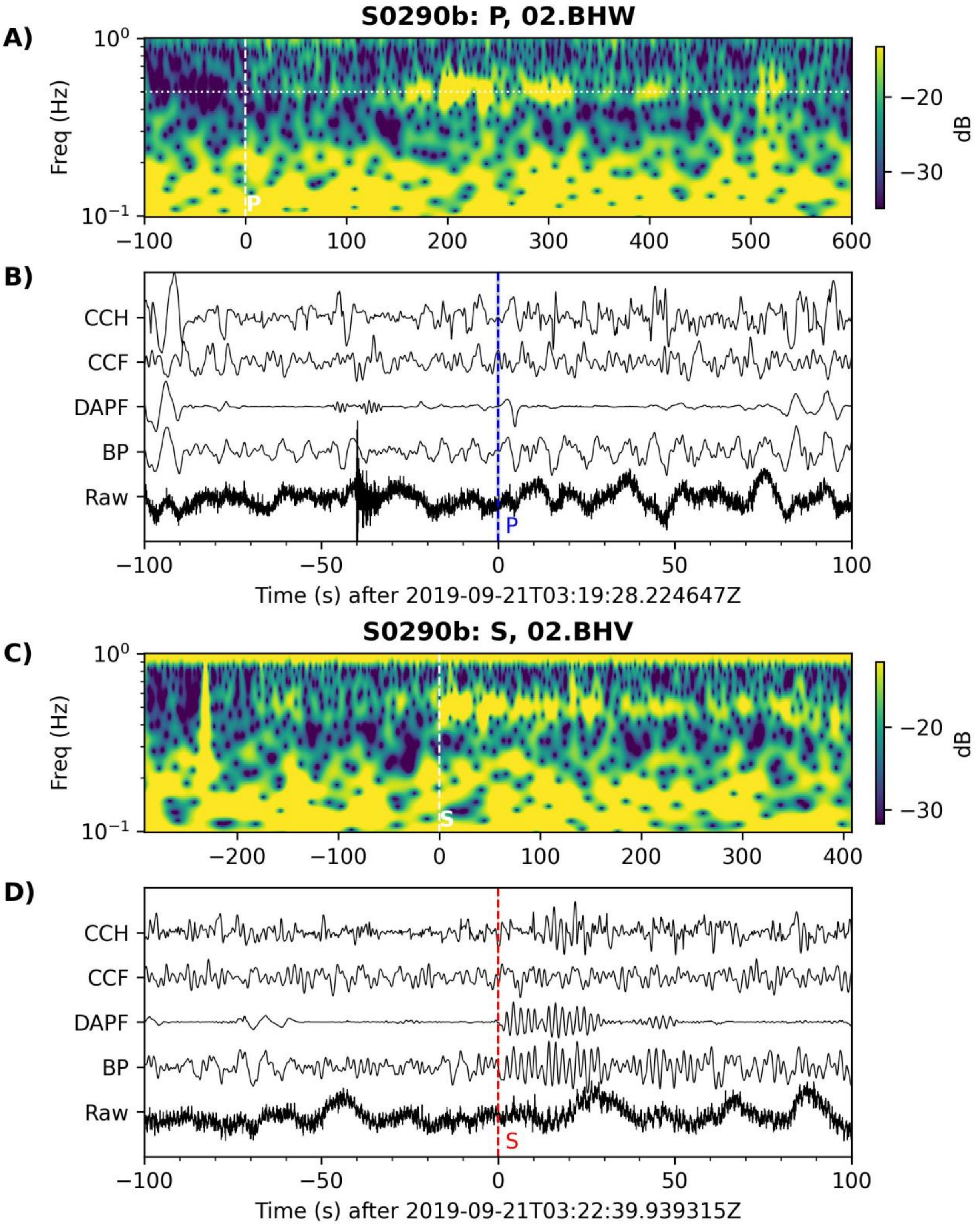

Fig. S6. Same as Fig. S1, but for S0290b.

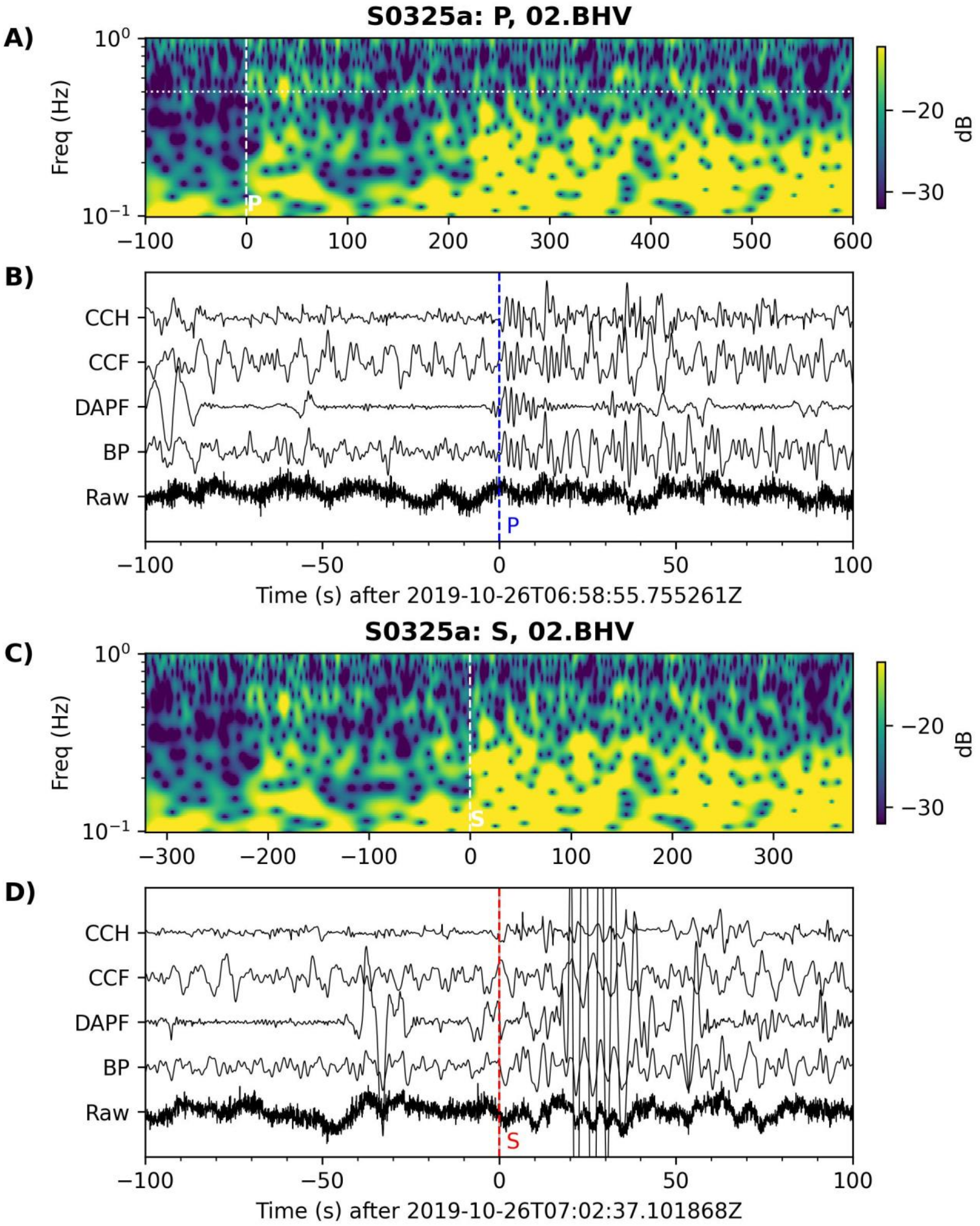

Fig. S7. Same as Fig. S1, but for S0325a.

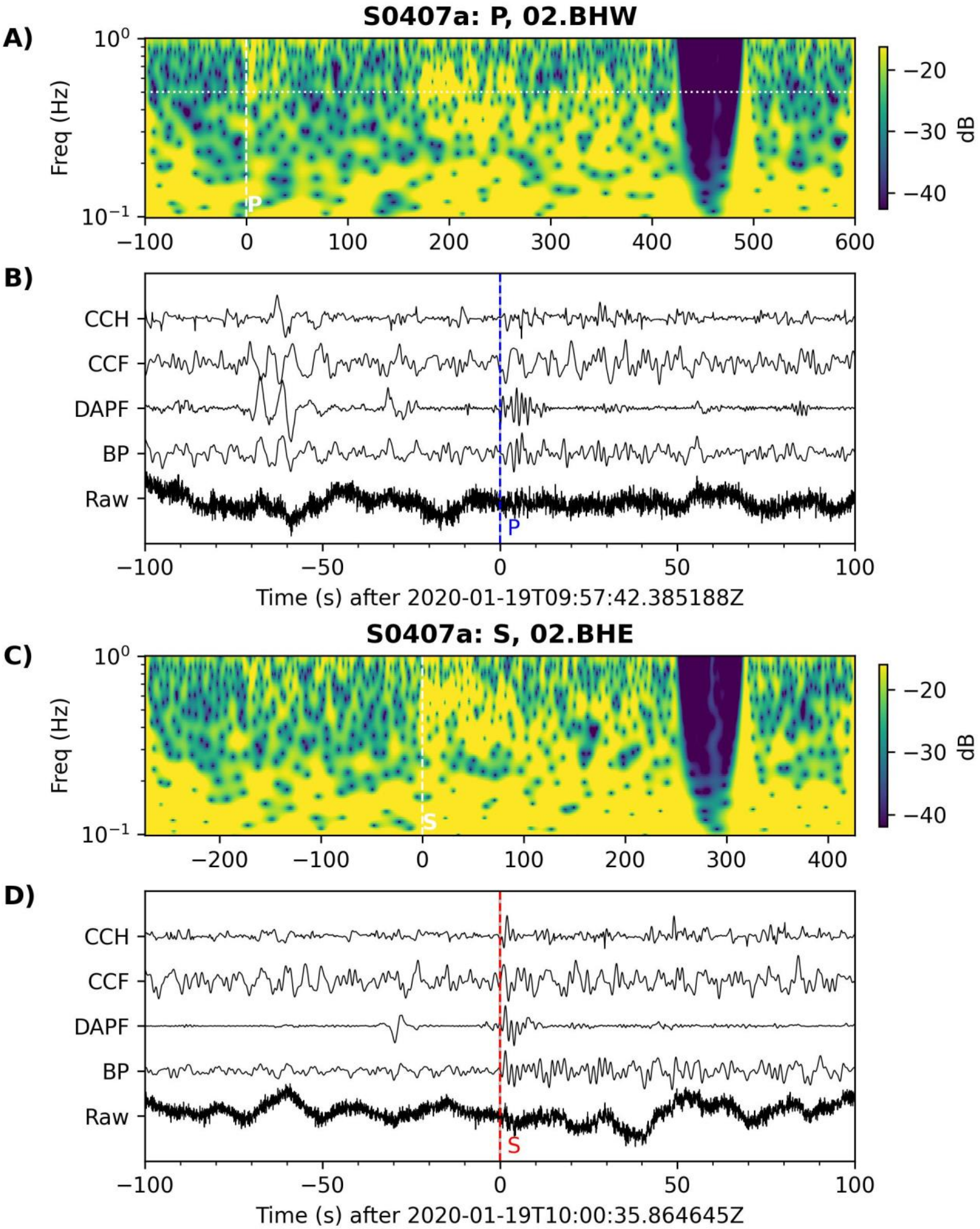

Fig. S8. Same as Fig. S1, but for S0407a.

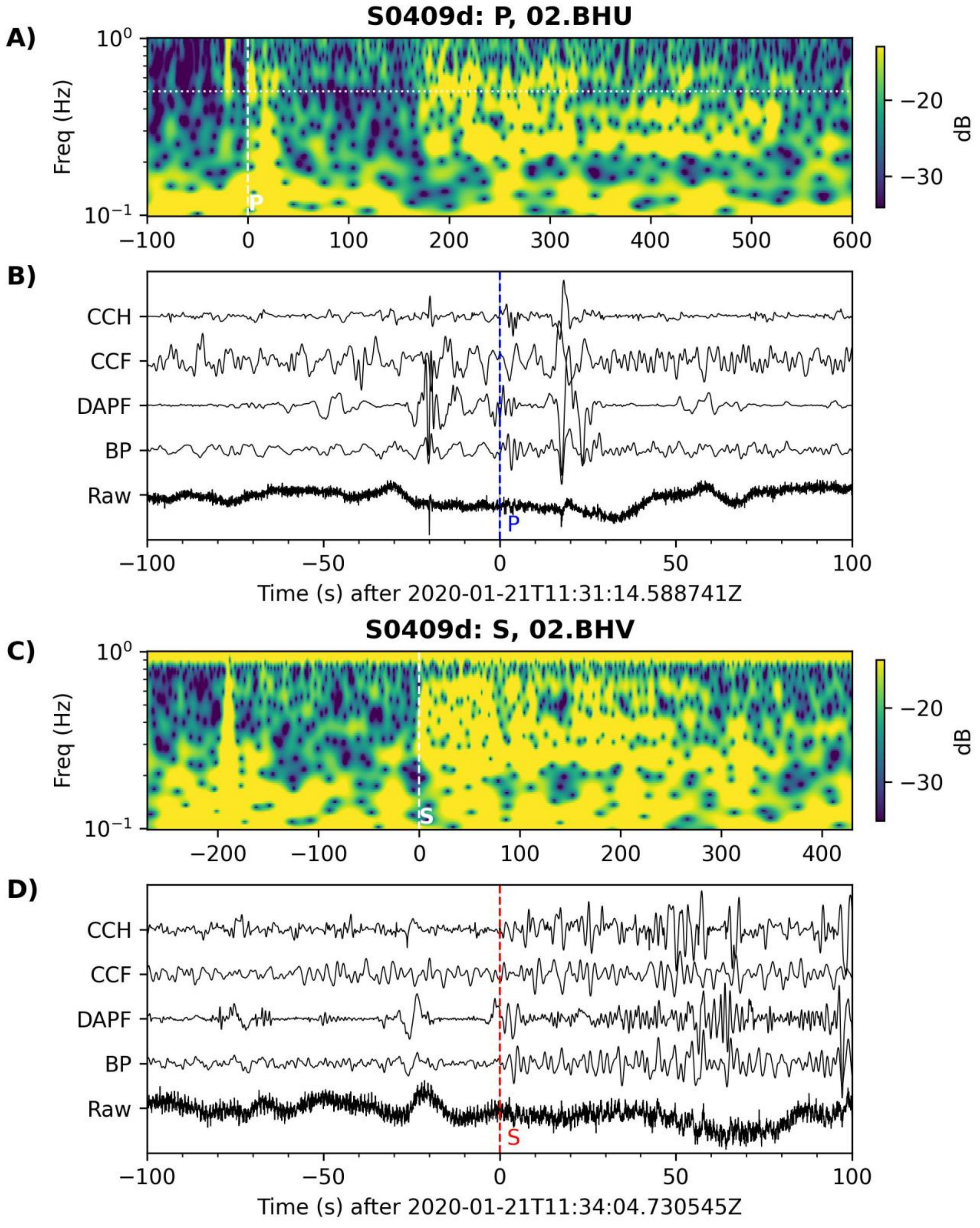

Fig. S9. Same as Fig. S1, but for S0409d.

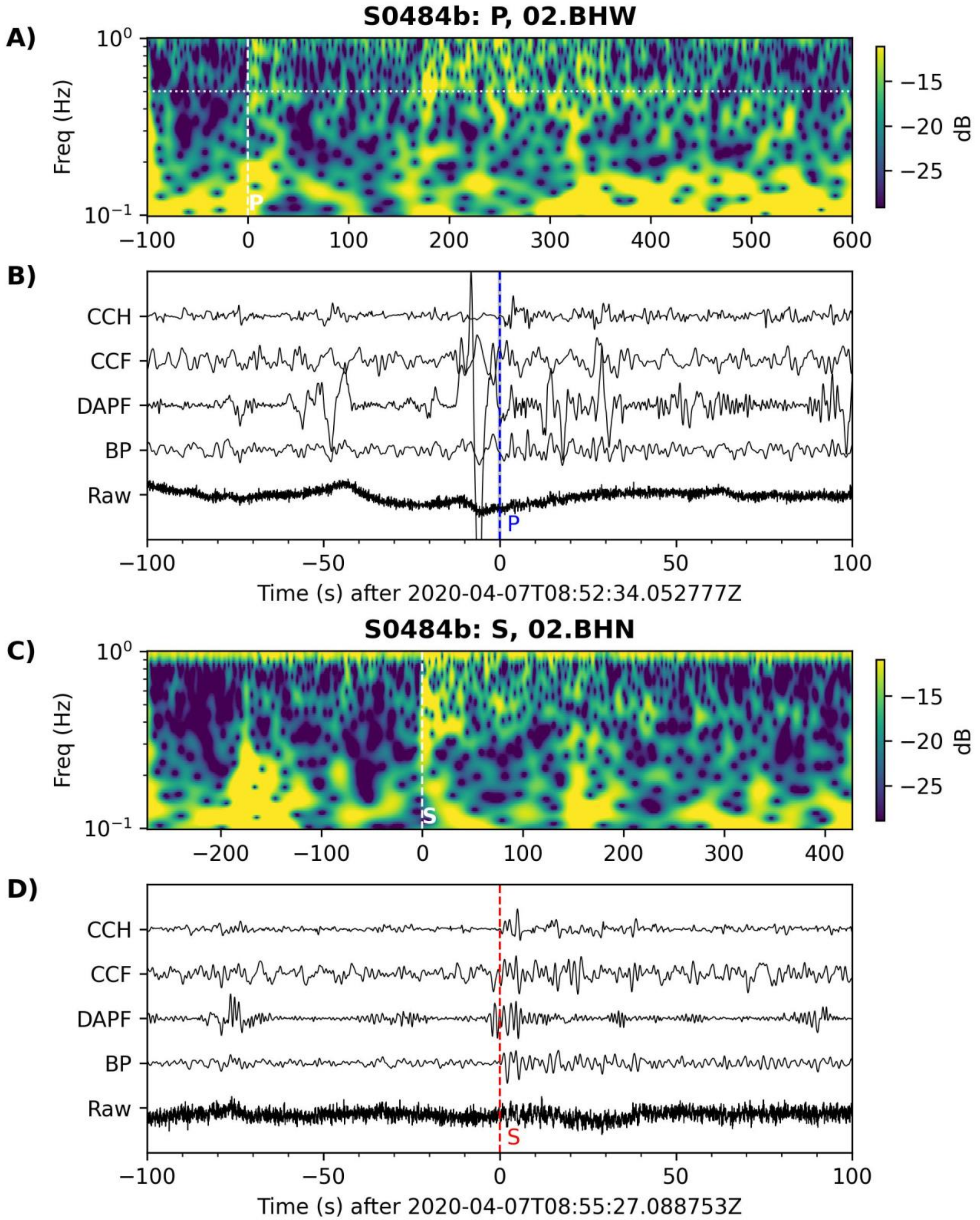

Fig. S10. Same as Fig. S1, but for S0484b.

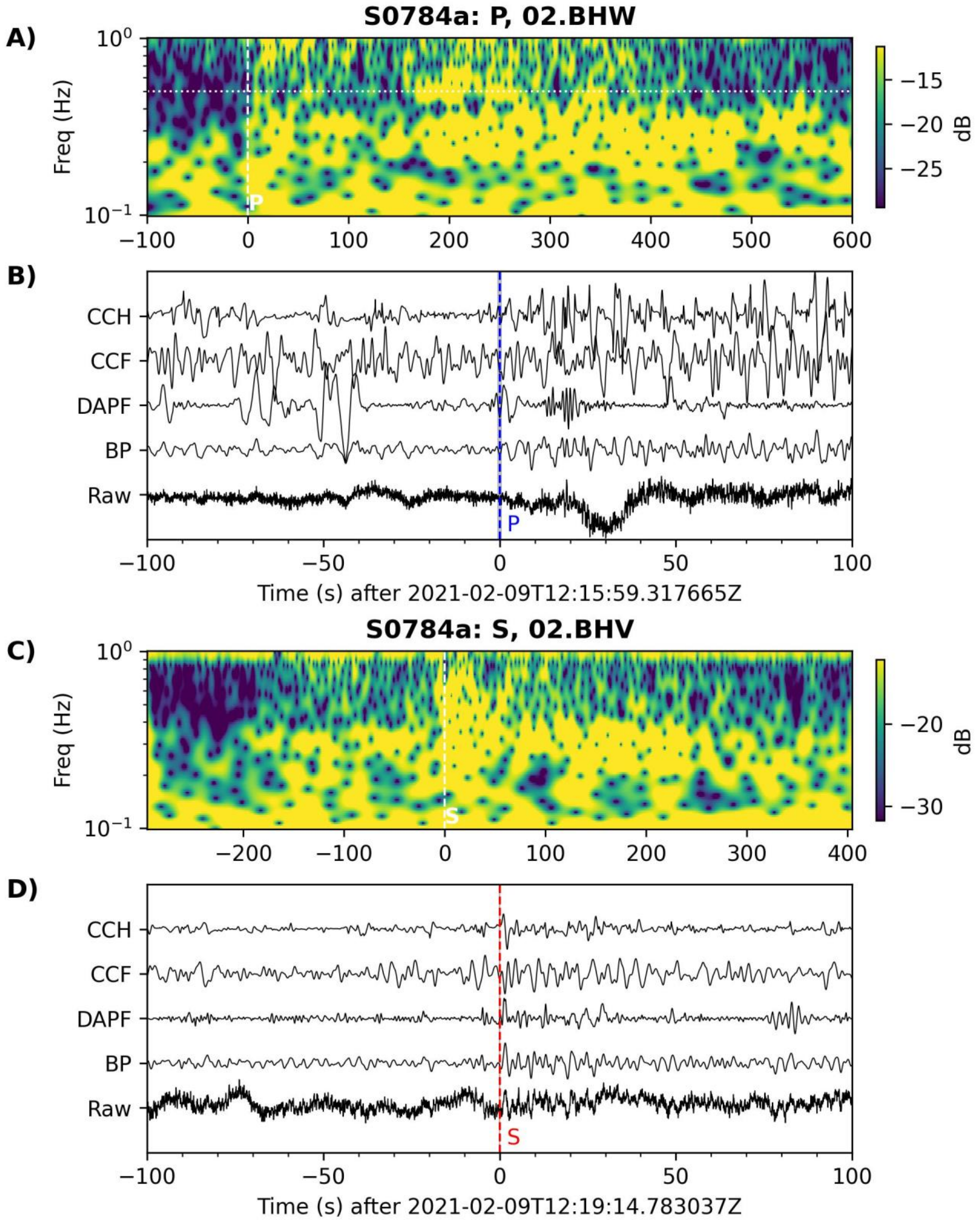

Fig. S11. Same as Fig. S1, but for S0784a.

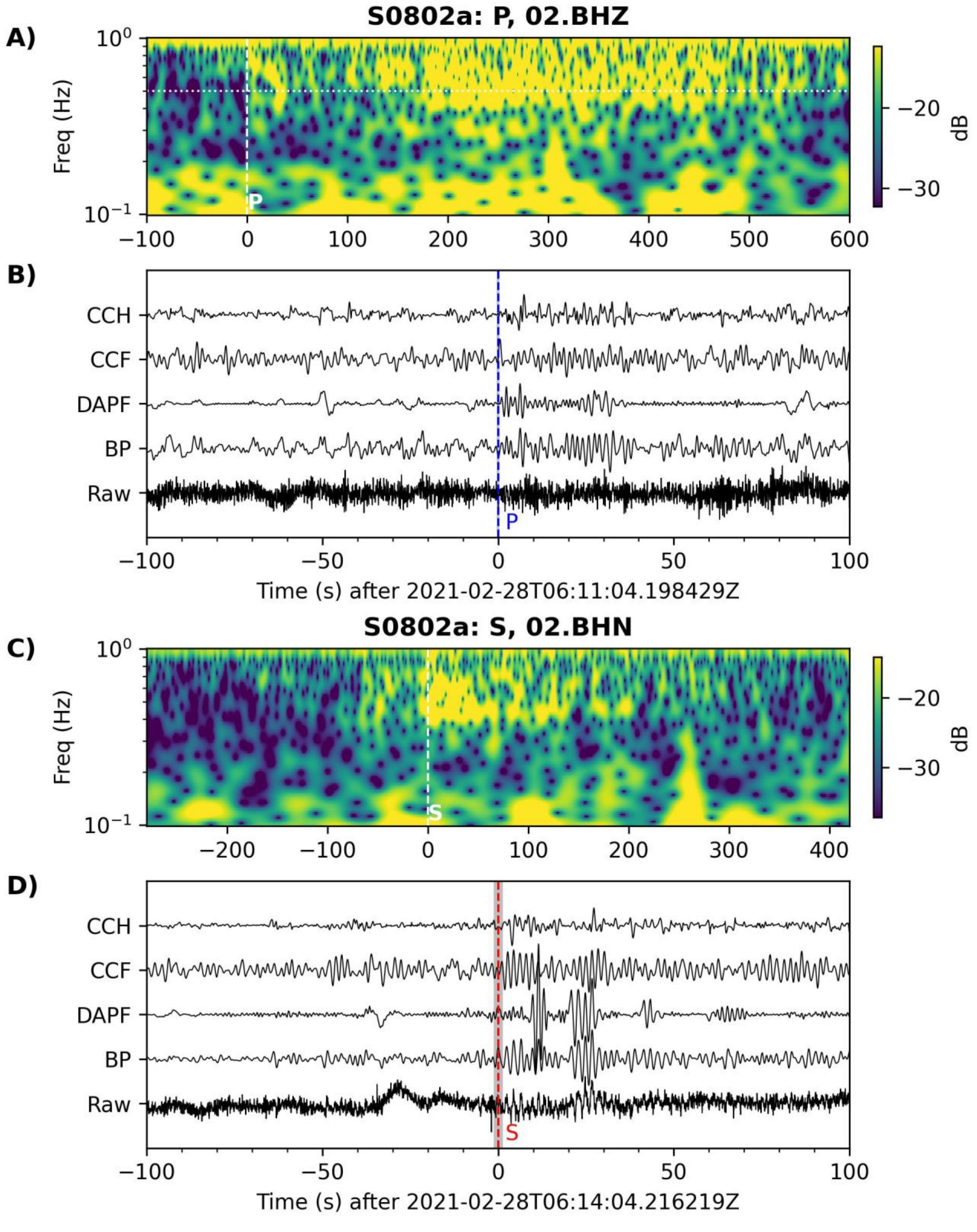

Fig. S12. Same as Fig. S1, but for S0802a.

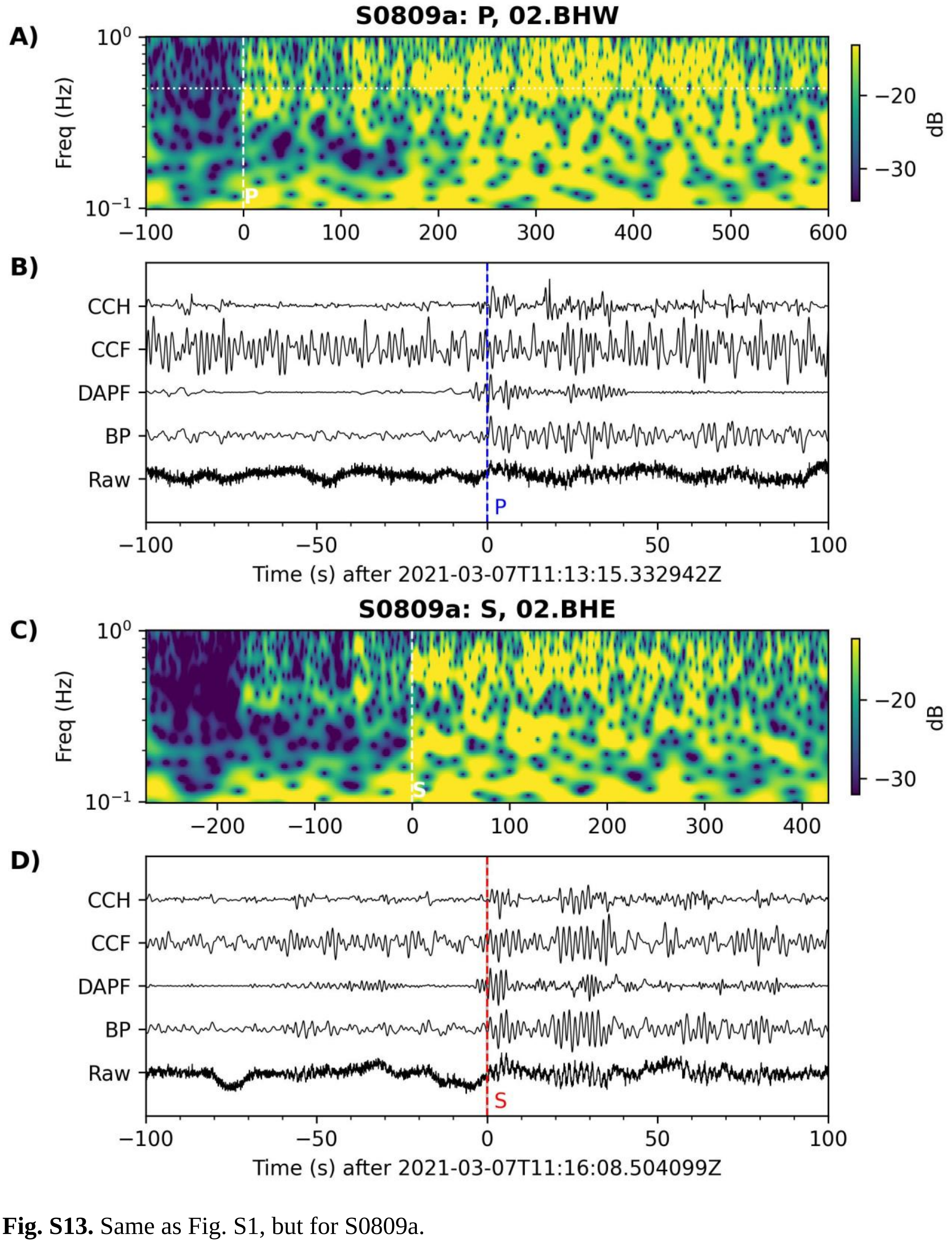

Fig. S13. Same as Fig. S1, but for S0809a.

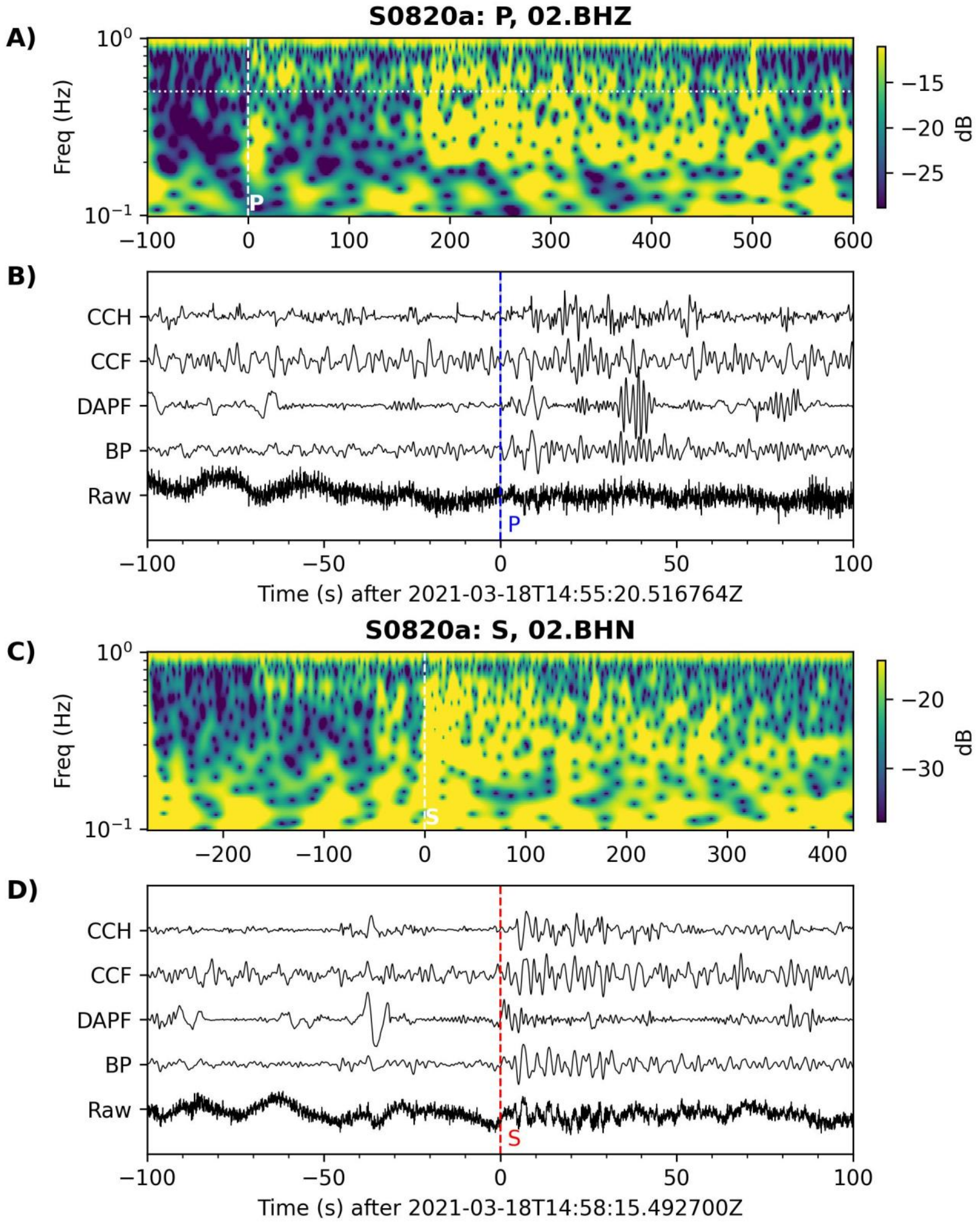

Fig. S14. Same as Fig. S1, but for S0820a.

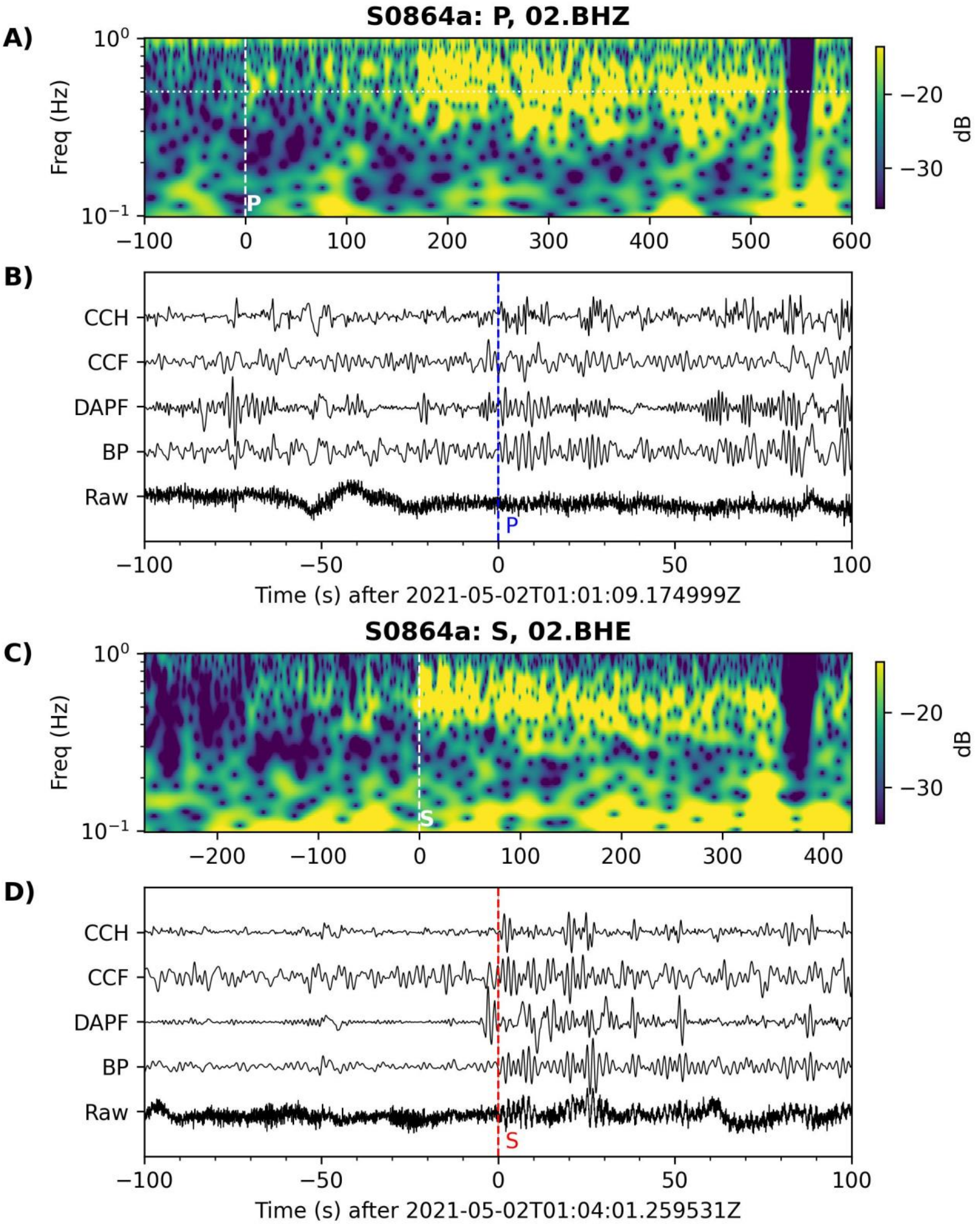

Fig. S15. Same as Fig. S1, but for S0864a.

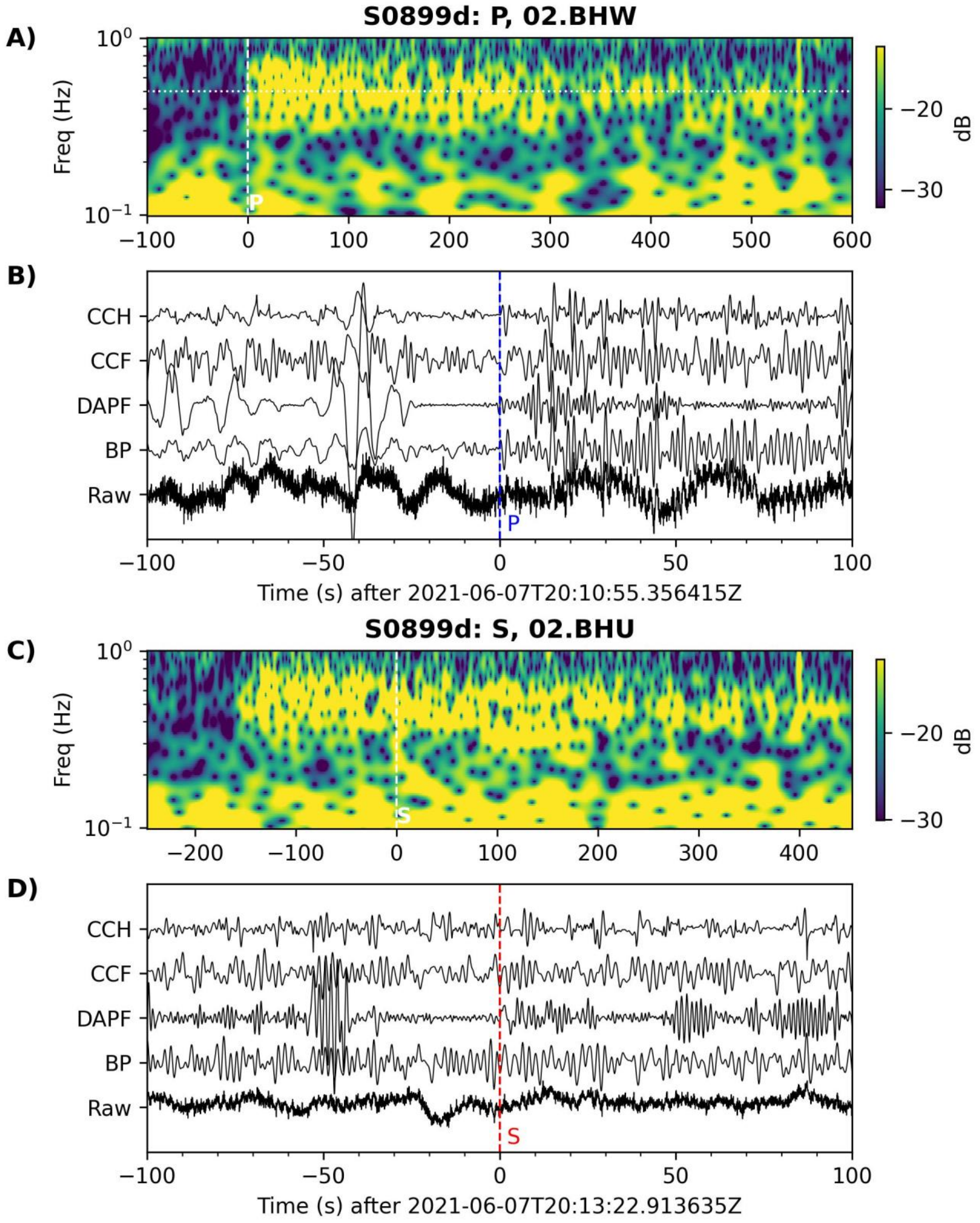

Fig. S16. Same as Fig. S1, but for S0899d.

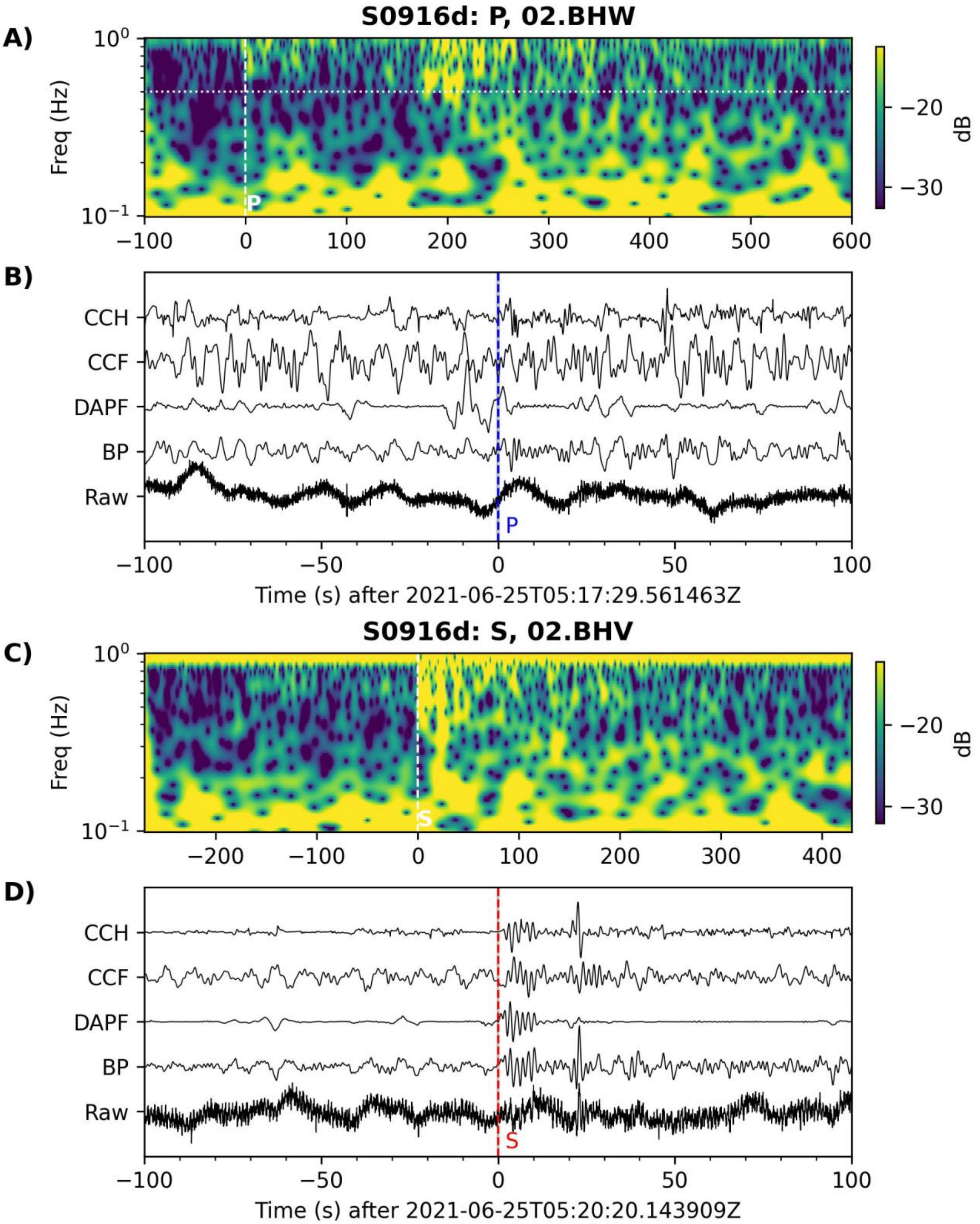

Fig. S17. Same as Fig. S1, but for S0916d.

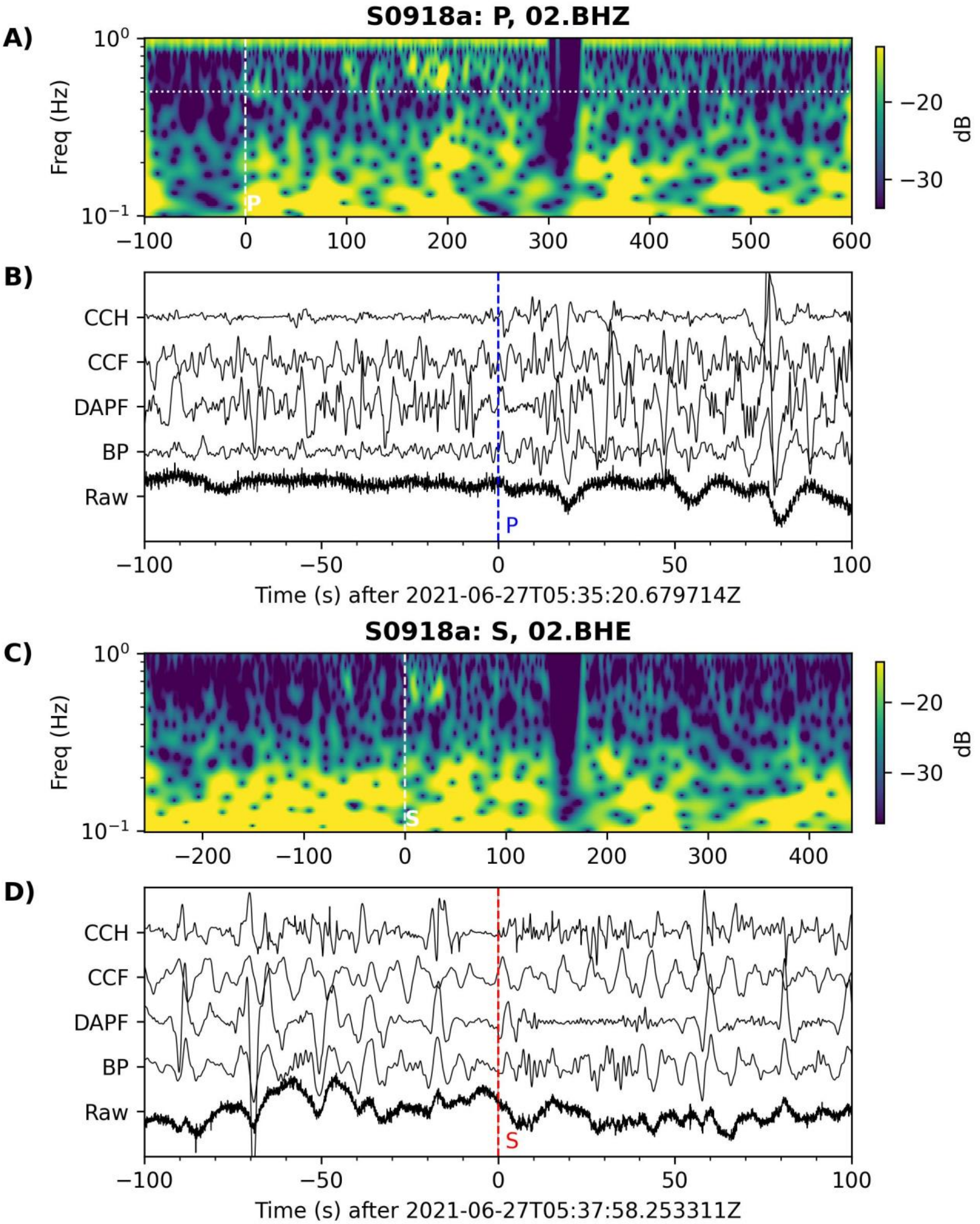

Fig. S18. Same as Fig. S1, but for S0918a.

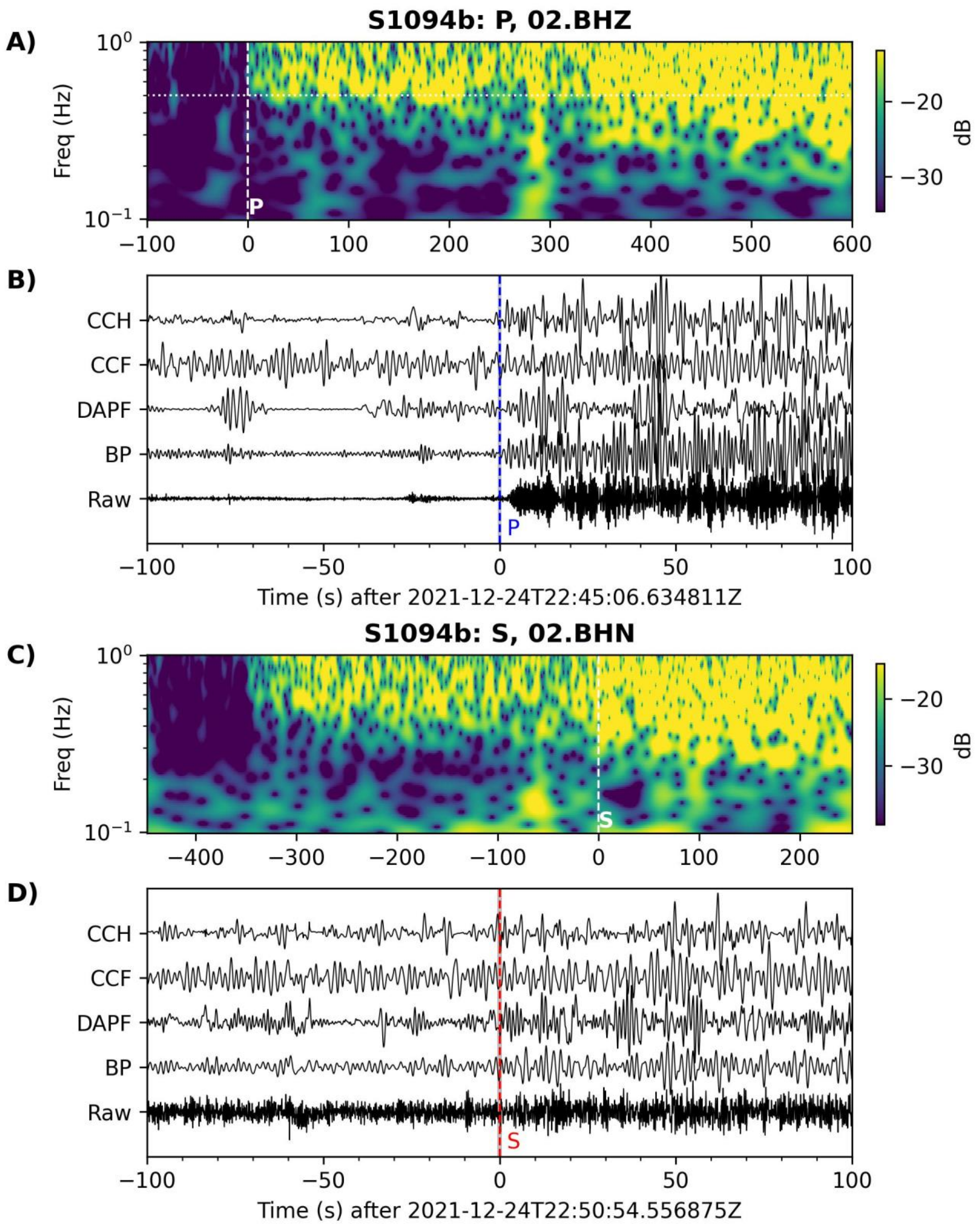

Fig. S19. Same as Fig. S1, but for S1094b.

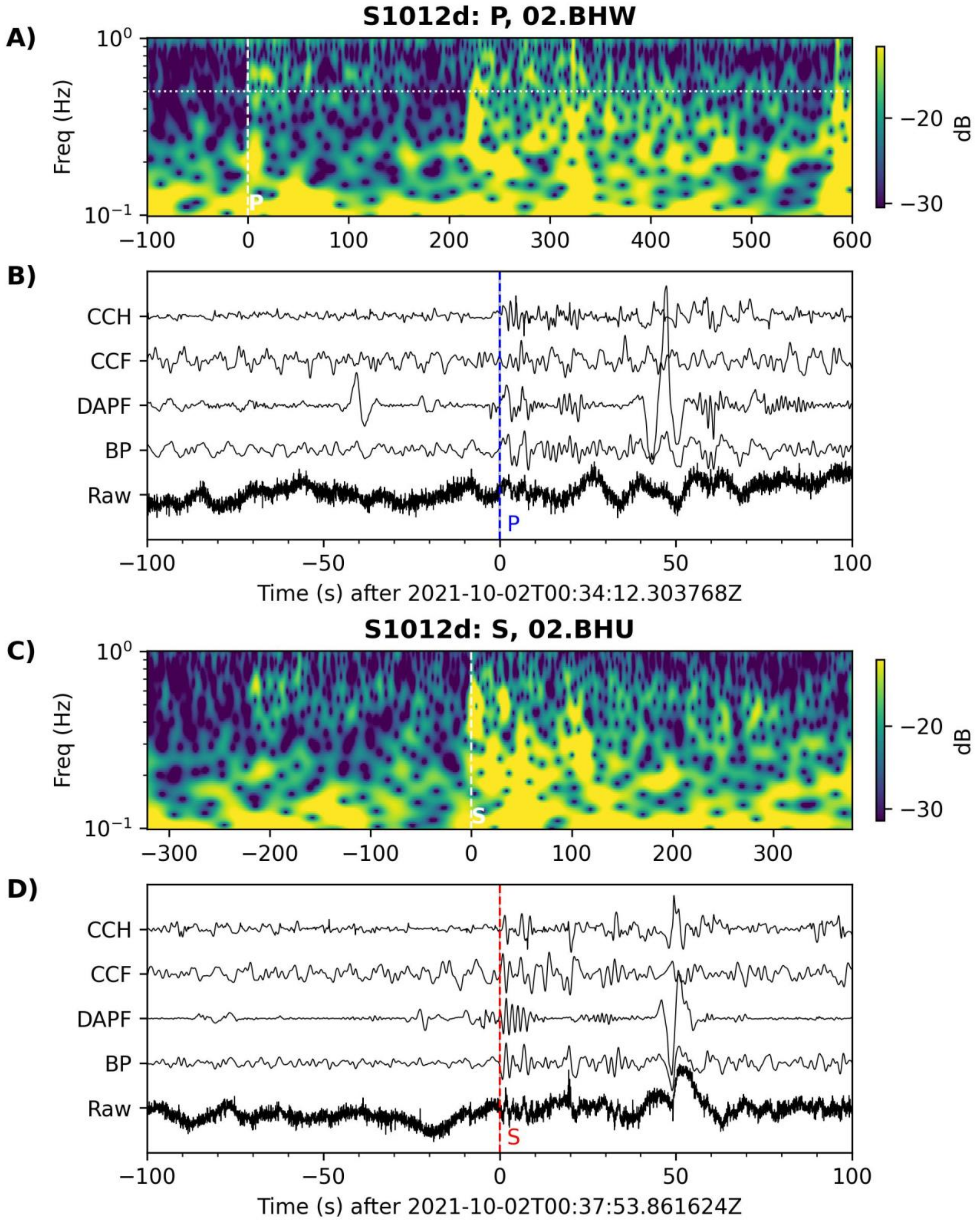

Fig. S20. Same as Fig. S1, but for S1012d.

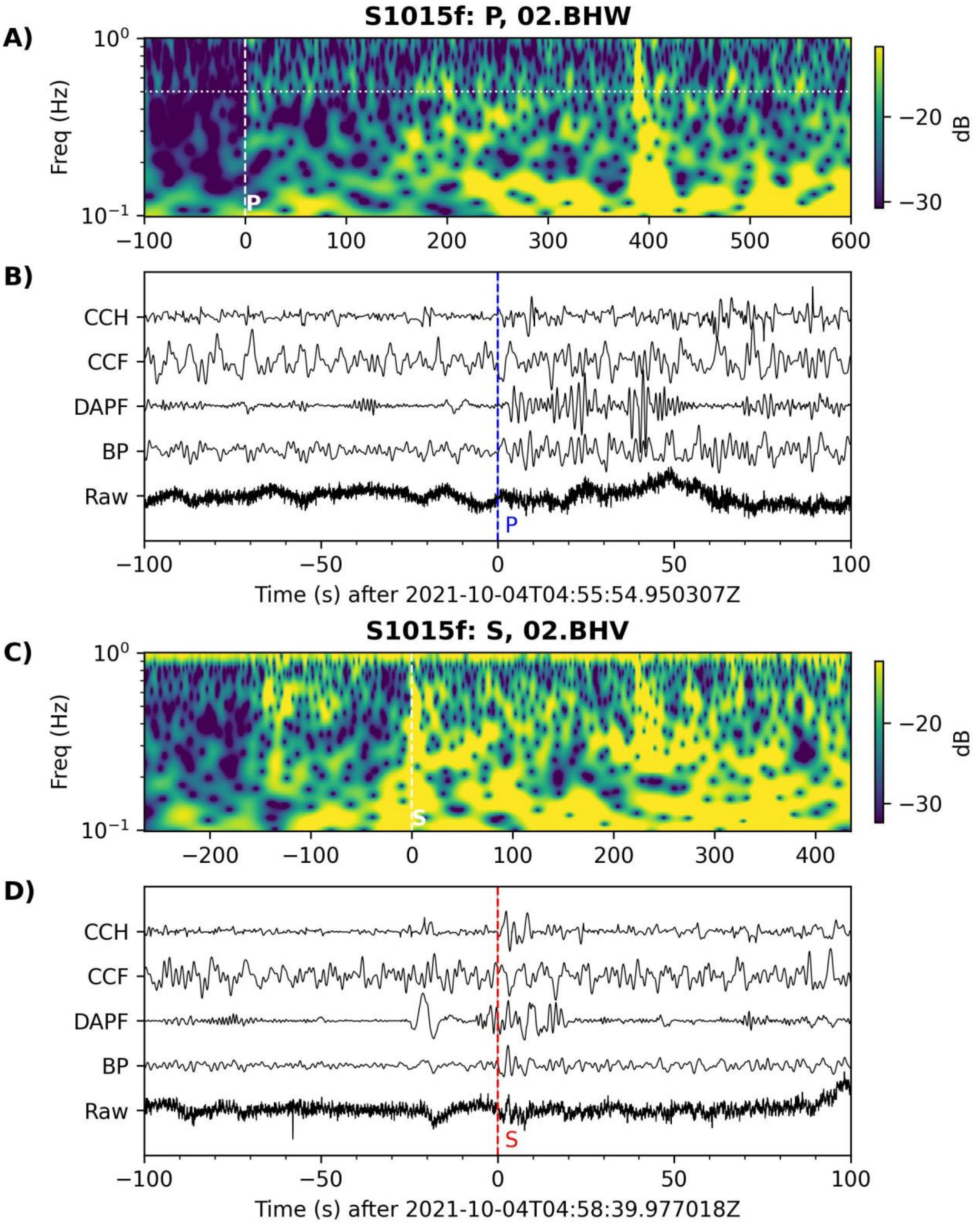

Fig. S21. Same as Fig. S1, but for S1015f.

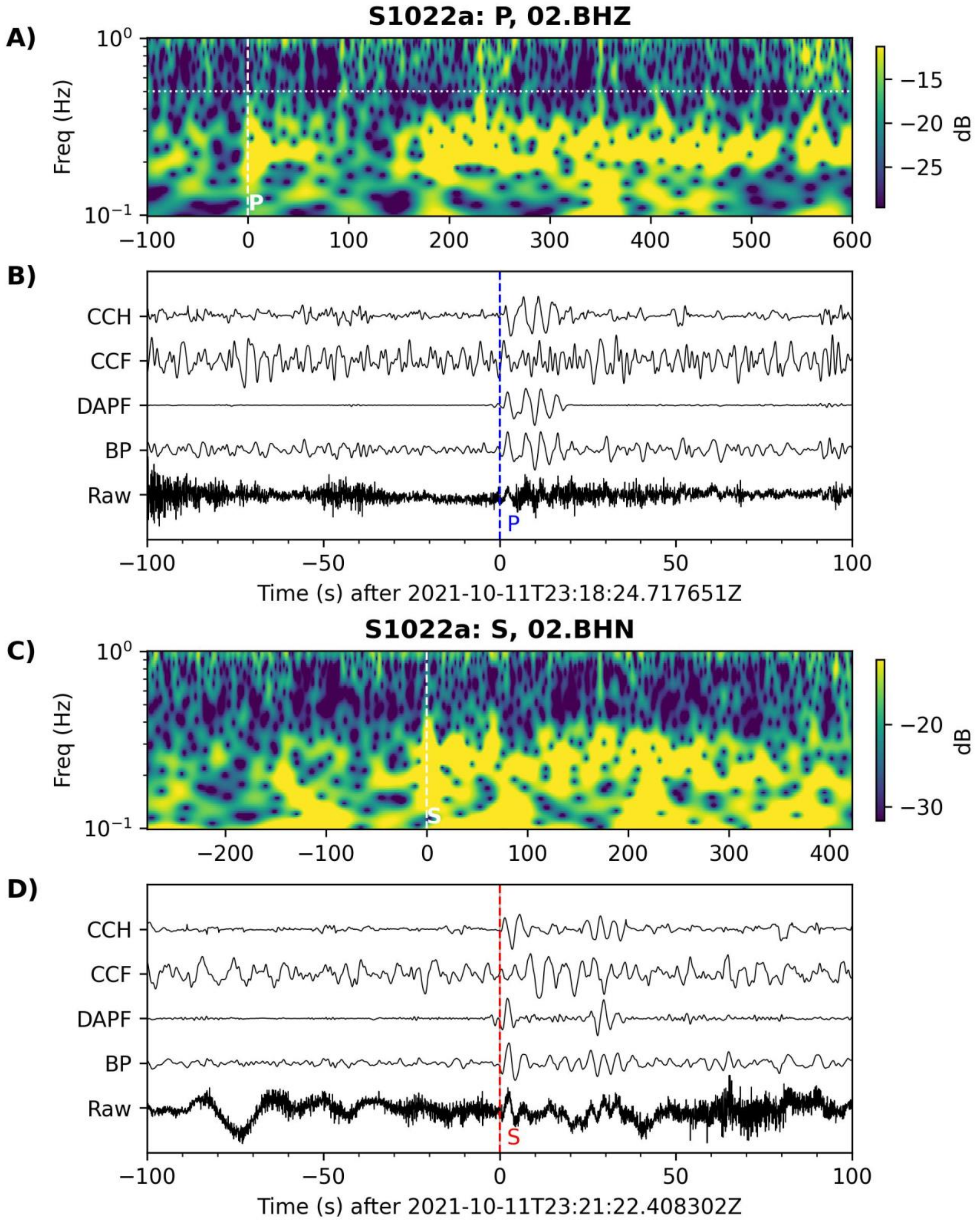

Fig. S22. Same as Fig. S1, but for S1022a.

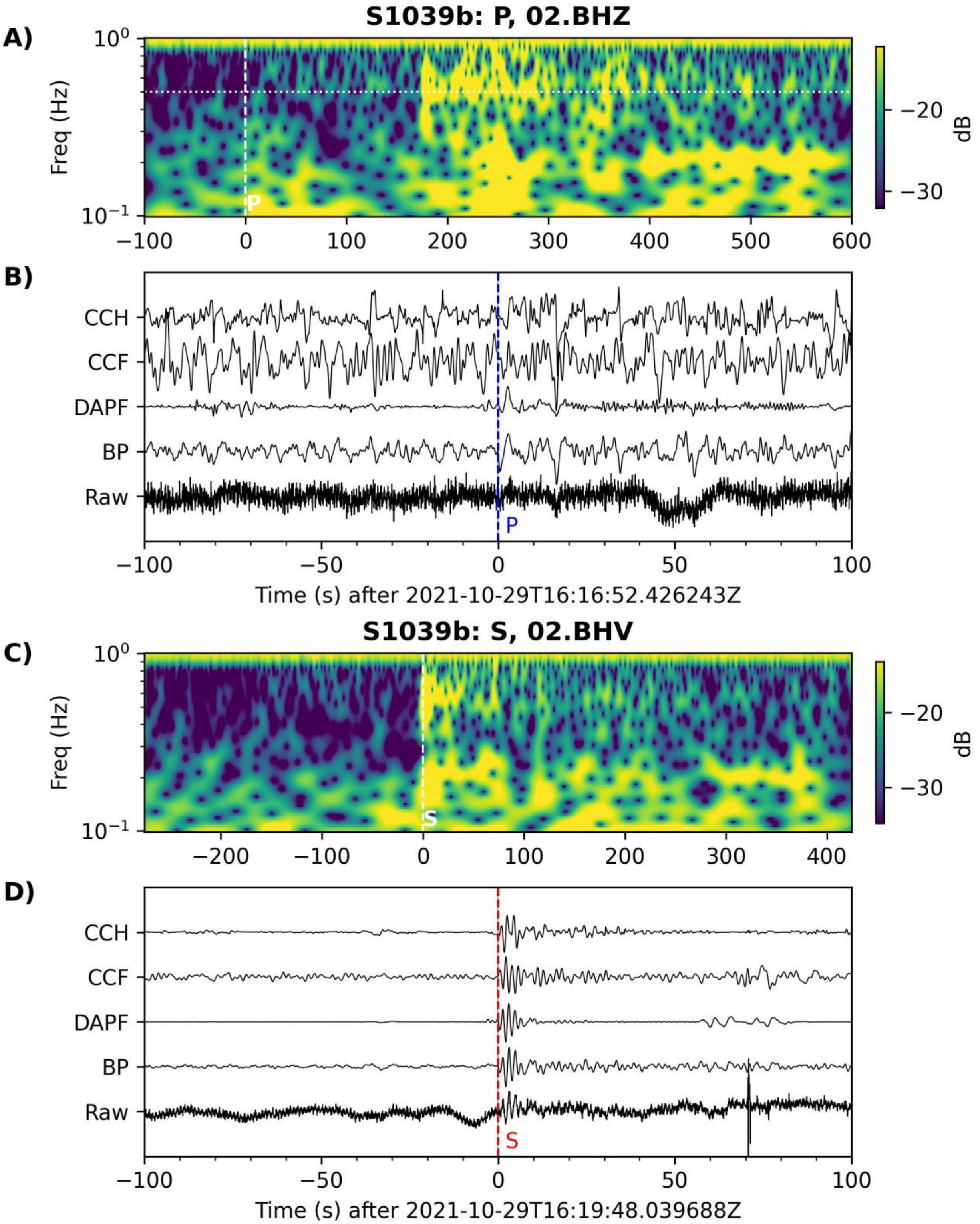

Fig. S23. Same as Fig. S1, but for S1039b.

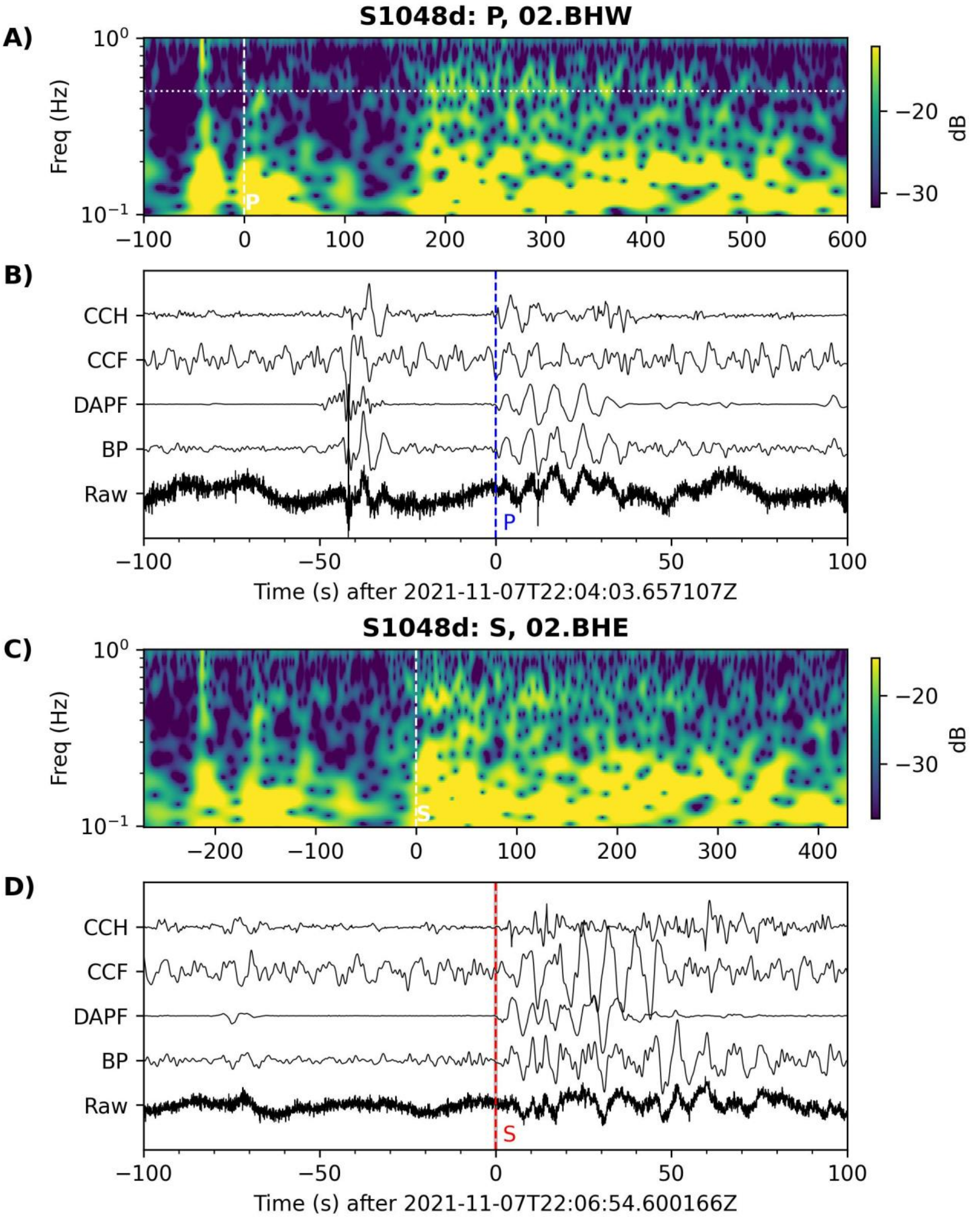

Fig. S24. Same as Fig. S1, but for S1048d.

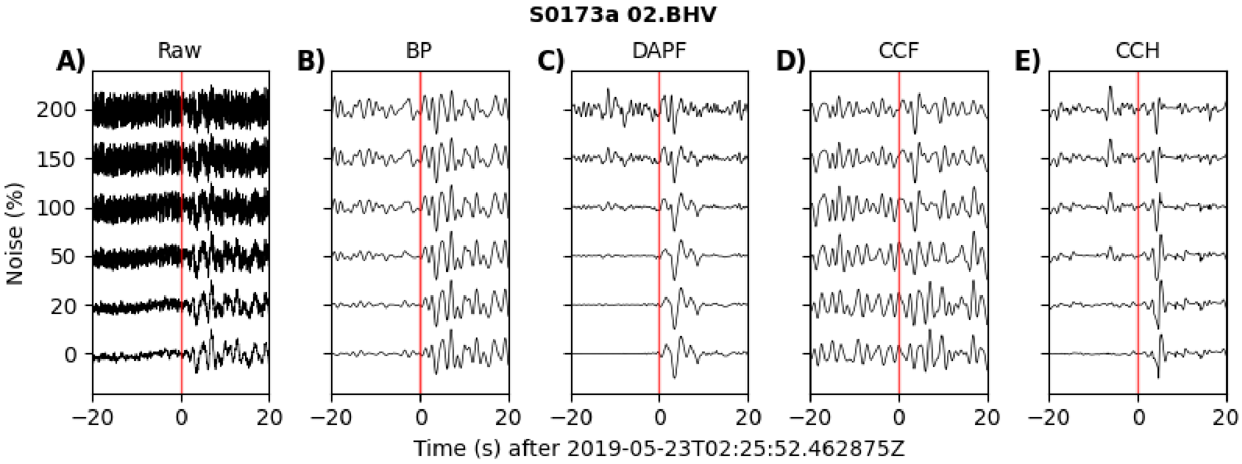

Fig. S25. Test of noise (given in percent of signal) influence on multiple filter methods used for travel-time picks.

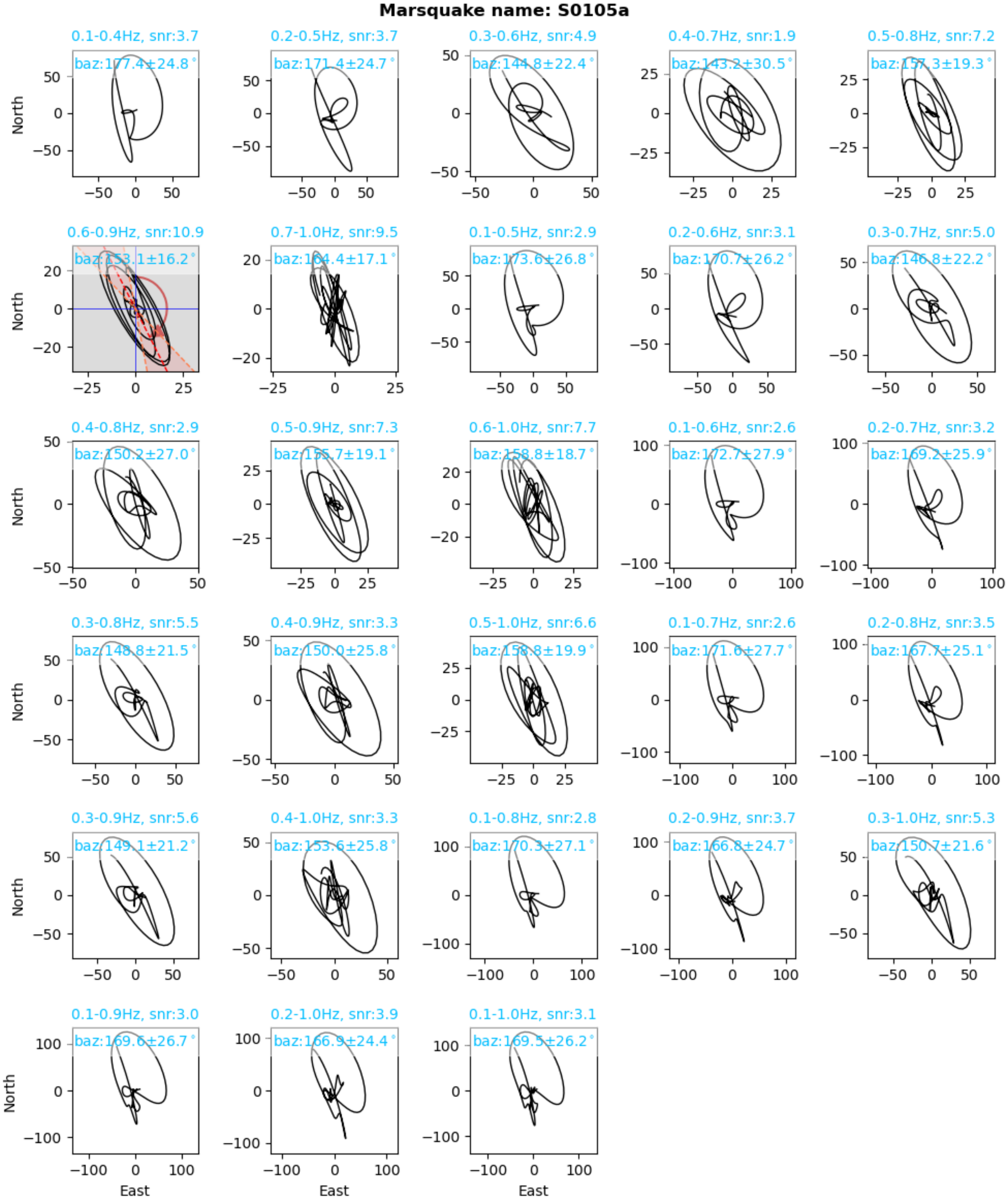

Fig. S26. Estimation of back azimuth by selecting the optimal frequency band. The frequency band, signal-to-noise ratio, and back azimuth with uncertainty are labeled on the top of each subfigure.

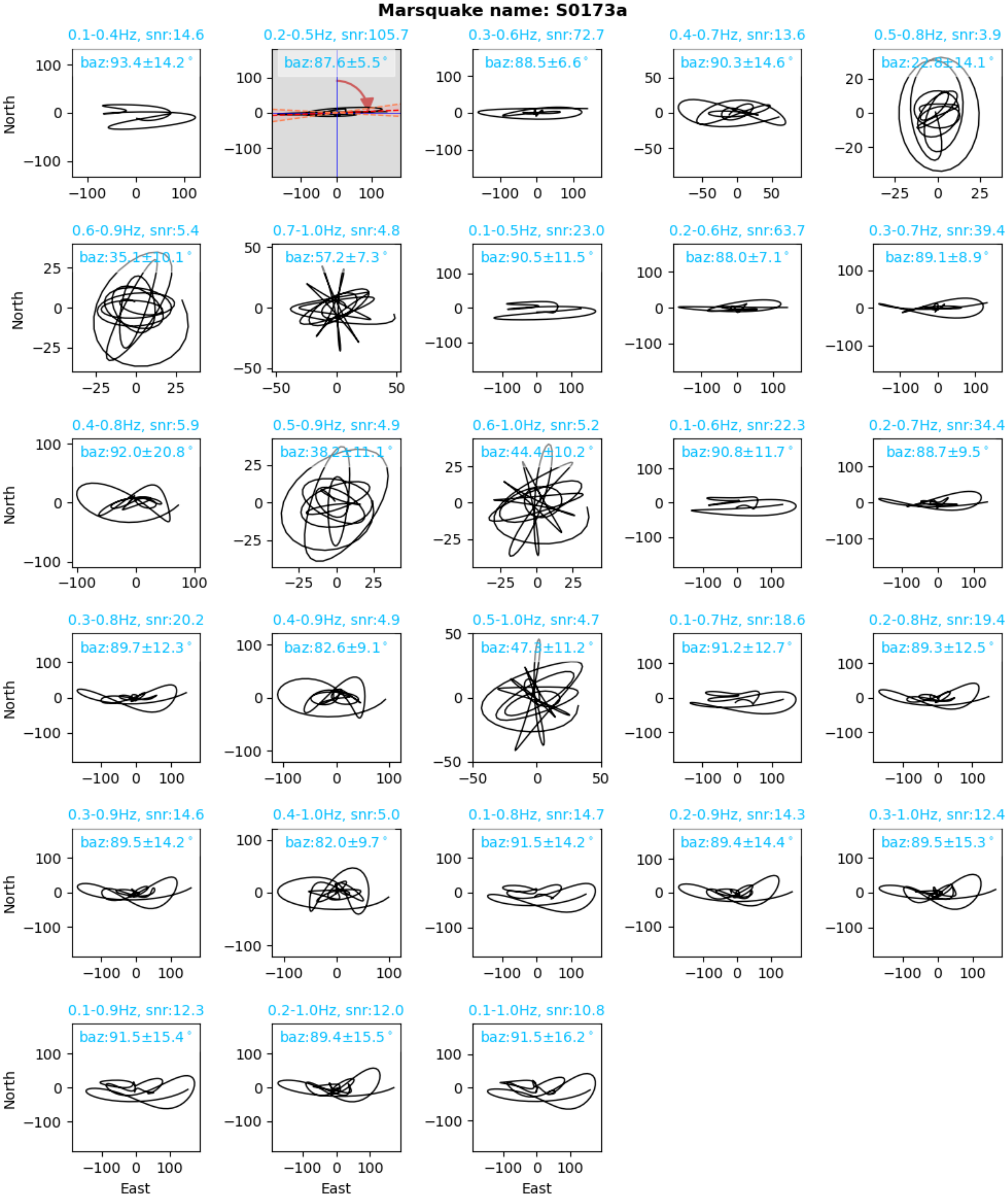

Fig. S27. Same as Fig. S26, but for S0173a.

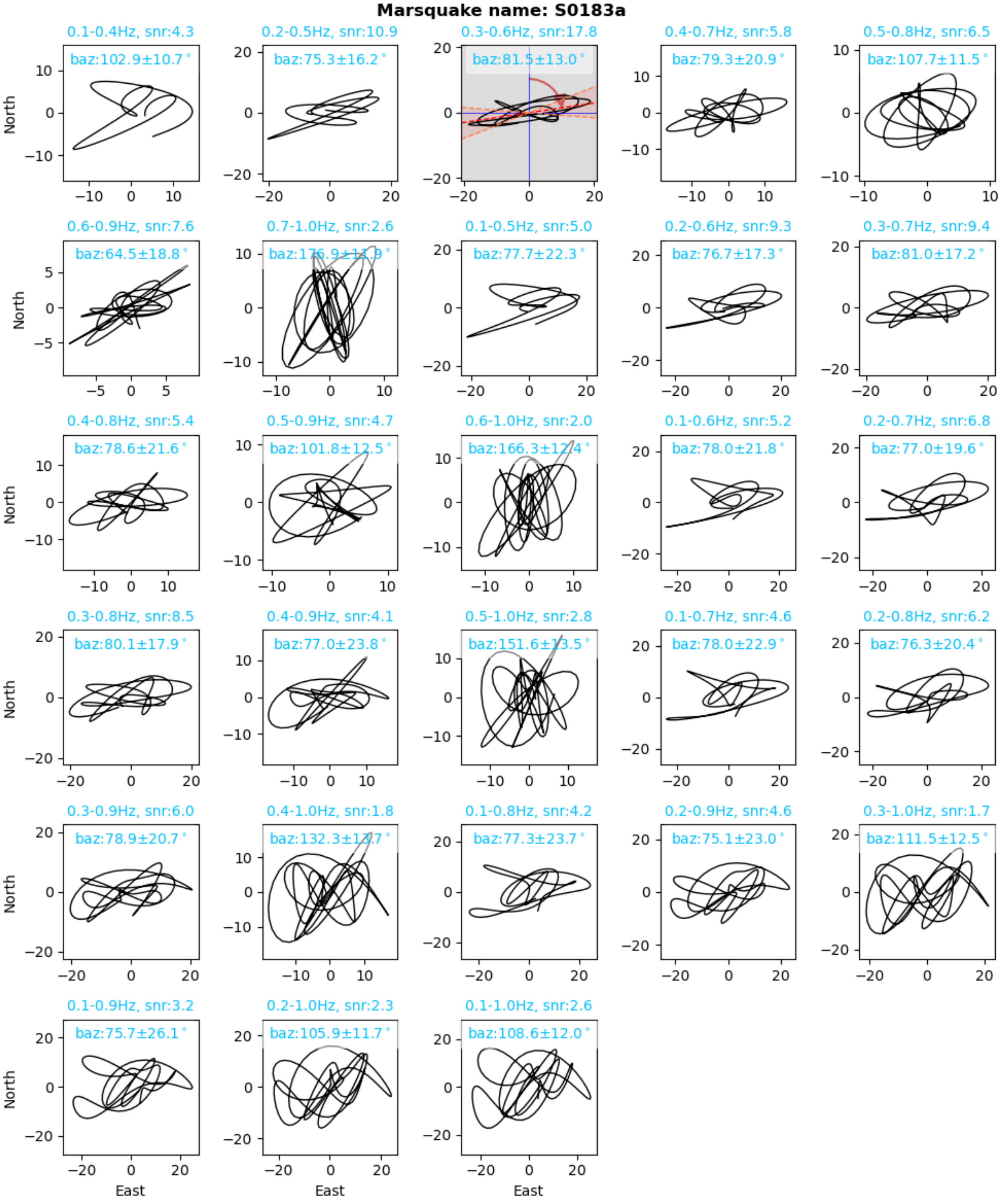

Fig. S28. Same as Fig. S26, but for S0183a.

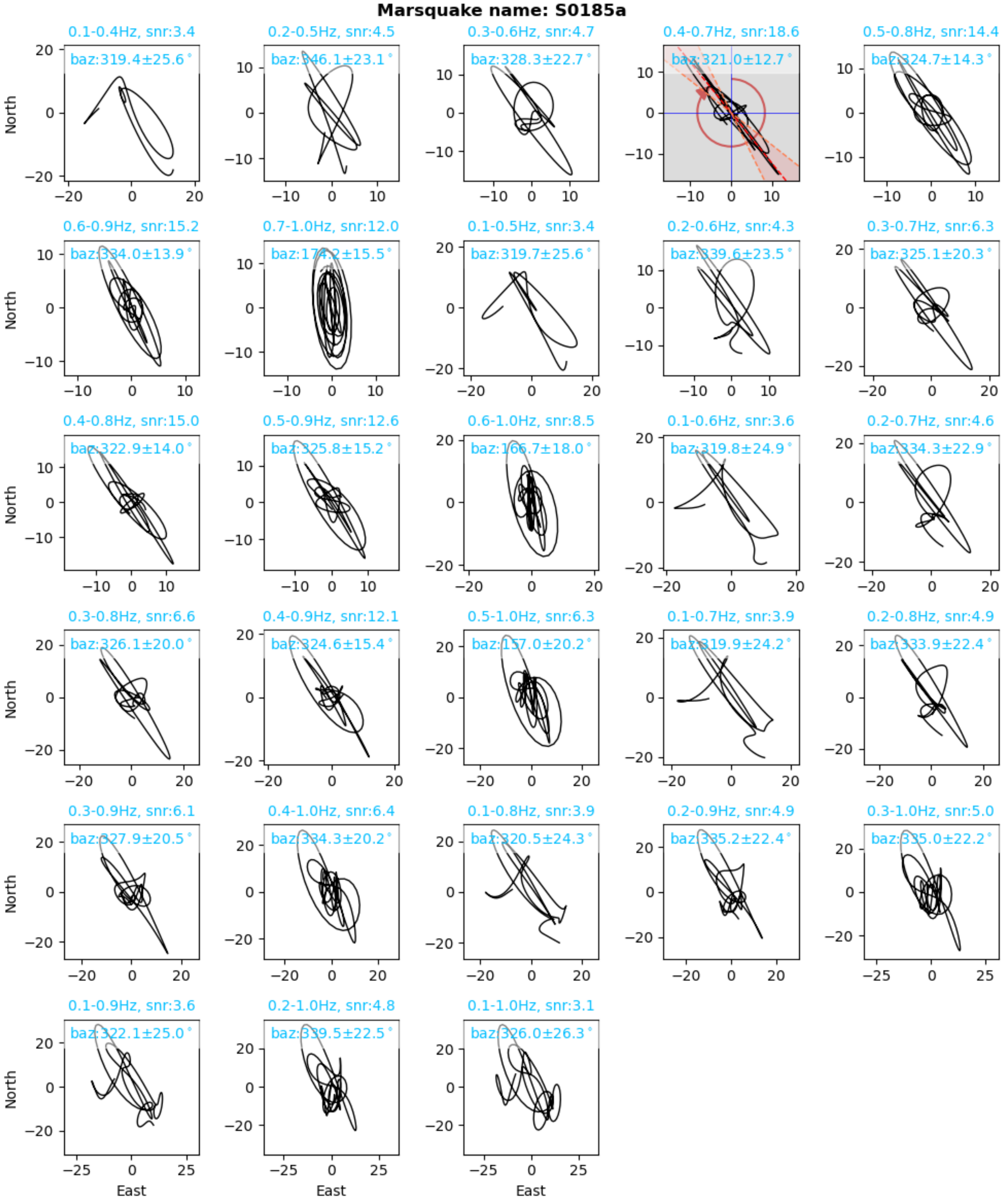

Fig. S29. Same as Fig. S26, but for S0185a.


Marsquake name: S0189a

0.1-0.4Hz, snr:4.9
0.2-0.5Hz, snr:18.4
0.3-0.6Hz, snr:7.9
0.4-0.7Hz, snr:4.4
0.5-0.8Hz, snr:8.2
0.6-0.9Hz, snr:4.1
0.7-1.0Hz, snr:11.2
0.1-0.5Hz, snr:5.0
0.2-0.6Hz, snr:9.9
0.3-0.7Hz, snr:4.4
0.4-0.8Hz, snr:3.8
0.5-0.9Hz, snr:3.5
0.6-1.0Hz, snr:4.4
0.1-0.6Hz, snr:4.8
0.2-0.7Hz, snr:5.9
0.3-0.8Hz, snr:3.9
0.4-0.9Hz, snr:2.8
0.5-1.0Hz, snr:2.1
0.1-0.7Hz, snr:4.4
0.2-0.8Hz, snr:4.9
0.3-0.9Hz, snr:3.3
0.4-1.0Hz, snr:2.5
0.1-0.8Hz, snr:4.2
0.2-0.9Hz, snr:4.7
0.3-1.0Hz, snr:3.3
0.1-0.9Hz, snr:4.0
0.2-1.0Hz, snr:5.0
0.1-1.0Hz, snr:3.7

Fig. S30. Same as Fig. S26, but for S0189a.

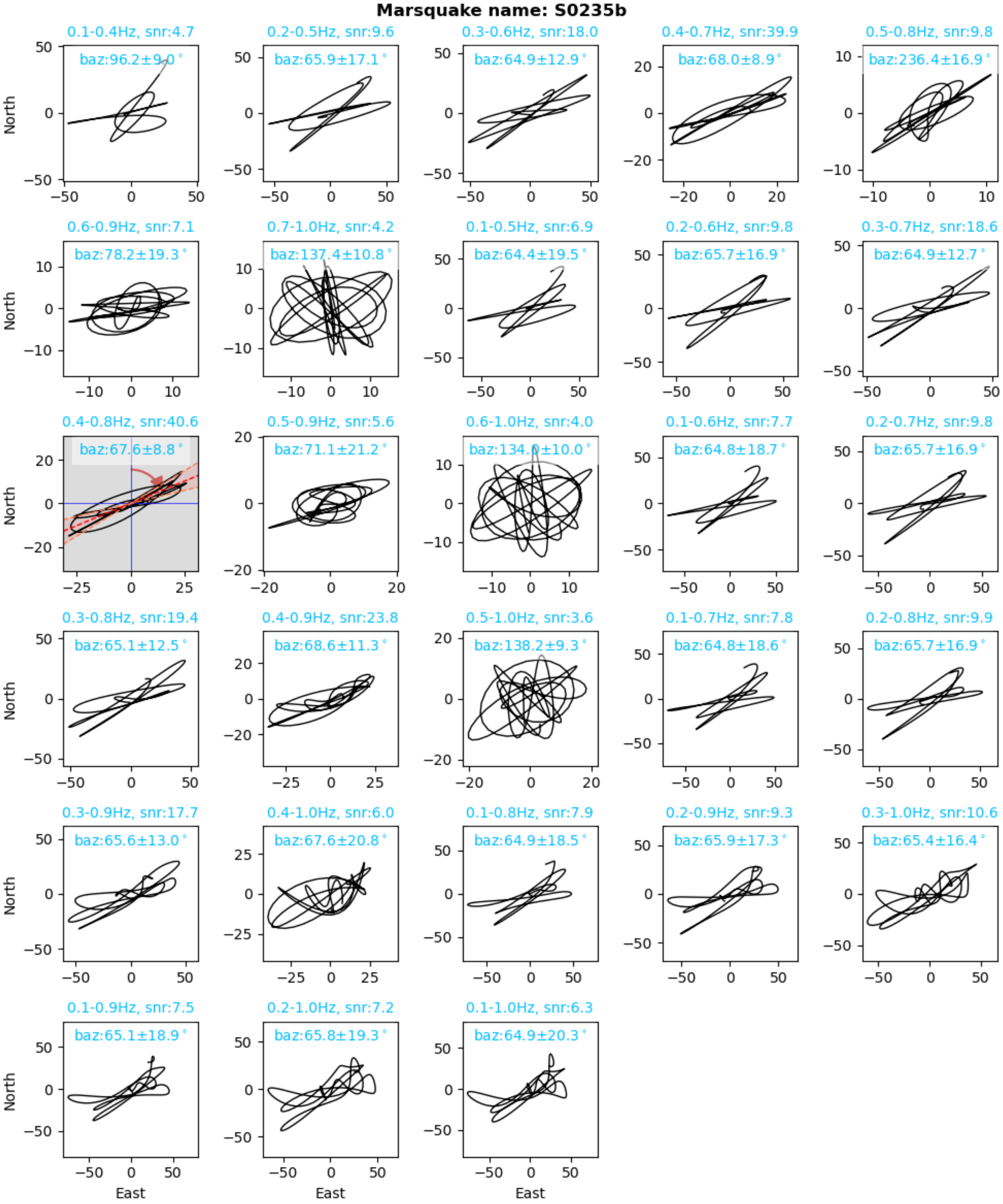

Fig. S31. Same as Fig. S26, but for S0235b.

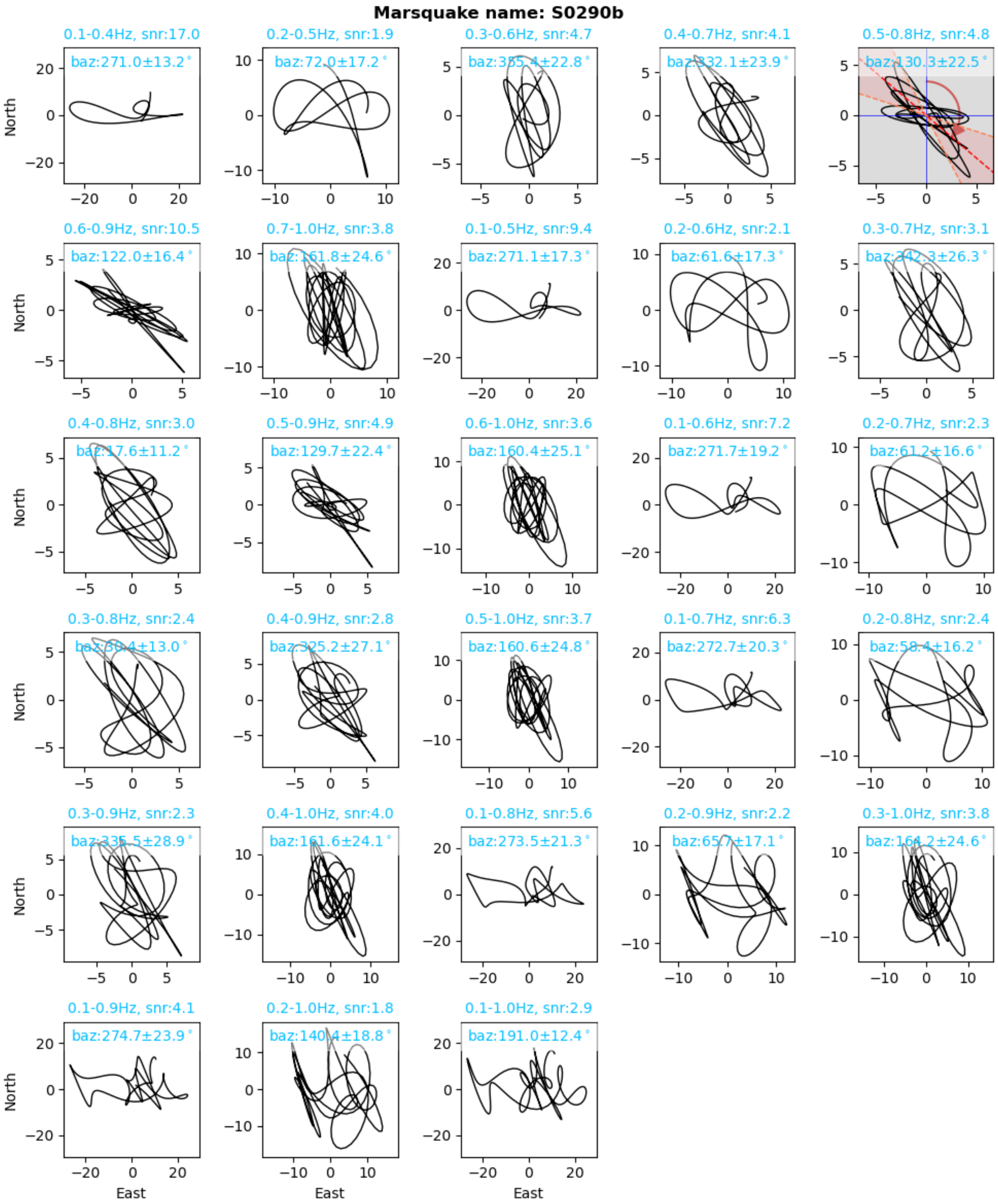

Fig. S32. Same as Fig. S26, but for S0290b.

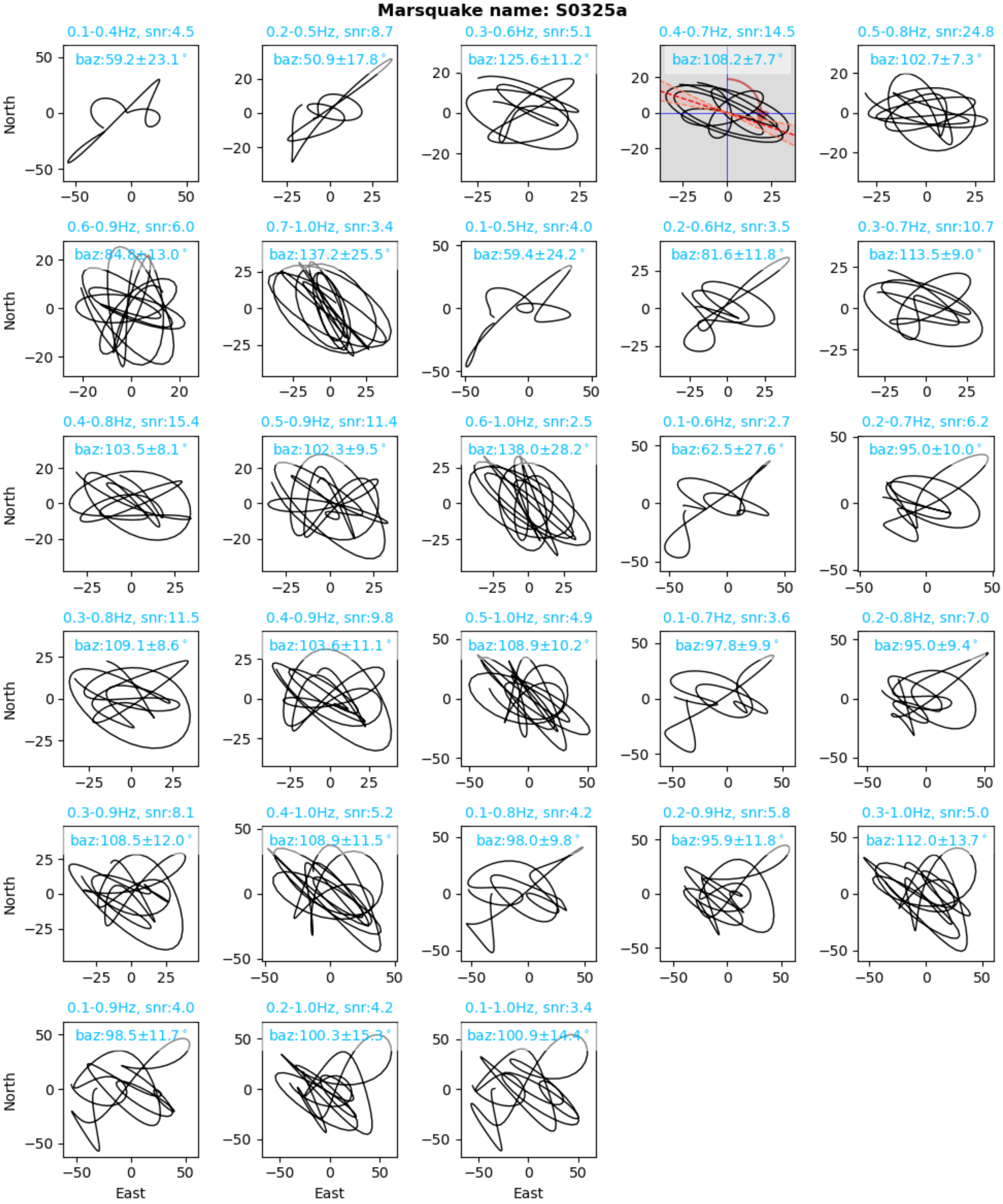

Fig. S33. Same as Fig. S26, but for S0325a.

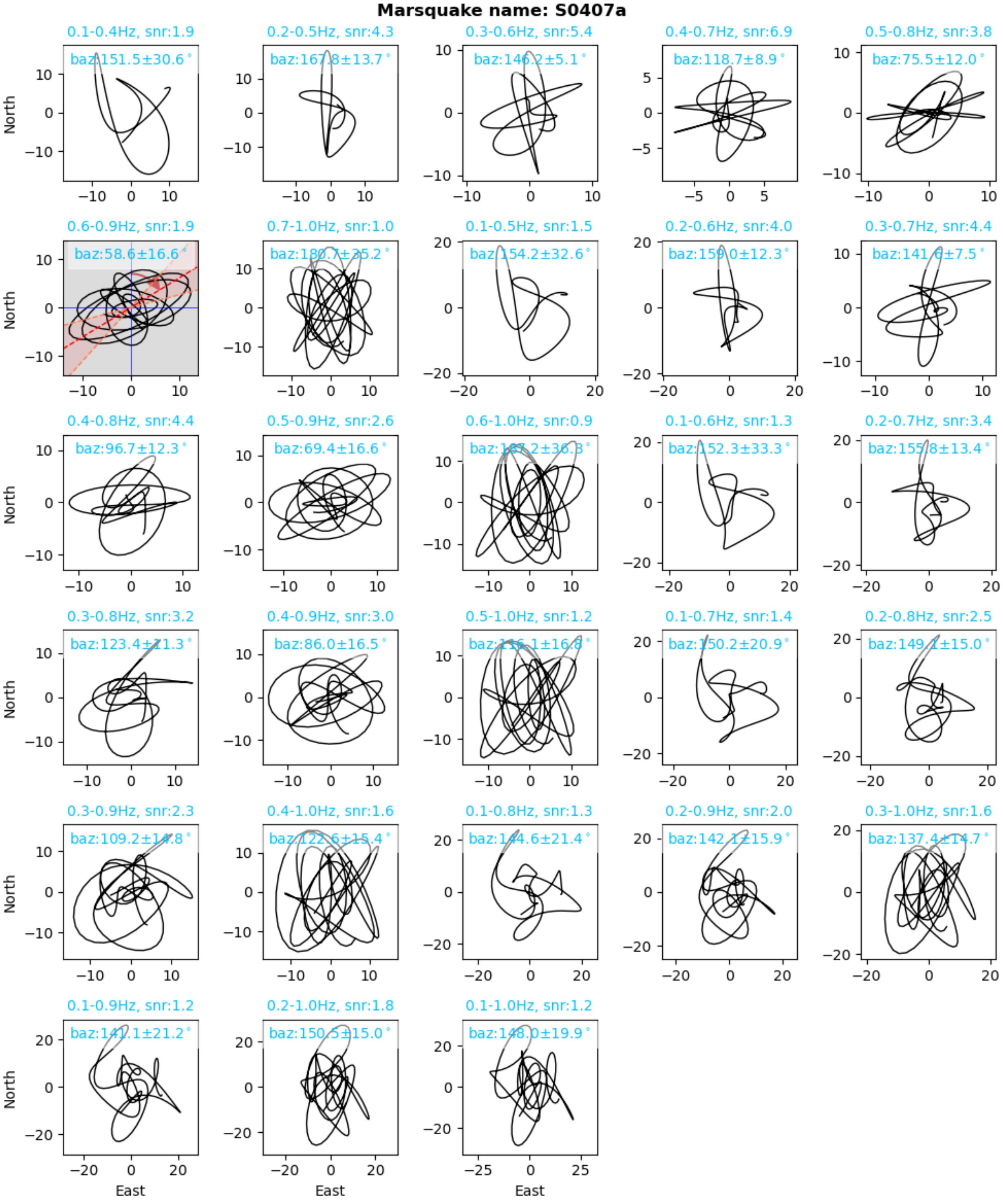

Fig. S34. Same as Fig. S26, but for S0407a.

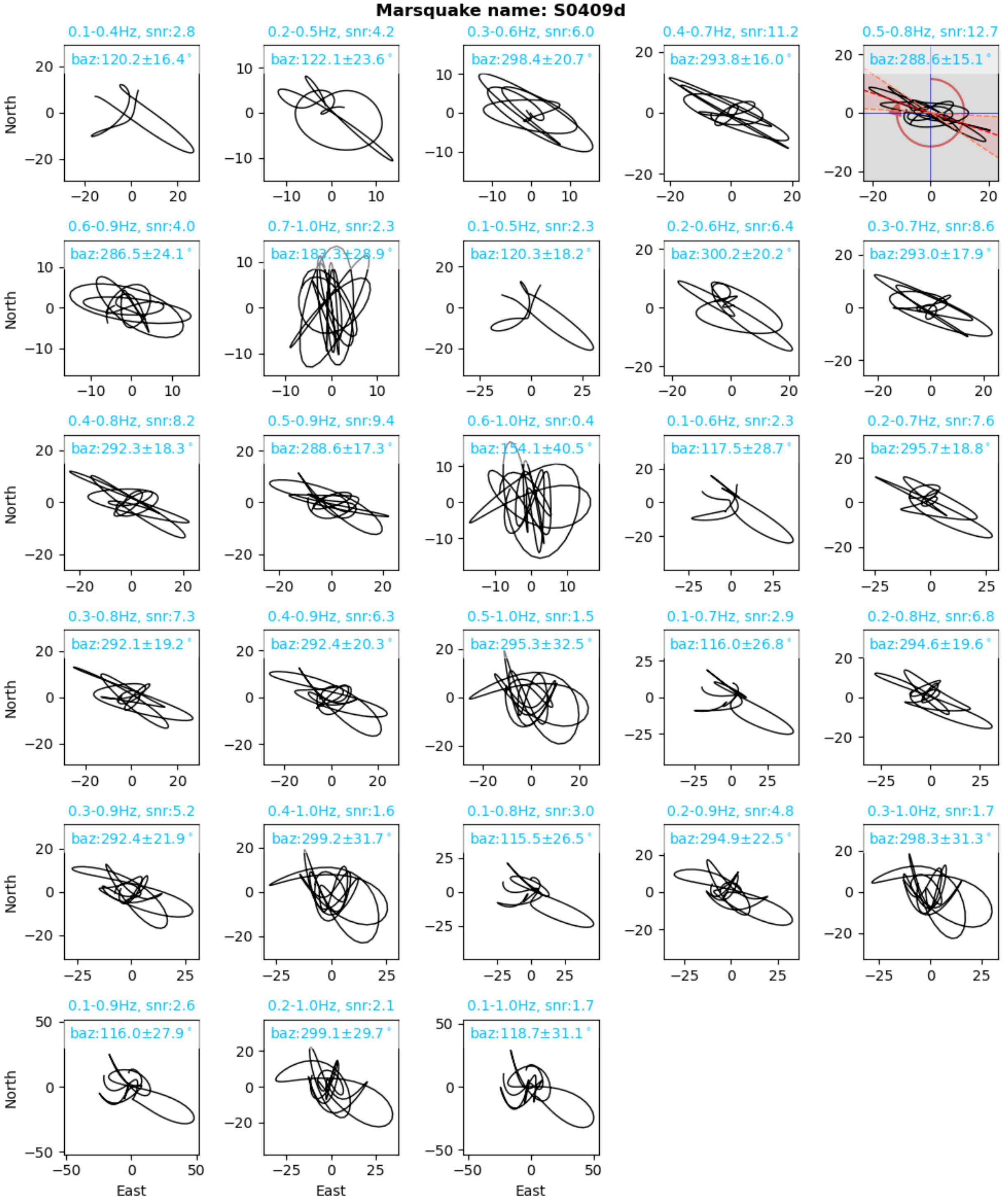

Fig. S35. Same as Fig. S26, but for S0409d.

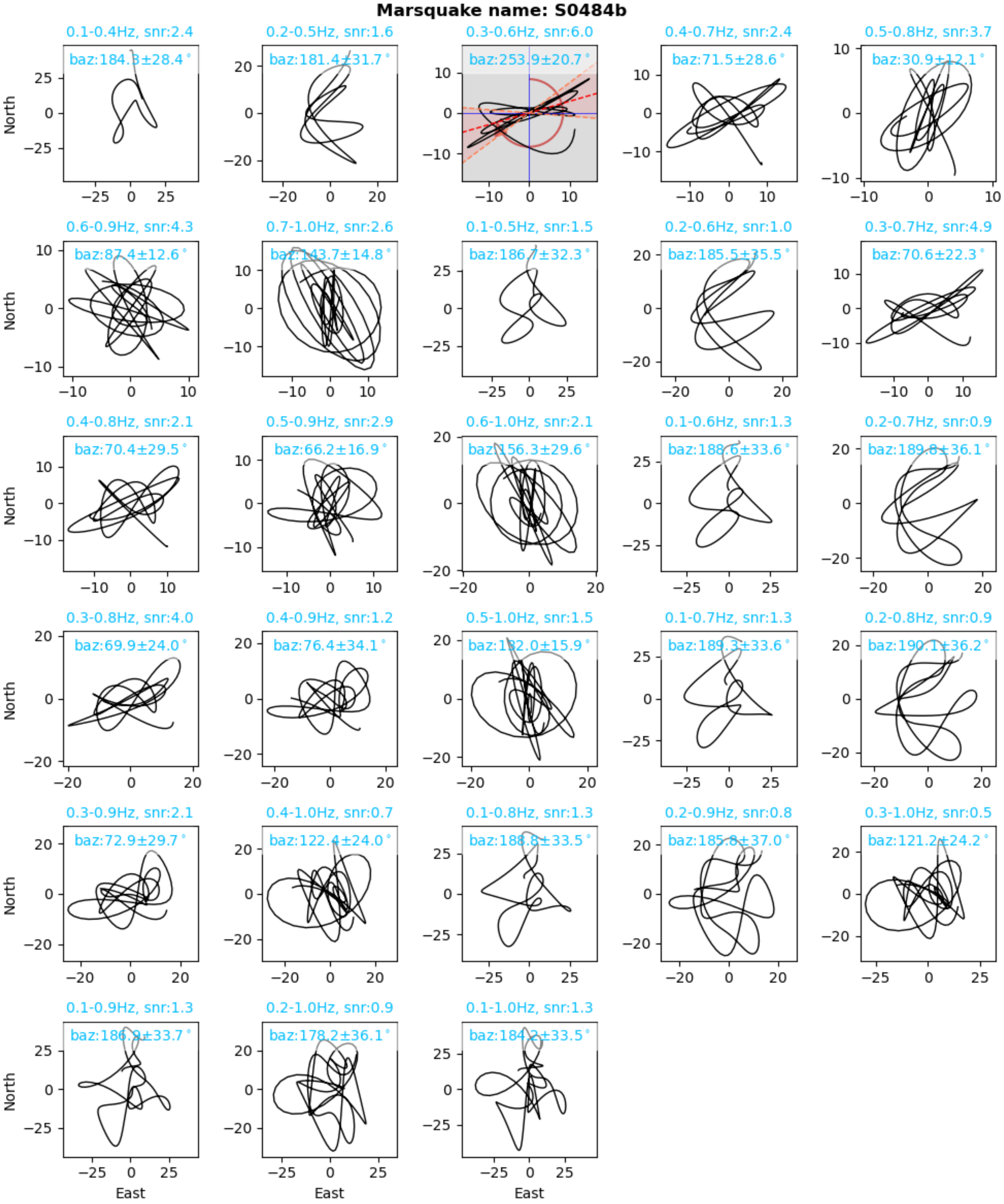

Fig. S36. Same as Fig. S26, but for S0484b.

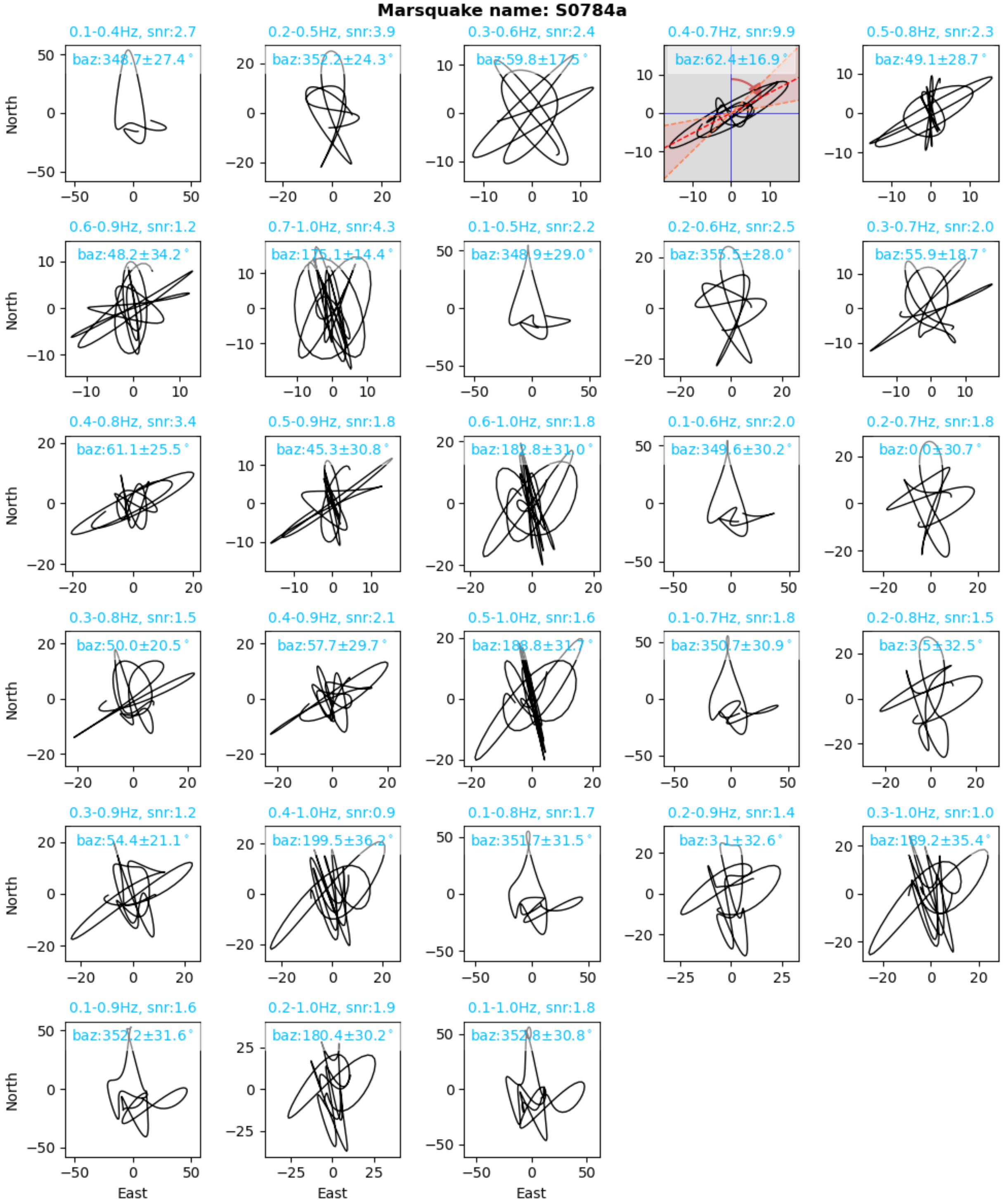

Fig. S37. Same as Fig. S26, but for S0784a.

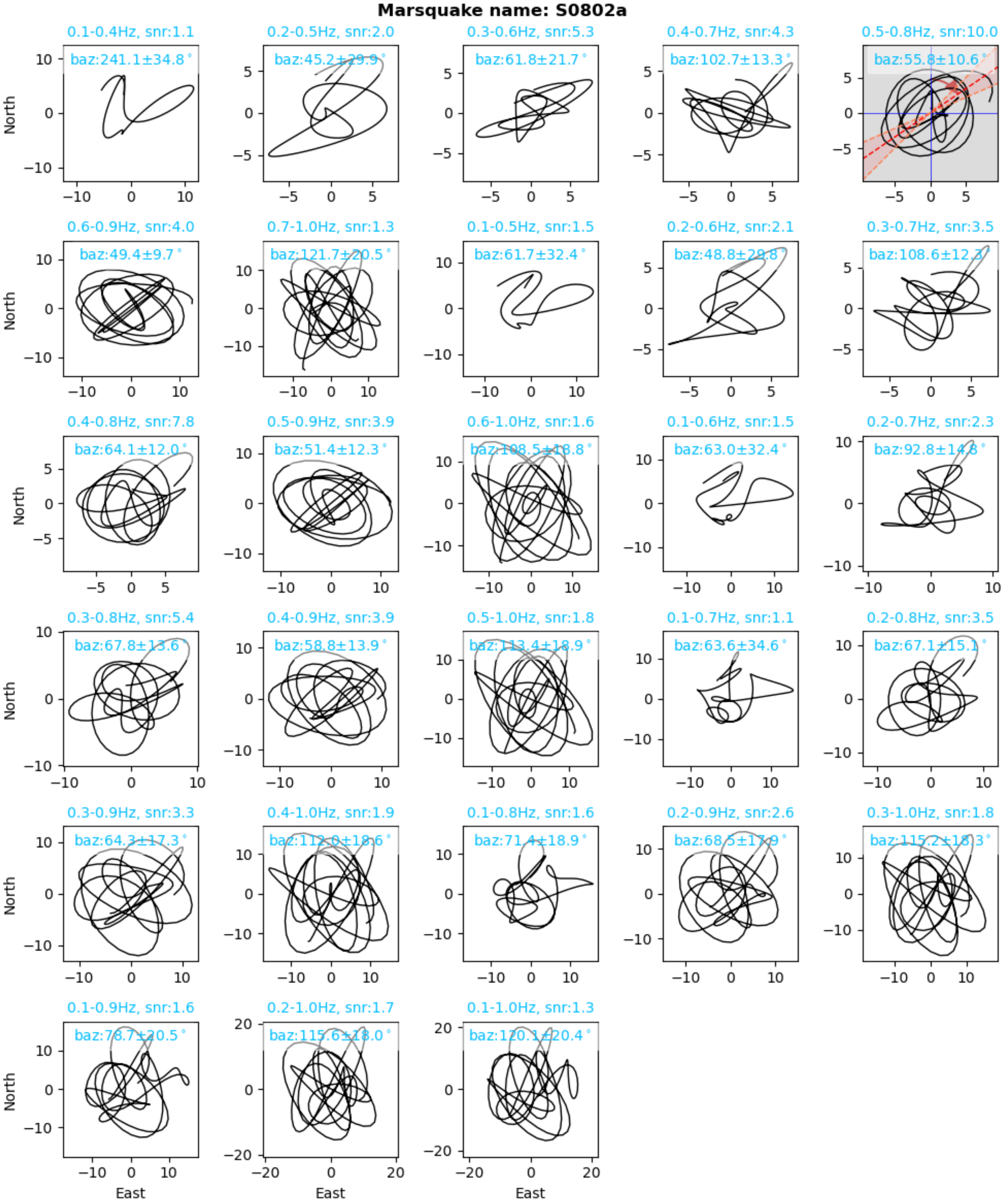

Fig. S38. Same as Fig. S26, but for S0802a.

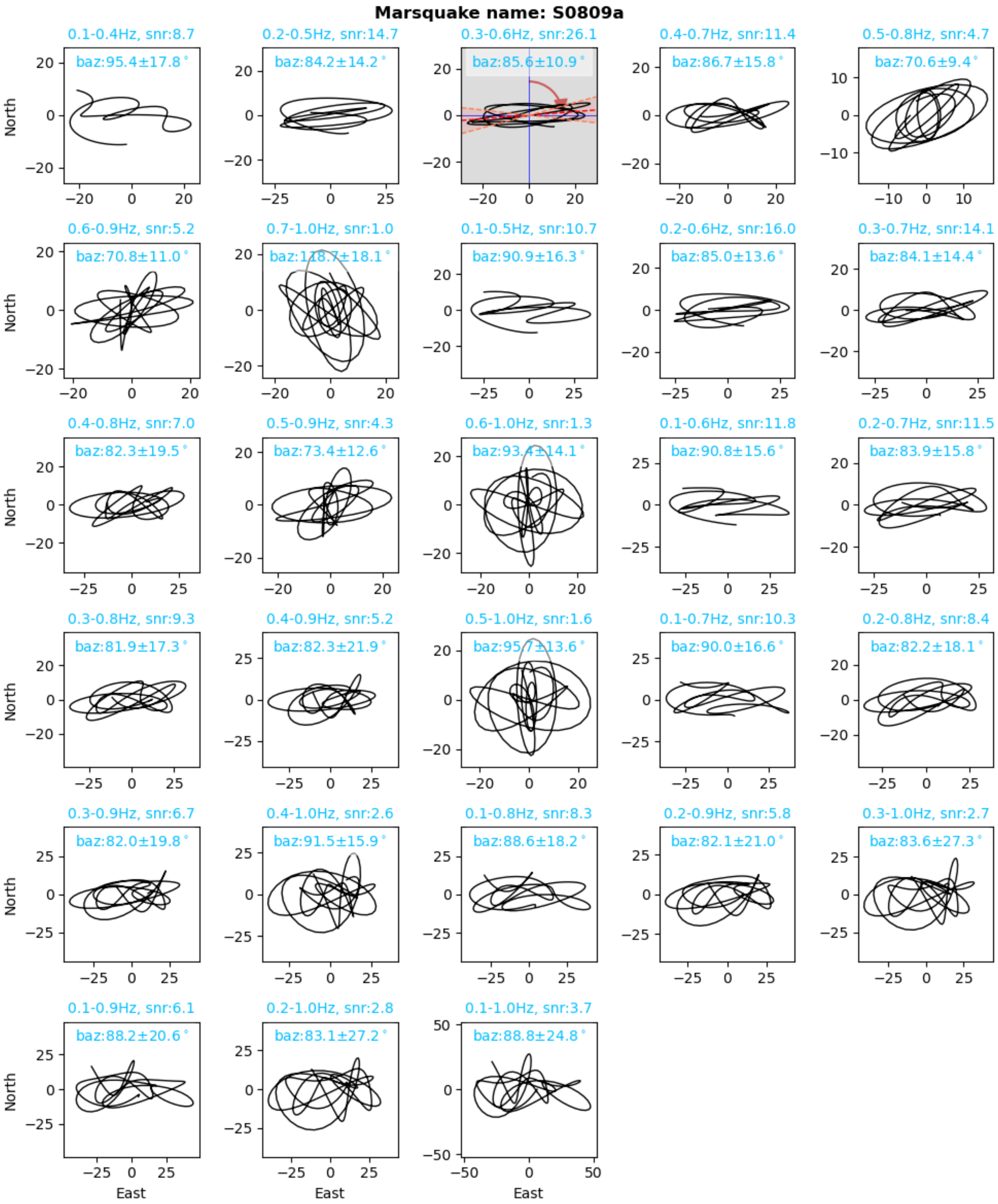

Fig. S39. Same as Fig. S26, but for S0809a.

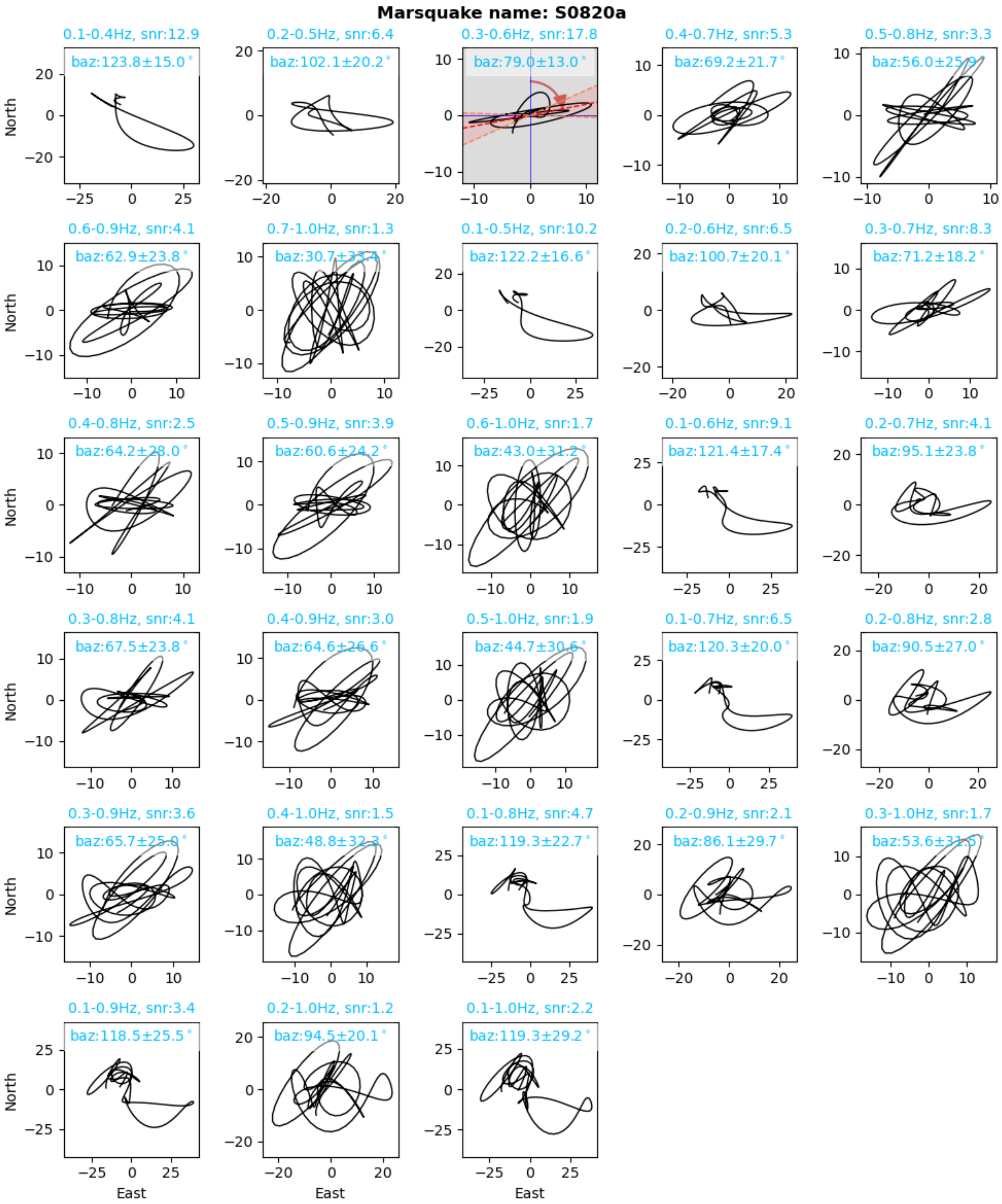

Fig. S40. Same as Fig. S26, but for S0820a.

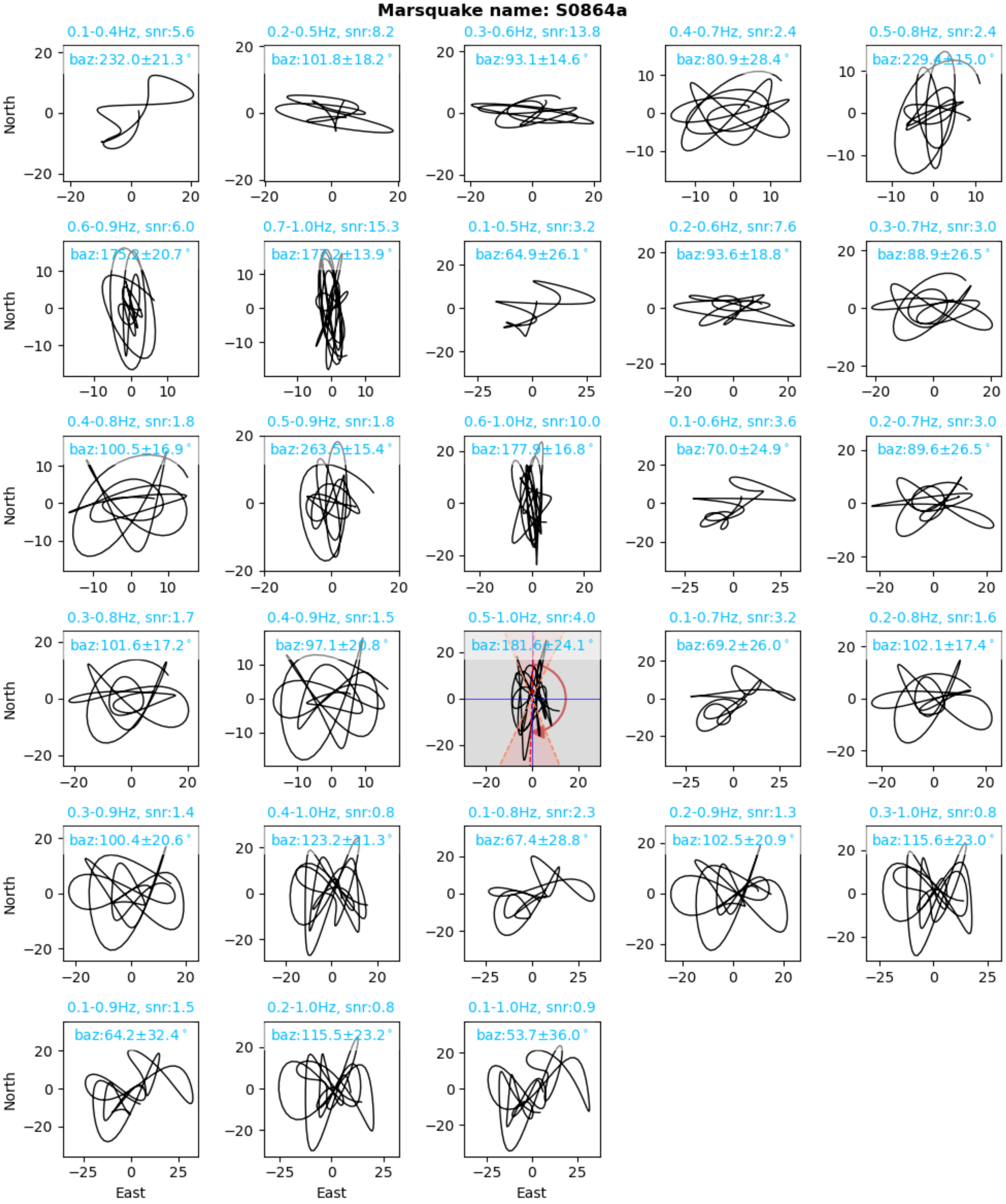

Fig. S41. Same as Fig. S26, but for S0864a.

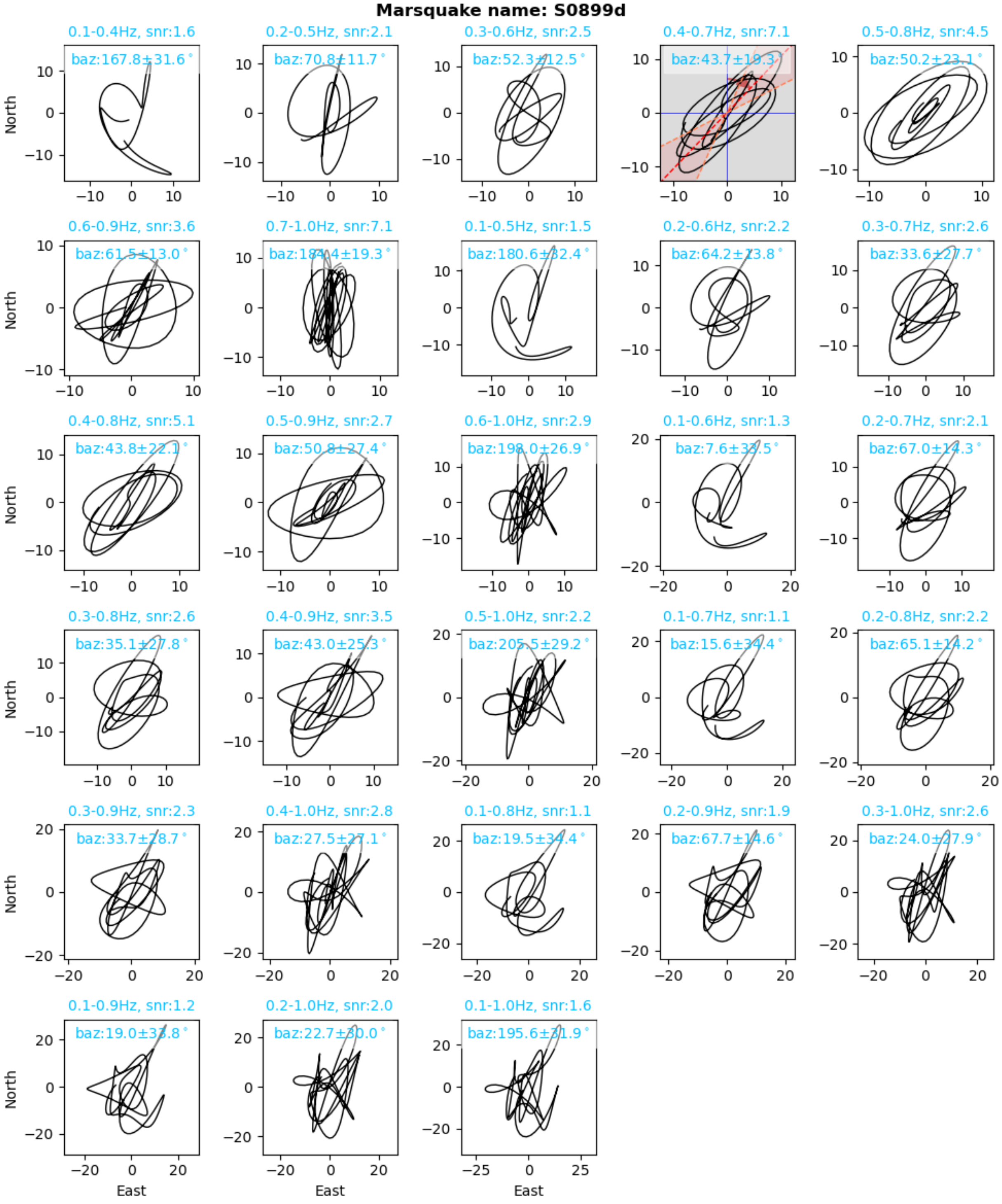

Fig. S42. Same as Fig. S26, but for S0899d.

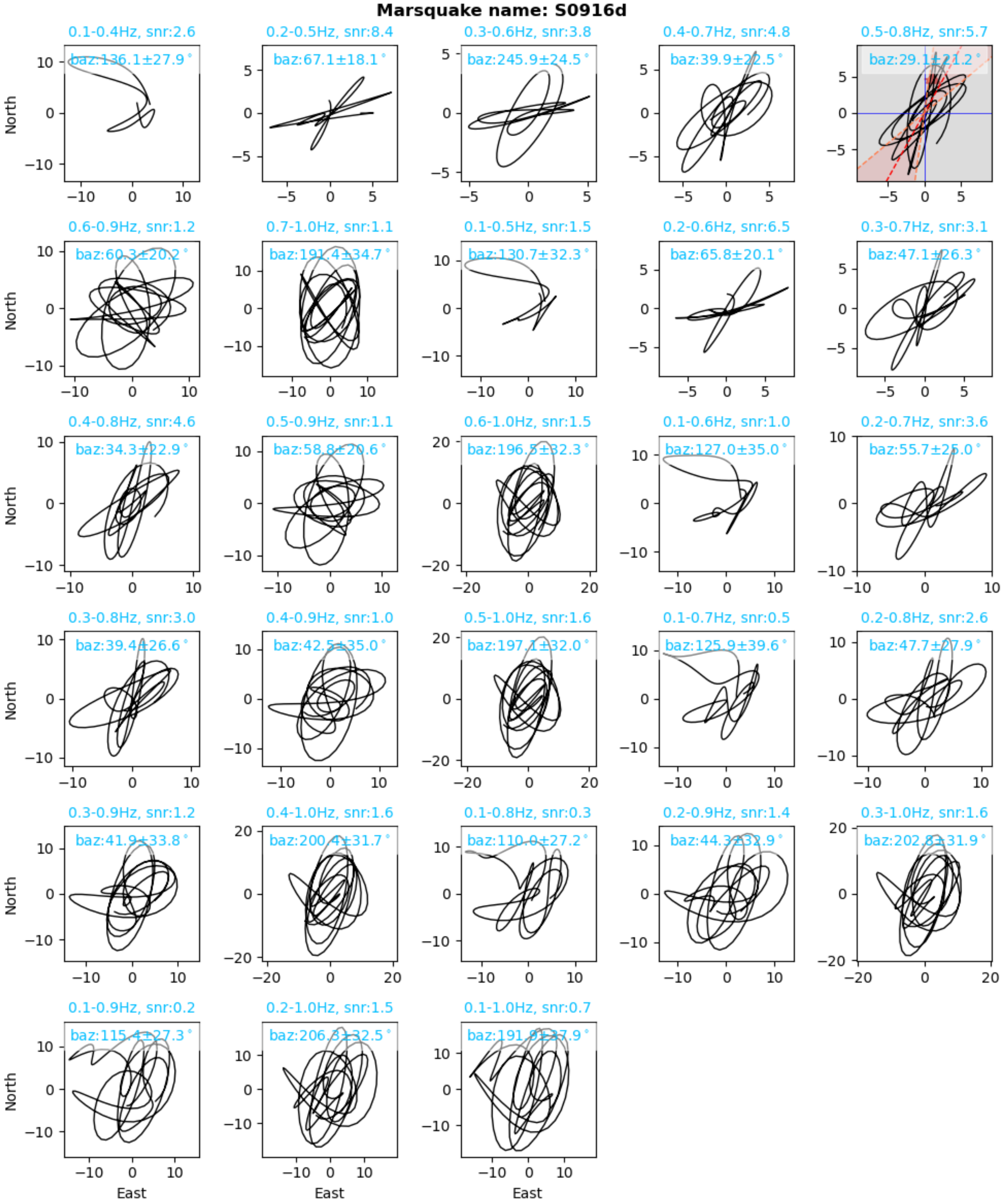

Fig. S43. Same as Fig. S26, but for S0916d.

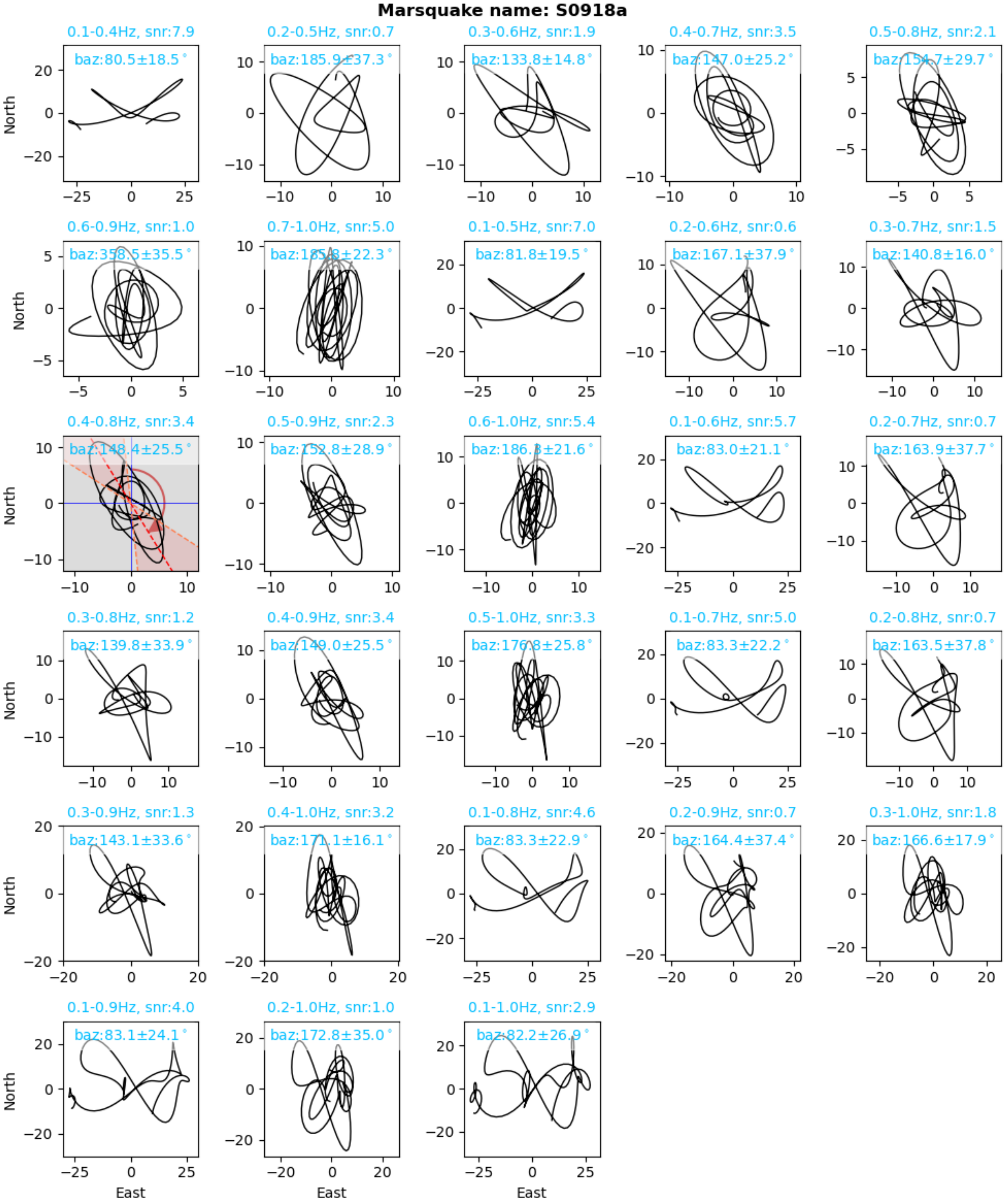

Fig. S44. Same as Fig. S26, but for S0918a.

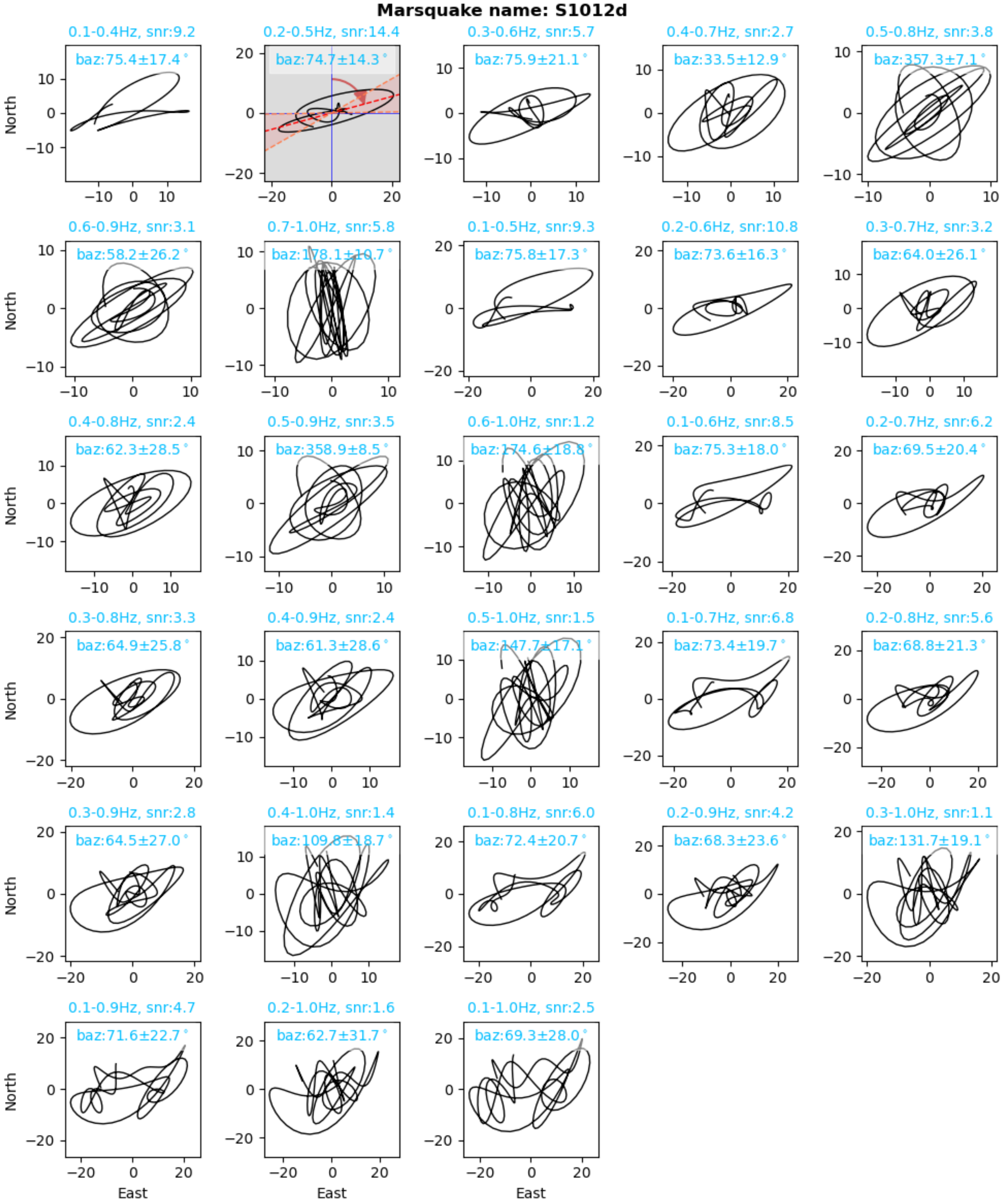

Fig. S45. Same as Fig. S26, but for S1012d.

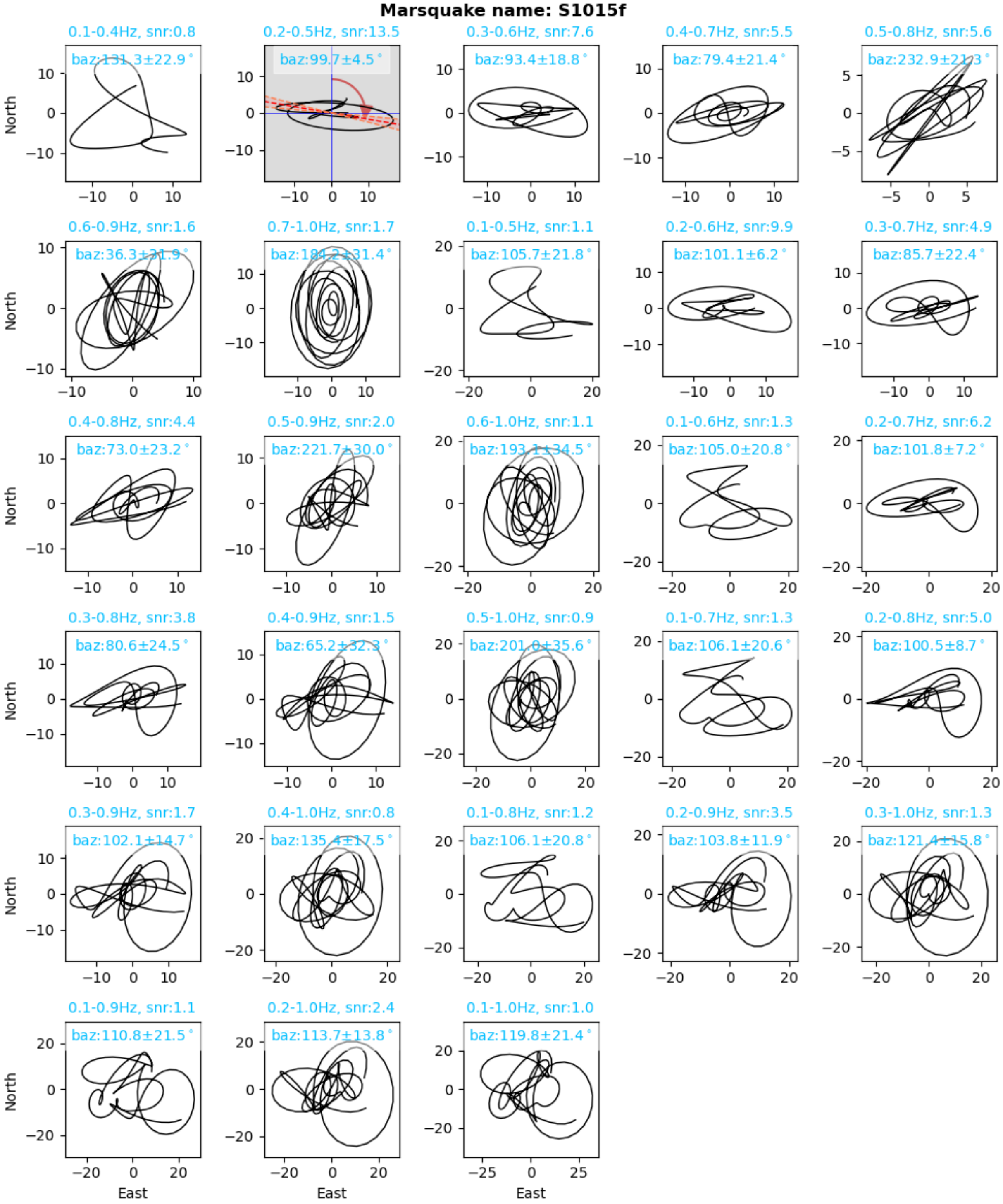

Fig. S46. Same as Fig. S26, but for S1015f.

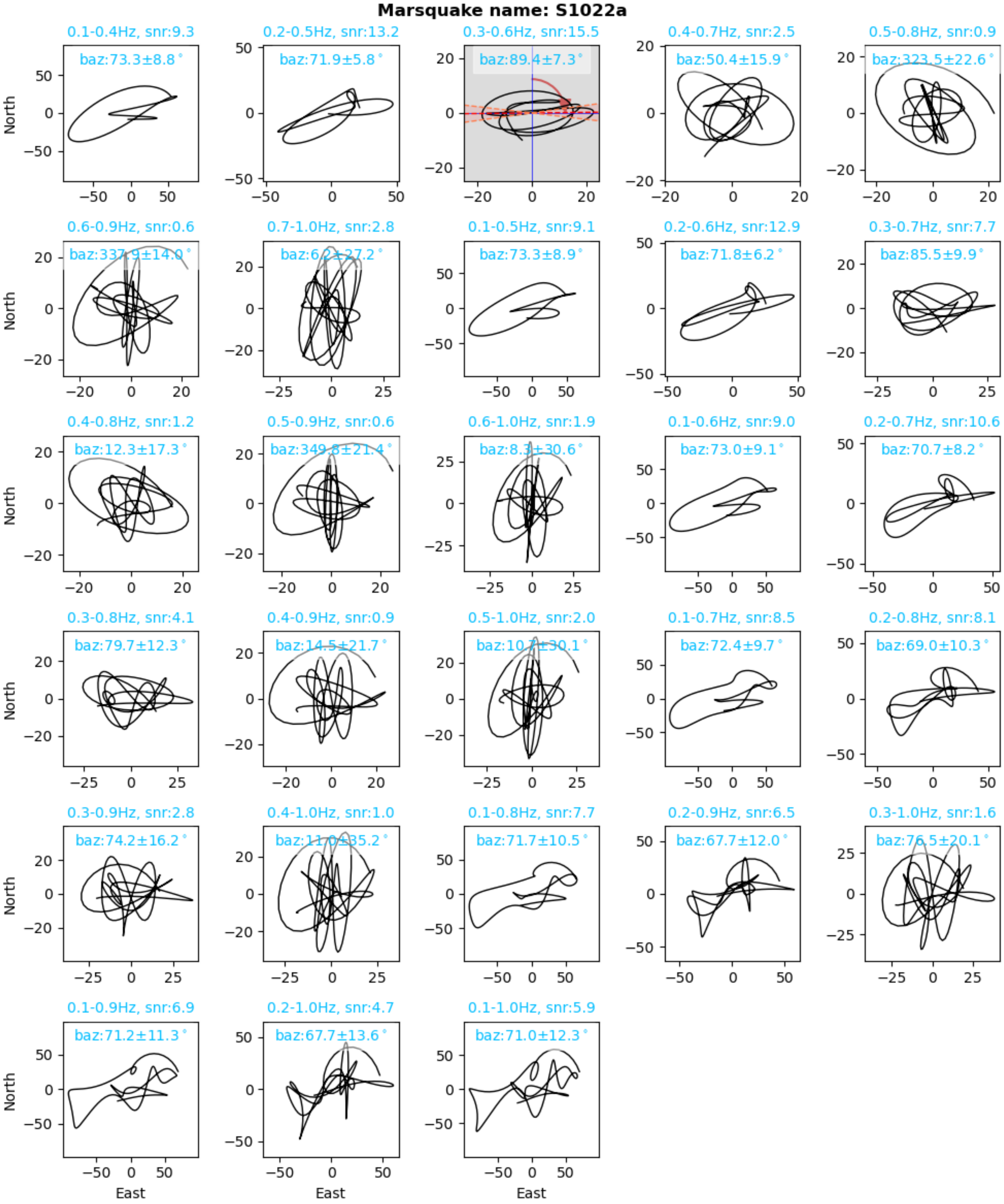

Fig. S47. Same as Fig. S26, but for S1022a.

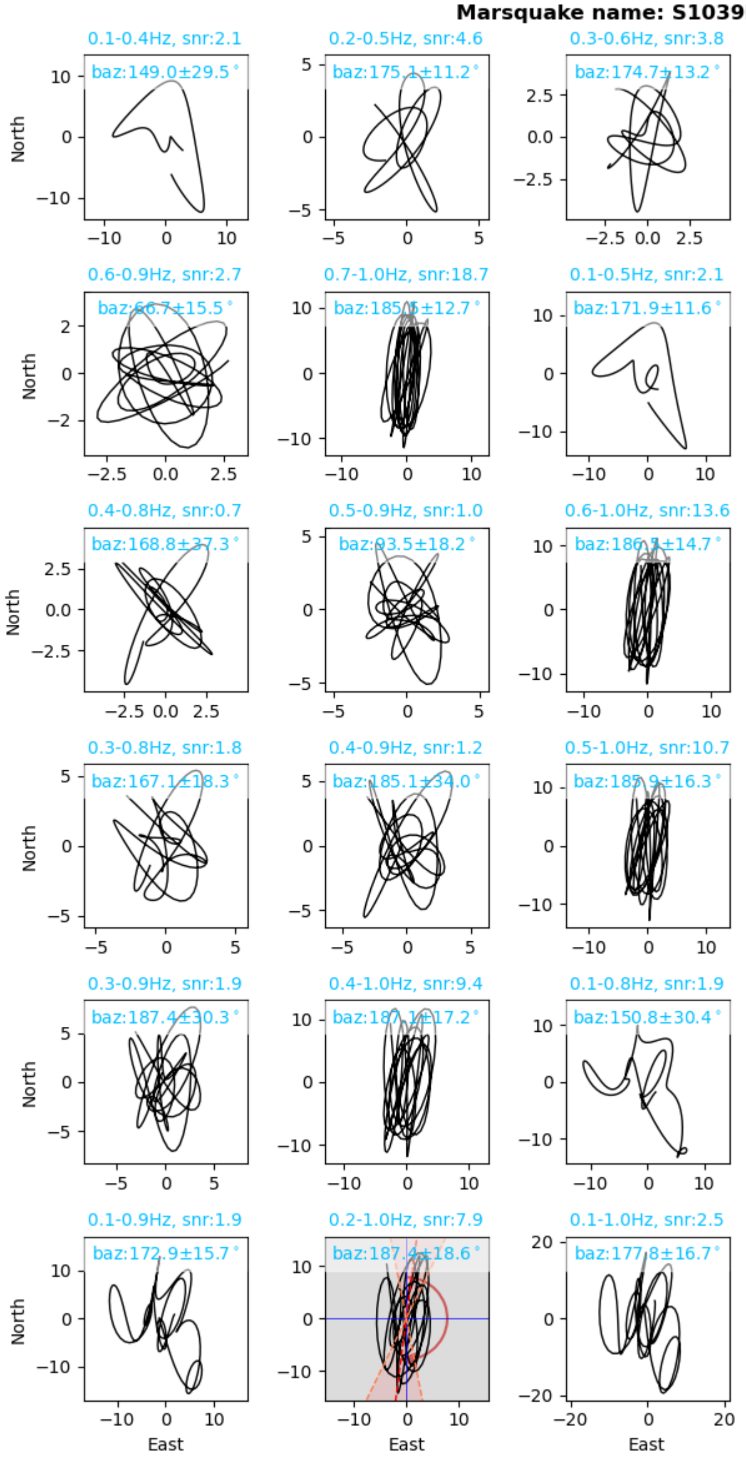

Fig. S48. Same as Fig. S26, but for S1039b.

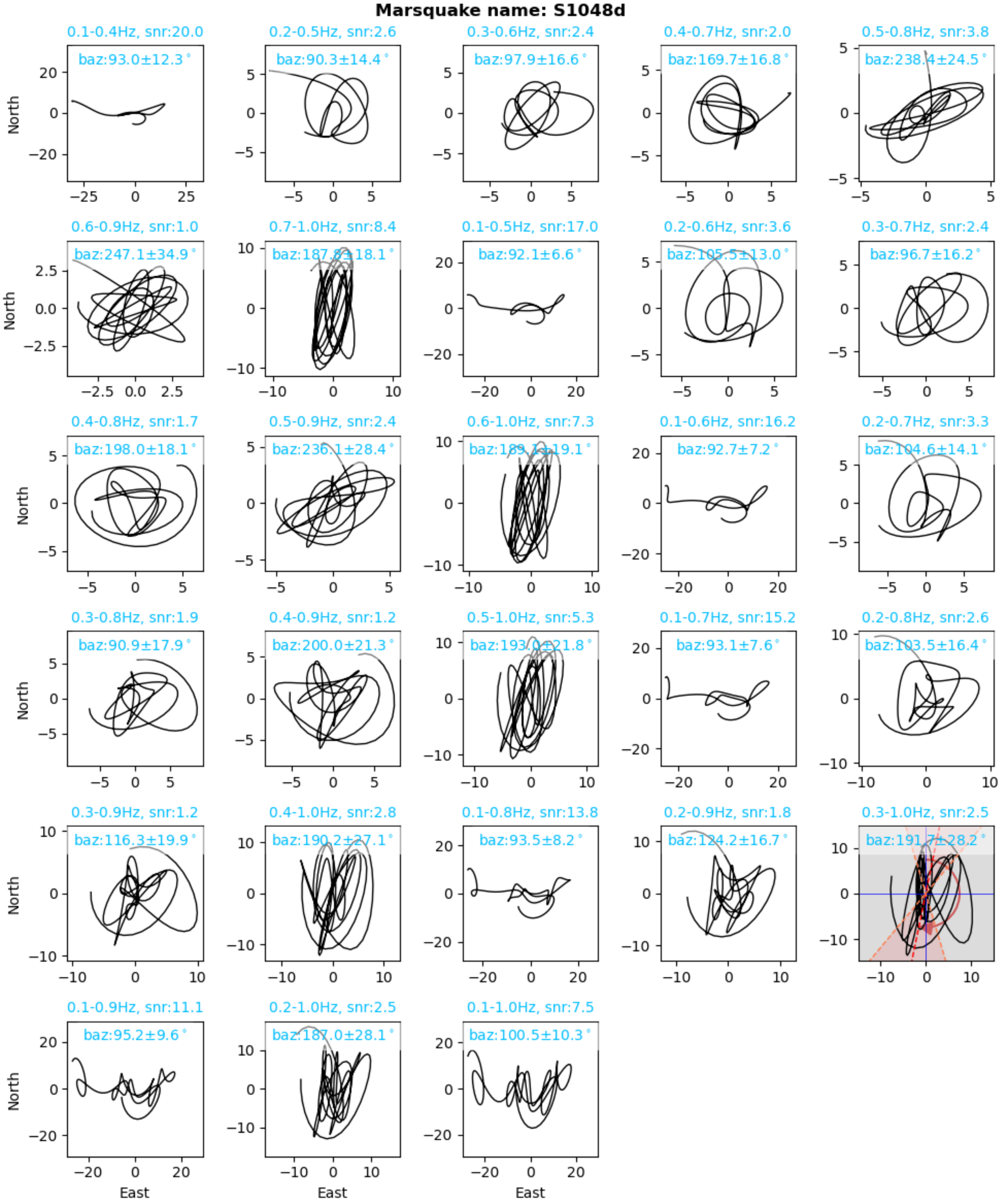

Fig. S49. Same as Fig. S26, but for S1048d.

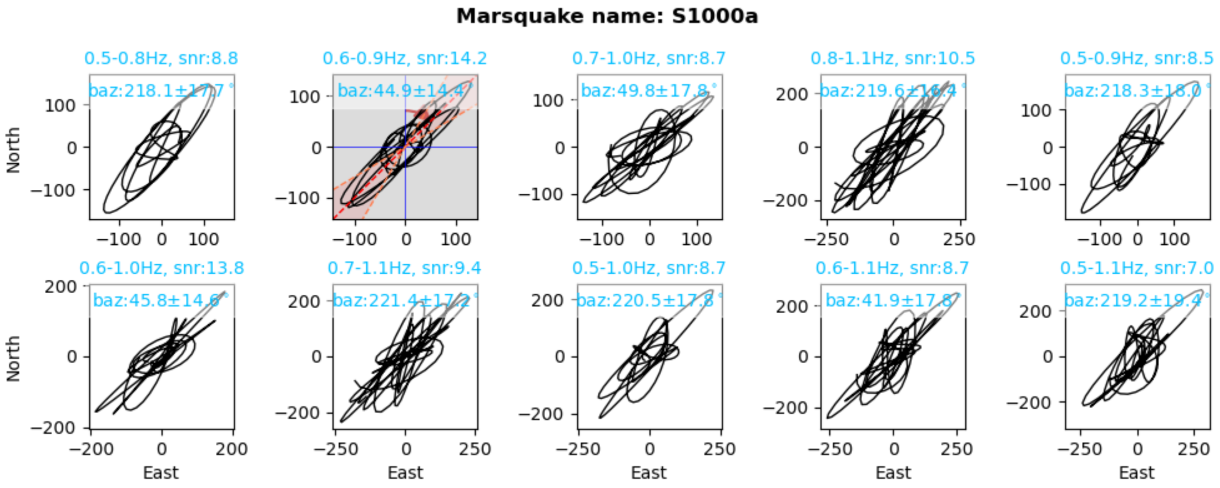

Fig. S50. Same as Fig. S26, but for S1000a. Since the meteorite impact event has much higher frequency components, the frequency bands are adjusted for the back-azimuth estimation.

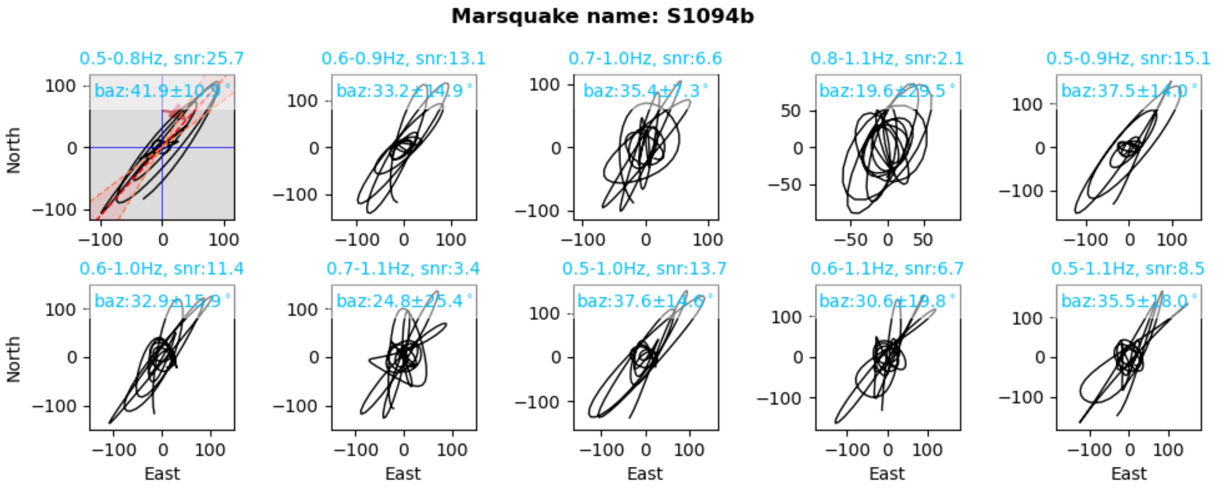

Fig. S51. Same as Fig. S50, but for S1094b.

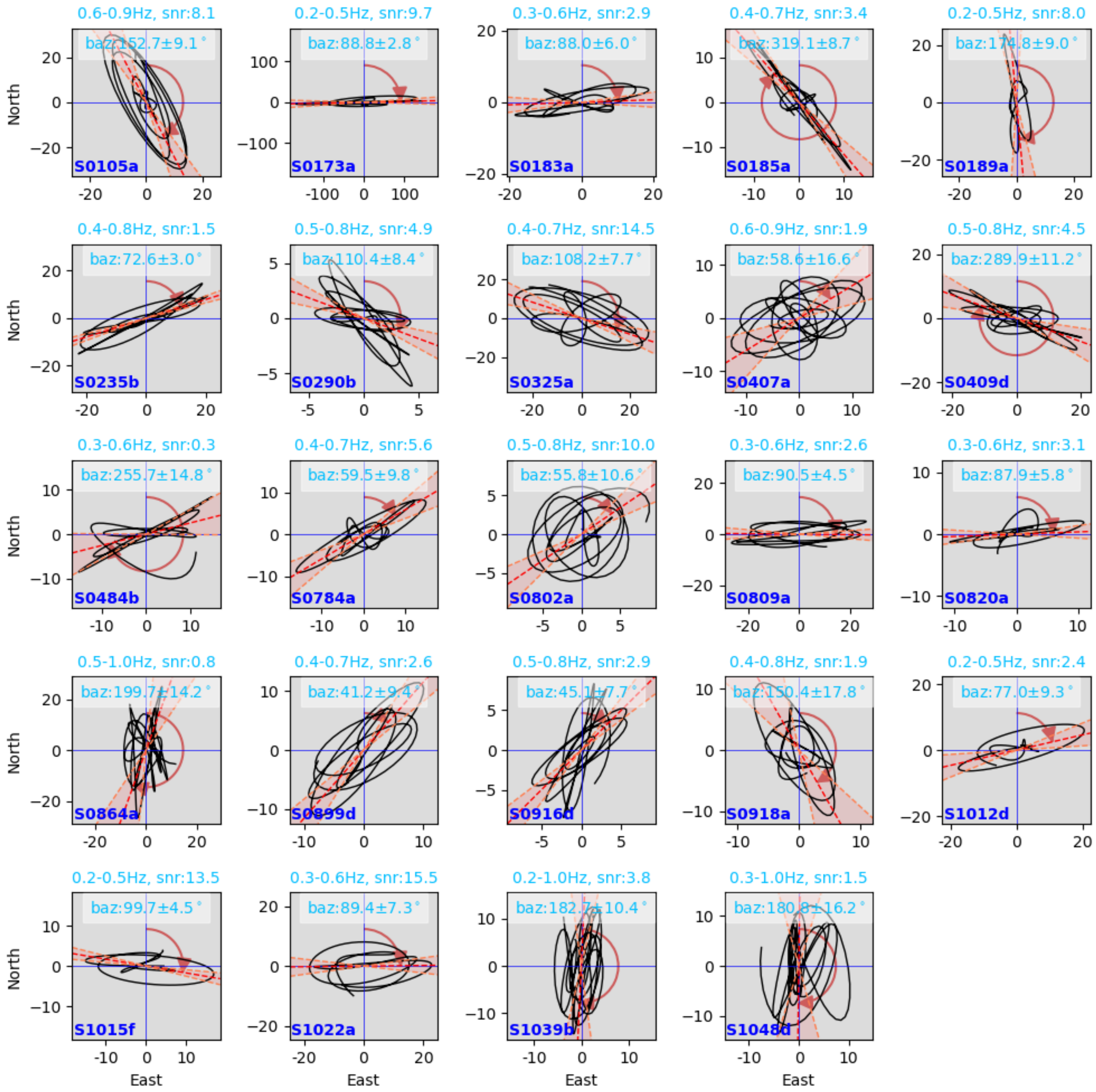

Fig. S52. Determination of the event back-azimuth from the 3-D analysis. Each hodogram illustrates particle motions of P waves in the 10-second-long window starting from the P-wave arrival. The frequency band and signal-to-noise ratio (SNR) are labeled. The measured back-azimuths, their uncertainties in degrees and marsquake IDs are also shown.

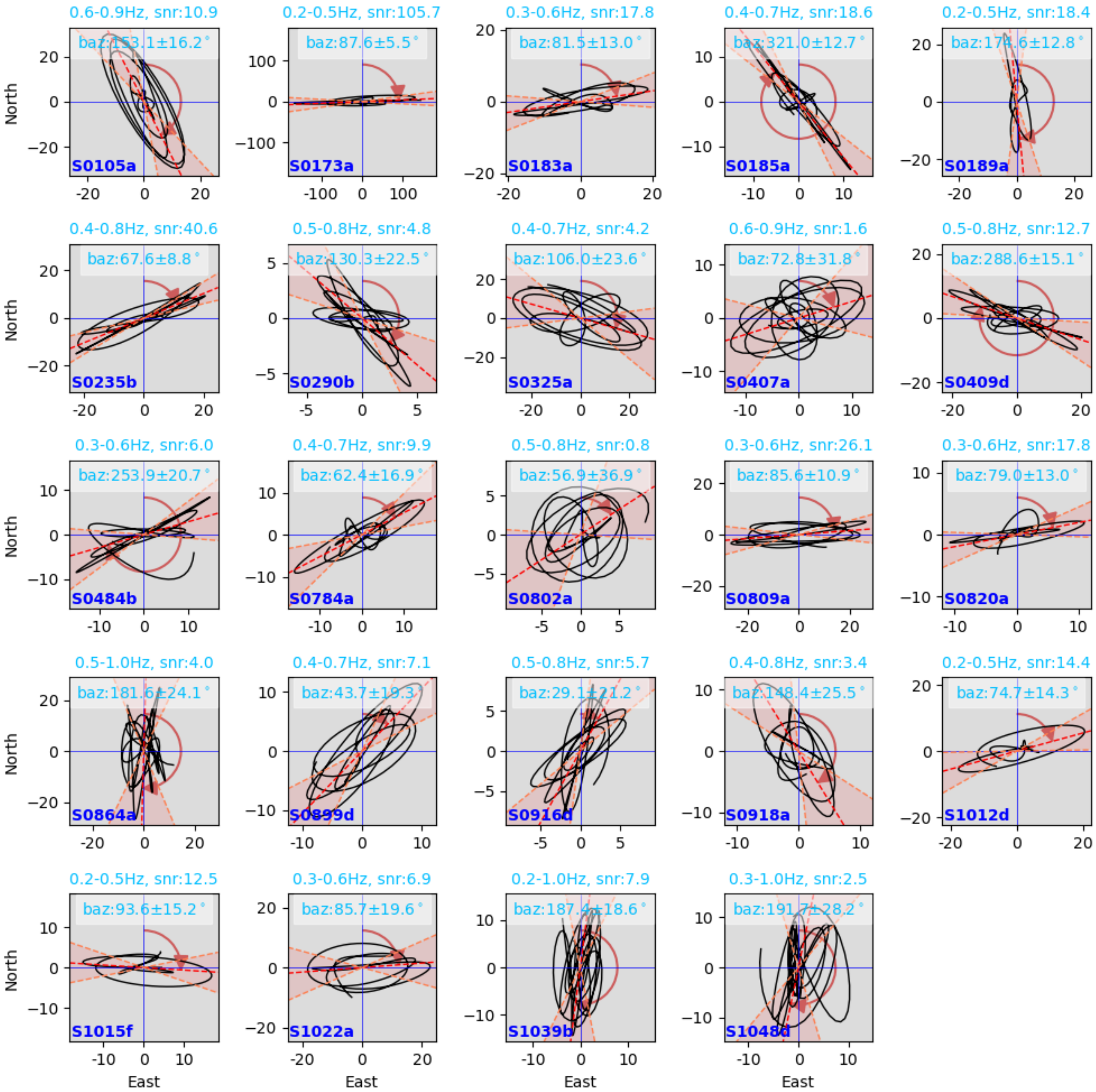

Fig. S53. Same as Fig. S52 but from the 2-D analysis.

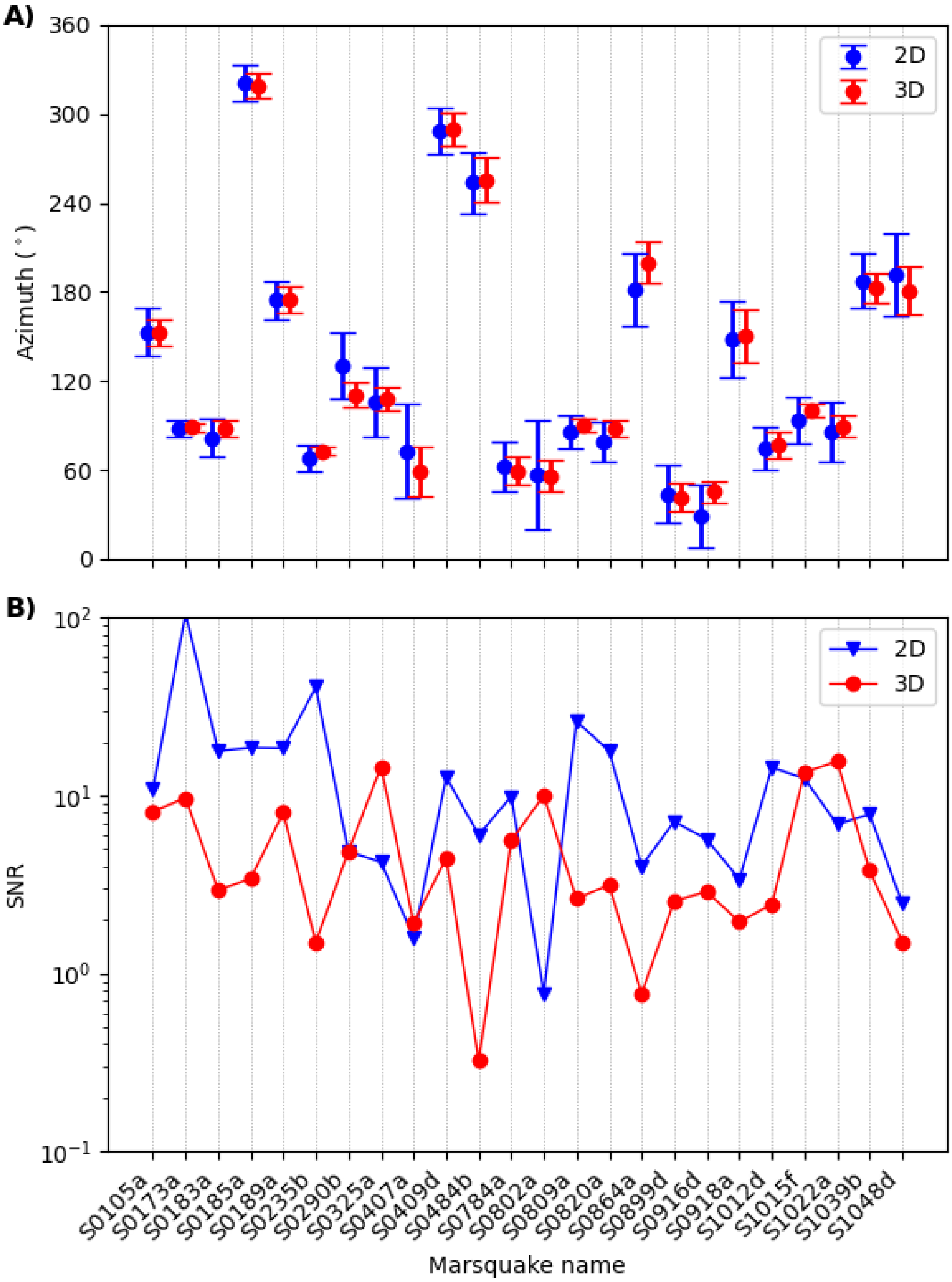

Fig. S54. The measurements of back-azimuth were determined by the 2-D and 3-D analyses for the successfully located marsquakes. A) The back azimuth and their uncertainties from 2-D (blue) and 3-D (red) analysis. B) The signal-to-noise ratio (SNR) is determined by the eigenvalue given by 2-D (blue) and 3-D (red) analysis.

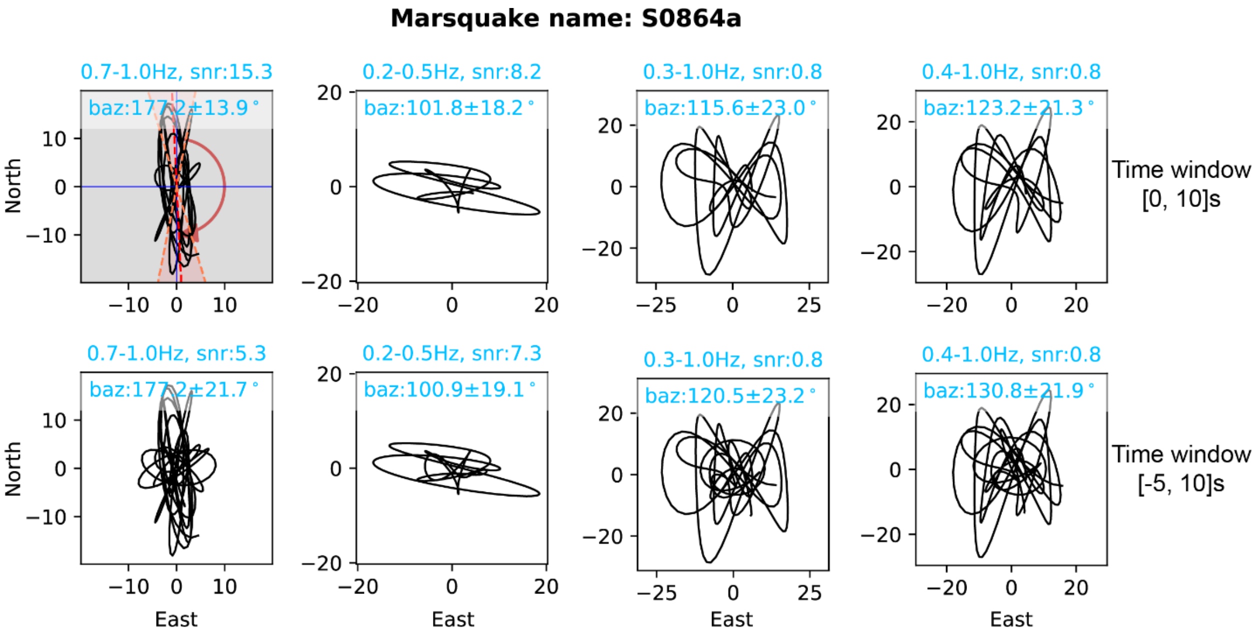

Fig. S55. The effect of the time duration selection for measuring back azimuth in various frequency bands. The top panel illustrates the estimated azimuth in the 10-s time window of [0, 10] s after the picked P arrival, i.e., no ambient noise preceding the P wave is included if the P-wave arrival is correctly picked. The lower panel shows the equivalent estimate using a 15-s time window of [-5, 10] s relative to the picked P-wave arrival, i.e., introducing a 5-s long ambient noise before the P-wave arrival, assuming it is picked correctly. This leads to the decrease of signal-to-noise ratio.

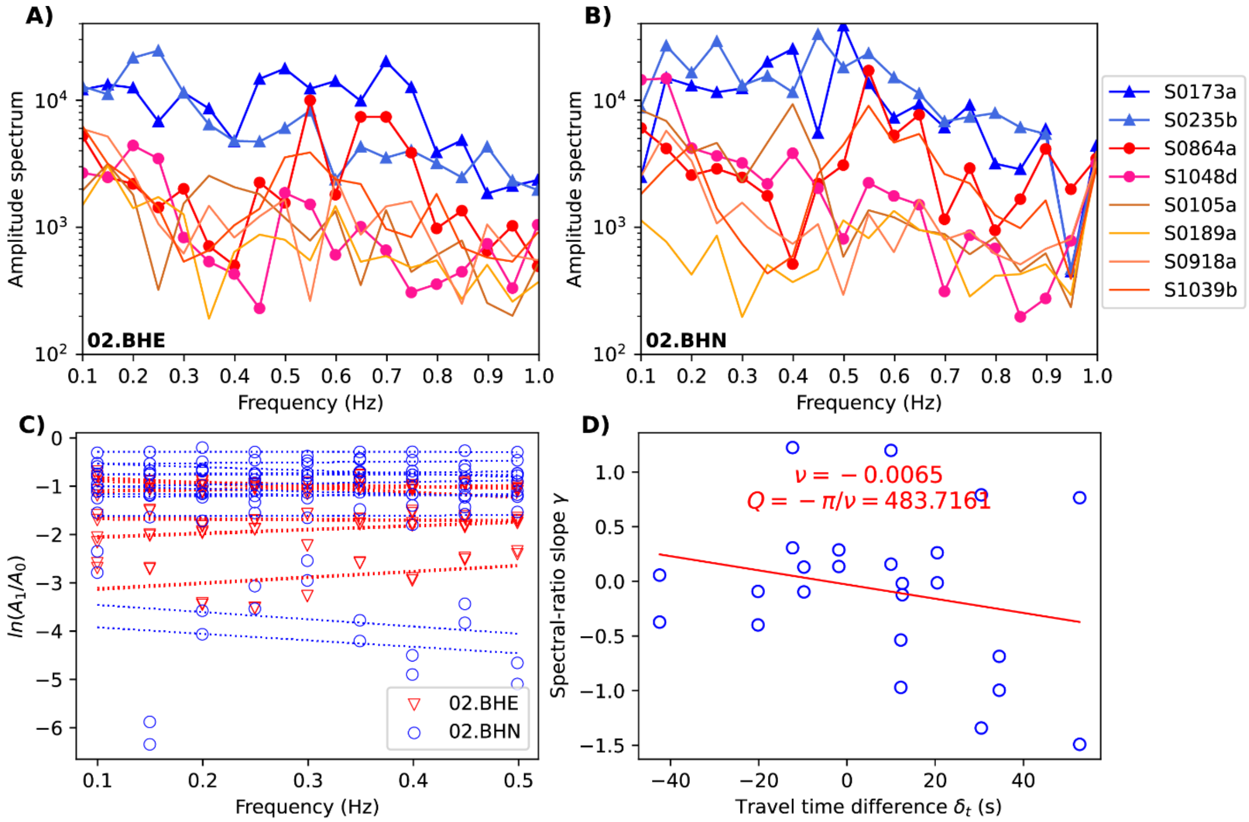

Fig. S56. Spectral analysis and attenuation measurement. (A) Amplitude spectrum of S-wave arrivals for 0.2BHE and (B) for 02.BHN. (C) Linear regression between spectral ratio and attenuation parameter. Dashed lines show the optimal fits. (D) Linear regression between spectral-ratio slope and travel time difference. The fitted lines are in red.

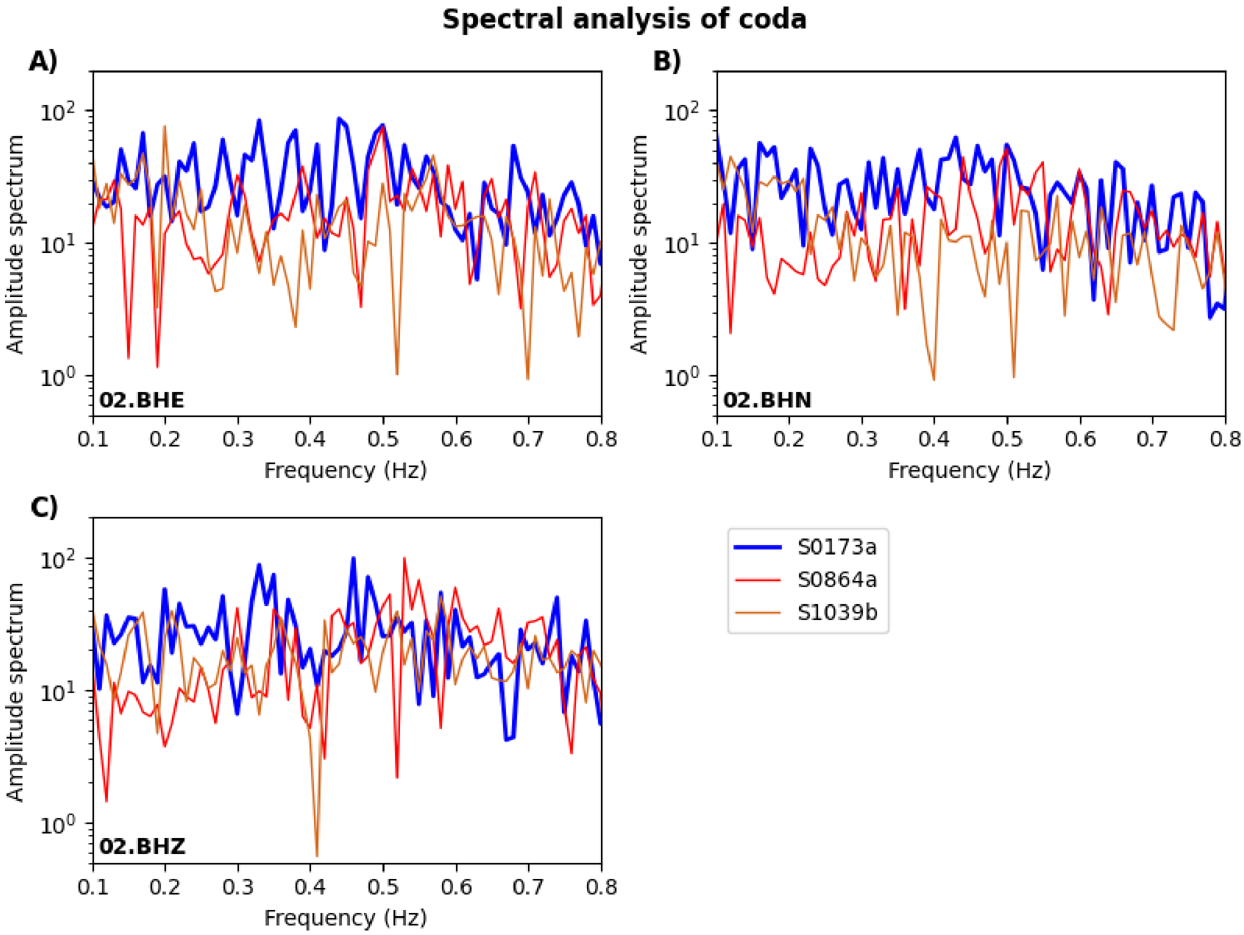

Fig. S57. Spectral analysis of coda wave. Amplitude spectrum of coda waves for components of (A) 0.2BHE, (B) 02.BHN, and (C) 02.BHZ of three selected marsquakes (S0173a in Elysium Planitia, S0864a, and S1039b in Terra Cimmeria) with similar epicentral distances.

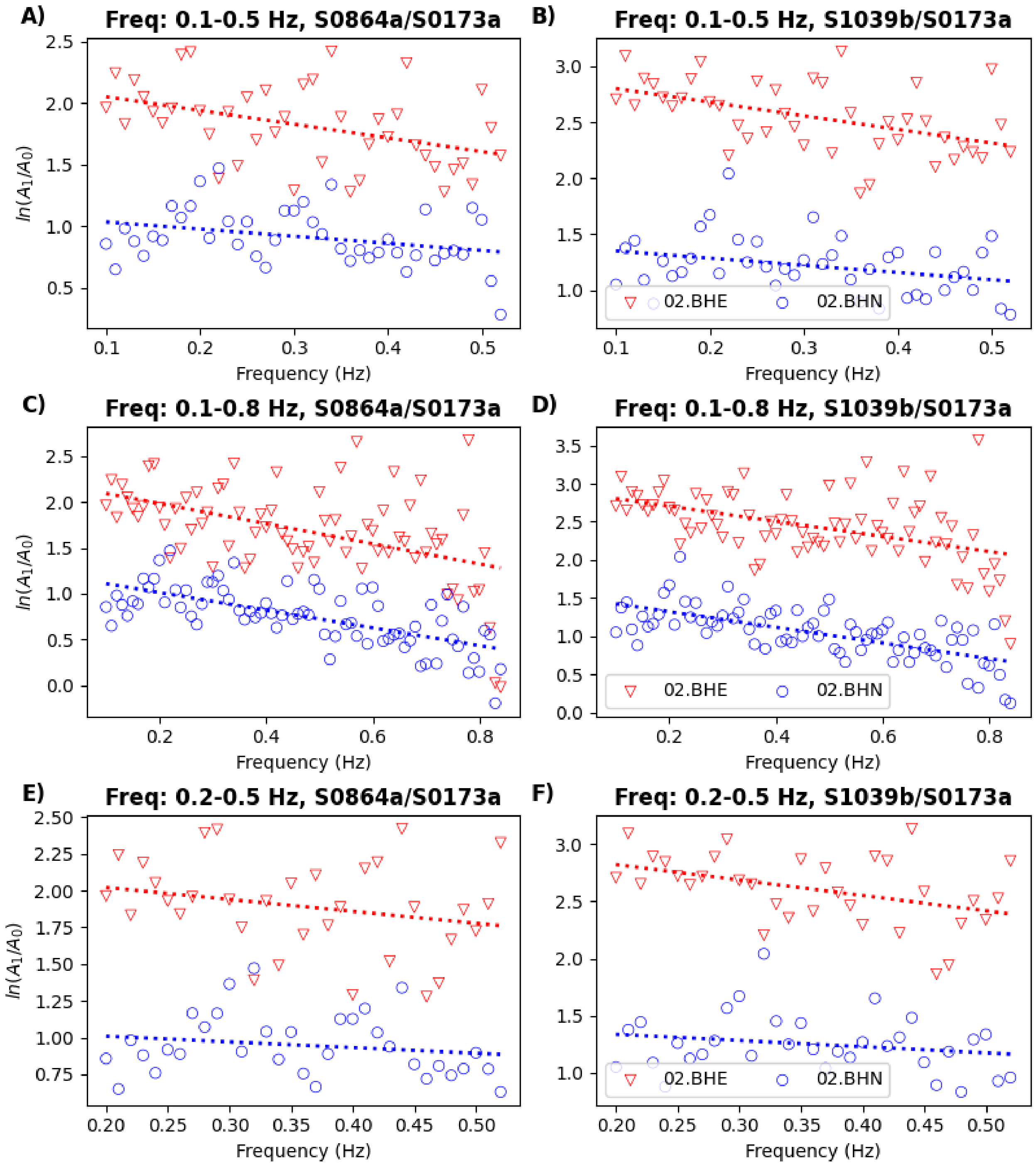

Fig. S58. The measurements of quality factor from coda wave. The Q_c value from the coda waves is calculated in various frequency bands: 0.1-0.5 Hz (A, B), 0.1-0.8 Hz (C, D), and 0.2-0.5 Hz (E, F) for three selected marsquakes, i.e., S0864a (A, C, E) and S1039b (B, D, F) in Terra Cimmeria over S0173a in Elysium Planitia.

Table S1. P-wave and S-wave picks for events analyzed in this study.

Event name	Event quality	Event type	MQS				This study								
			P picks	P U r	S-P	S U r	P picks	P U r	P channel	P method	S-P	S U r	S U r	S method
S0105a	B	LF	2019-03-14T21:03:31.110886Z	±20	188.30	±20	2019-03-14T21:03:38.128079Z	±0	02.BHW	['DAPF']	181.89	±0.54	02.BHW	['DAPF', 'BP', 'CCH']
S0173a	A	LF	2019-05-23T02:22:59.069095Z	±1	174.70	±2	2019-05-23T02:22:56.023762Z	±0.04	02.BHW	['BP', 'DAPF']	176.44	±0.01	02.BHN	['BP', 'DAPF']
S0183a	B	LF	2019-06-03T02:27:49.049133Z	±1	266.65	±60	2019-06-03T02:27:46.928588Z	±0.03	02.BHW	['BP', 'CCH']	259.96	±0.43	02.BHN	['BP', 'DAPF', 'CCH']
S0185a	B	BB	2019-06-05T02:13:50.450822Z	±60	344.42	±20	2019-06-05T02:14:04.981111Z	±0	02.BHU	['DAPF']	325.82	±0.09	02.BHW	['CCH', 'BP']
S0189a	B	LF	2019-06-09T05:40:05.564239Z	±20	193.91	±20	2019-06-09T05:40:31.274046Z	±0.55	02.BHU	['DAPF', 'CCH']	190.02	±0.05	02.BHV	['CCH', 'BP']
S0235b	A	BB	2019-07-26T12:19:18.032523Z	±1	167.29	±2	2019-07-26T12:19:17.204752Z	±0.13	02.BHW	['BP', 'CCH']	166.51	±0.68	02.BHN	['CCF', 'BP', 'DAPF', 'CCH']
S0290b	B	LF	2019-09-21T03:19:09.490618Z	±20	175.42	±20	2019-09-21T03:19:28.224647Z	±0	02.BHW	['DAPF']	191.71	±0.02	02.BHV	['BP', 'DAPF']
S0325a	B	LF	2019-10-26T06:58:570523Z	±2	229.09	±20	2019-10-26T06:58:55.755261Z	±0.06	02.BHV	['BP', 'CCH']	221.35	±0.27	02.BHV	['CCH', 'BP']
S0407a	B	LF	2020-01-19T09:57:45.773987Z	±5	170.79	±2	2020-01-19T09:57:42.385188Z	±0.27	02.BHW	['DAPF', 'CCH', 'BP']	173.48	±0.34	02.BHE	['CCH', 'BP', 'DAPF']
S0409d	B	LF	2020-01-21T11:31:05.388096Z	±20	180.63	±2	2020-01-21T11:31:14.588741Z	±0.25	02.BHU	['CCH', 'BP']	170.14	±0.06	02.BHV	['CCH', 'BP']
S0484b	B	BB	2020-04-07T08:52:24.077440Z	±20	184.43	±1	2020-04-07T08:52:34.052777Z	±0.52	02.BHW	['BP', 'CCH']	173.04	±0.03	02.BHN	['BP', 'CCH']
S0784a	B	BB	2021-02-09T12:15:56.546674Z	±10	199.77	±5	2021-02-09T12:15:59.317665Z	±0.68	02.BHW	['DAPF', 'BP', 'CCH']	195.47	±0.26	02.BHV	['BP', 'DAPF', 'CCH']
S0802a	B	BB	2021-02-28T06:11:10.703162Z	±5	174.50	±10	2021-02-28T06:11:04.198429Z	±0.34	02.BHZ	['BP', 'CCH', 'DAPF']	180.02	±1.29	02.BHN	['BP', 'CCH']
S0809a	A	LF	2021-03-07T11:13:15.949092Z	±1	173.17	±5	2021-03-07T11:13:15.332942Z	±0.25	02.BHW	['BP', 'CCH']	173.17	±0.36	02.BHE	['BP', 'CCH']
S0820a	A	LF	2021-03-18T14:55:23.391411Z	±5	175.66	±5	2021-03-18T14:55:20.516764Z	±0.31	02.BHZ	['DAPF', 'BP']	174.98	±0.11	02.BHN	['DAPF', 'BP']
S0864a	A	BB	2021-05-02T01:01:17.223068Z	±10	166.83	±5	2021-05-02T01:01:09.174999Z	±0.25	02.BHZ	['BP', 'DAPF', 'CCH']	172.08	±0.16	02.BHE	['BP', 'CCH']
S0899d	B	LF	2021-05-02T01:01:17.223068Z	±10	166.83	±5	2021-06-07T20:10:55.356415Z	±0.24	02.BHW	['BP', 'CCH']	147.56	±0	02.BHU	['DAPF']
S0916d	B	BB	2021-06-25T05:17:32.429620Z	±20	169.57	±2	2021-06-25T05:17:29.561463Z	±0	02.BHW	['CCH']	170.58	±0.37	02.BHV	['BP', 'DAPF', 'CCH']
S0918a	B	LF	2021-06-27T05:35:24.641985Z	±20	158.03	±10	2021-06-27T05:35:20.679714Z	±0.12	02.BHZ	['CCH', 'BP']	157.57	±0.24	02.BHE	['DAPF', 'BP', 'CCH']
S1012d	B	LF	2021-10-02T00:34:13.600173Z	±10	220.50	±2	2021-10-02T00:34:12.303768Z	±0.31	02.BHW	['BP', 'DAPF', 'CCH']	221.56	±0.18	02.BHU	['BP', 'CCH']
S1015f	A	BB	2021-10-04T04:56:00.605894Z	±5	159.61	±2	2021-10-04T04:55:54.950307Z	±0.30	02.BHW	['CCH', 'BP']	165.03	±0.27	02.BHV	['CCH', 'BP']
S1022a	A	LF	2021-10-11T23:18:25.025302Z	±5	178.23	±2	2021-10-11T23:18:24.717651Z	±0.12	02.BHZ	['BP', 'CCH']	177.69	±0.30	02.BHN	['BP', 'CCH']
S1039b	B	BB	2021-10-29T16:16:56.477198Z	±60	172.91	±2	2021-10-29T16:16:52.426243Z	±0.22	02.BHZ	['BP', 'DAPF']	175.61	±0.19	02.BHV	['BP', 'CCF', 'DAPF', 'CCH']
S1048d	A	LF	2021-11-07T22:04:05.355199Z	±1	175.52	±1	2021-11-07T22:04:03.657107Z	±0.04	02.BHW	['DAPF', 'BP', 'CCH']	170.94	±0.59	02.BHE	['BP', 'DAPF', 'CCH']

Table S2. The resulting back azimuths for the events analyzed in this study by 2D and 3D techniques and a comparison with the back azimuths reported in Zenhäusern et al. (2022).

Event name	This study							Zenhäusern et al. (2022)	
	Optimal frequency band (Hz)	Baz 2D (∘)	Uncertainty 2D	SNR 2D	Baz 3D (∘)	Uncertainty 3D	SNR 3D	Baz (∘)	Uncertainty
S0105a	0.6-0.9	153.1	136.9-169.2	10.8	152.7	143.6-161.8	8.1	112	95-133
S0173a	0.2-0.5	87.6	82.0-93.1	105.6	88.7	85.9-91.6	9.6	88	78-103
S0183a	0.3-0.6	81.5	68.5-94.5	17.7	87.9	82.0-93.9	2.9	85	67-101
S0185a	0.4-0.7	321.0	308.3-333.7	18.5	319.0	310.4-327.7	3.4	-	-
S0189a	0.2-0.5	174.6	161.8-187.4	18.4	174.7	165.7-183.7	8.0	-	-
S0235b	0.4-0.8	67.6	58.7-76.4	40.6	72.5	69.5-75.5	1.5	77	64-100
S0290b	0.5-0.8	130.3	107.8-152.8	4.8	110.3	101.9-118.7	4.8	292	257-341
S0325a	0.4-0.7	106.0	82.3-129.6	4.2	108.1	100.4-115.9	14.4	57	43-73
S0407a	0.6-0.9	72.8	40.9-104.6	1.5	58.6	42.0-75.2	1.9	57	43-169
S0409d	0.5-0.8	288.6	273.4-303.7	12.6	289.8	278.7-301.0	4.4	70	50-90*
S0484b	0.3-0.6	253.9	233.1-274.5	6.0	255.7	240.9-270.5	0.3	100	80-120*
S0784a	0.4-0.7	62.4	45.5-79.2	9.8	59.4	49.6-69.3	5.5	115	92-136
S0802a	0.5-0.8	56.9	20.0-93.8	0.7	55.8	45.2-66.4	10.0	82	65-96
S0809a	0.3-0.6	85.6	74.7-96.4	26.1	90.5	86.0-95.0	2.6	91	82-100
S0820a	0.3-0.6	78.9	66.0-91.9	17.8	87.8	82.0-93.6	3.1	106	85-120
S0864a	0.5-1.0	181.6	157.6-205.6	4.0	199.7	185.6-213.8	0.7	90	66-110
S0899d	0.4-0.7	43.7	24.3-63.0	7.1	41.2	31.7-50.6	2.5	22	354-55
S0916d	0.5-0.8	29.0	7.8-50.2	5.6	45.1	37.4-52.7	2.8	97	41-114
S0918a	0.4-0.8	148.4	122.9-174.0	3.4	150.4	132.6-168.2	1.9	137	125-149
S1012d	0.2-0.5	74.7	60.4-89.0	14.3	77.0	67.7-86.2	2.4	-	-
S1015f	0.2-0.5	93.5	78.3-108.8	12.4	99.6	95.2-104.1	13.4	-	-
S1022a	0.3-0.6	85.7	66.1-105.3	6.8	89.3	82.1-96.6	15.5	-	-
S1039b	0.2-1.0	187.4	168.9-206.0	7.9	182.7	172.3-193.1	3.8	-	-
S1048d	0.3-1.0	191.7	163.5-219.9	2.5	180.8	164.5-197.0	1.5	-	-

Table S3. The ground truth locations of the two meteoroid impacts, according to Posiolova et al. (2022).

Event	Lat (deg)	Lon (deg)	Distance (deg)	Distance (km)	Azimuth (deg)	Baz (deg)
S1000a	38.1080	-79.8771	126.1188	7481.018	314.5057	34.3429
S1094b	34.8037	-170.0800	58.3821	3463.0660	251.9719	51.6921

Table S4. The seismologically estimated distance from the ground truth locations of the two meteoroid impacts. (MQS: Marsquake Service, https://doi.org/10.12686/a18)

Distance from ground truth location	S1000a		S1094b	
	Δ (º)	Δ (km)	Δ (º)	Δ (km)
MQS	17.9203	1062.9842	6.4592	383.1405
Posiolova et al. (2022)	16.3608	970.4749	15.7602	934.8513
This study	9.0361	535.9940	8.2916	491.8376